

**COMPARISONS OF FINITE-ELEMENT CODE CALCULATIONS  
TO HYDROSTATICALLY LOADED  
SUBASSEMBLY-DUCT EXPERIMENTS**

**by**

**J. E. Ash and T. J. Marciniak**

BASE TECHNOLOGY



U of C-AUA-USERDA

---

**ARGONNE NATIONAL LABORATORY, ARGONNE, ILLINOIS**

**Prepared for the U. S. ENERGY RESEARCH  
AND DEVELOPMENT ADMINISTRATION**

The facilities of Argonne National Laboratory are owned by the United States Government. Under the terms of a contract (W-31-109-Eng-38) between the U. S. Energy Research and Development Administration, Argonne Universities Association and The University of Chicago, the University employs the staff and operates the Laboratory in accordance with policies and programs formulated, approved and reviewed by the Association.

#### MEMBERS OF ARGONNE UNIVERSITIES ASSOCIATION

The University of Arizona	Kansas State University	The Ohio State University
Carnegie-Mellon University	The University of Kansas	Ohio University
Case Western Reserve University	Loyola University	The Pennsylvania State University
The University of Chicago	Marquette University	Purdue University
University of Cincinnati	Michigan State University	Saint Louis University
Illinois Institute of Technology	The University of Michigan	Southern Illinois University
University of Illinois	University of Minnesota	The University of Texas at Austin
Indiana University	University of Missouri	Washington University
Iowa State University	Northwestern University	Wayne State University
The University of Iowa	University of Notre Dame	The University of Wisconsin

#### NOTICE

This report was prepared as an account of work sponsored by the United States Government. Neither the United States nor the United States Energy Research and Development Administration, nor any of their employees, nor any of their contractors, subcontractors, or their employees, makes any warranty, express or implied, or assumes any legal liability or responsibility for the accuracy, completeness or usefulness of any information, apparatus, product or process disclosed, or represents that its use would not infringe privately-owned rights. Mention of commercial products, their manufacturers, or their suppliers in this publication does not imply or connote approval or disapproval of the product by Argonne National Laboratory or the U. S. Energy Research and Development Administration.

Printed in the United States of America  
Available from  
National Technical Information Service  
U. S. Department of Commerce  
5285 Port Royal Road  
Springfield, Virginia 22161  
Price: Printed Copy \$5.00; Microfiche \$3.00

---

ANL-77-1

---

ARGONNE NATIONAL LABORATORY  
9700 South Cass Avenue  
Argonne, Illinois 60439

COMPARISONS OF FINITE-ELEMENT CODE CALCULATIONS  
TO HYDROSTATICALLY LOADED  
SUBASSEMBLY-DUCT EXPERIMENTS

by

J. E. Ash and T. J. Marciniak

Reactor Analysis and Safety Division

January 1977



## TABLE OF CONTENTS

	<u>Page</u>
ABSTRACT . . . . .	11
I. INTRODUCTION. . . . .	11
II. HYDROSTATIC PRESSURIZATION EXPERIMENTS . . . . .	14
A. Test Apparatus . . . . .	15
B. Test-plan Matrix. . . . .	16
C. General Results . . . . .	17
III. THE COMPUTER CODE . . . . .	26
IV. MECHANICAL PROPERTIES OF THE STEEL. . . . .	31
A. Annealed Type 316 Stainless Steel . . . . .	36
B. The 20%-coldworked Steel with Hardness Gradients. . . . .	42
C. The 50%-coldworked Type 316 Stainless Steel. . . . .	44
V. COMPARISONS OF CALCULATIONS WITH EXPERIMENTS . . . . .	47
A. Hydrostatic Tests with Annealed Hexcan . . . . .	48
1. Internal-pressurization Tests . . . . .	48
2. External-pressurization Tests . . . . .	51
B. The Nominal 20%-coldworked Hydrostatic Tests . . . . .	54
C. The 50%-coldworked Hydrostatic Tests . . . . .	56
1. Internal-pressurization Tests . . . . .	56
2. External-pressurization Tests . . . . .	59
VI. SUMMARY AND CONCLUSIONS . . . . .	60
APPENDIXES	
A. The STRAW and SADCAT Codes. . . . .	63
1. The STRAW Code . . . . .	63
2. The SADCAT Code . . . . .	65
B. The Plane-strain Assumption . . . . .	69
1. The Elastic Range and Initial Yield Point . . . . .	69
2. Plastic Flow and Subsequent Yields . . . . .	72

## TABLE OF CONTENTS

	<u>Page</u>
C. Analytical Representation of Stress-Strain Relationship . . . . .	78
ACKNOWLEDGMENTS . . . . .	84
REFERENCES . . . . .	85

## LIST OF FIGURES

<u>No.</u>	<u>Title</u>	<u>Page</u>
1.	Test Apparatus Used in Internal Hydrostatic Pressurization of Subassembly Ducts. . . . .	15
2.	Test Apparatus Used in External Hydrostatic Pressurization of Subassembly Ducts. . . . .	15
3.	Typical Locations of Instruments for Deflection and Strain Measurements. . . . .	18
4.	Measured Midflat and Corner Displacements for Annealed Type 316 Stainless Steel Test Hexcan . . . . .	18
5.	Measured Strains at Midflat Inner and Outer Surfaces of Annealed Hexcan . . . . .	19
6.	Effect of Test Length upon Midflat Deflection of Annealed Hexcan. . . . .	19
7.	Effect of Test Length upon Corner Deflection of Annealed Hexcan. . . . .	19
8.	Effect of Test Length upon Deflection Profiles in Axial Direction of Annealed Hexcan . . . . .	20
9.	Comparison of Experimental Midflat Deflections of Annealed and Nominal 20%-coldworked Hexcans under Internal Pressurization at Room Temperature. . . . .	21
10.	Comparison of Experimental Corner Deflections of Annealed and Nominal 20%-coldworked Hexcans under Internal Pressurization at Room Temperature. . . . .	21
11.	Comparison of Experimental Midflat Outer-surface Strains of Annealed and Nominal 20%-coldworked Hexcans under Internal Pressurization at Room Temperature . . . . .	21
12.	Measured Midflat Displacement of 50%-coldworked Hexcan under Internal Pressurization at Room Temperature . . . . .	22
13.	Measured Corner Displacement of 50%-coldworked Hexcan under Internal Pressurization at Room Temperature . . . . .	22
14.	Measured Strain at Inner Midflat Surface of 50%-coldworked Hexcan under Internal Pressurization at Room Temperature . . . . .	22
15.	Measured Strain at Outer Midflat Surface of 50%-coldworked Hexcan under Internal Pressurization at Room Temperature . . . . .	23
16.	Annealed and Nominal 20%-coldworked Test Hexcans Internally Pressurized to Failure . . . . .	23

## LIST OF FIGURES

<u>No.</u>	<u>Title</u>	<u>Page</u>
17.	The 50%-coldworked Hexcan Internally Pressurized to Failure . .	23
18.	Detail of Upper Crack Tip for 50%-coldworked Hexcan Internally Pressurized to Failure . . . . .	24
19.	Detail of Lower Crack Tip for 50%-coldworked Hexcan Internally Pressurized to Failure . . . . .	24
20.	Examples of Strain Reversals at Corner Outer Surface and Midflat Inner Surface for Internal Pressurization of Annealed Hexcan at Room Temperature. . . . .	30
21.	Comparison of Measured Midflat Displacements with STRAW and SADCAT Computations for Internally Pressurized Annealed Hexcan at Room Temperature . . . . .	31
22.	Empirical Correlation of Coldworking and Hardness for Type 316 Stainless Steel. . . . .	32
23.	Survey of Diamond Point Hardness of Sample over Wall Thickness for a Nominal 20%-coldworked Hexagonal Duct in Condition Received from Vendor . . . . .	32
24.	Average Hardness Profile from Midflat to Corner for Sample, Nominal 20%-coldworked, Hexagonal Duct Section . . . . .	33
25.	Graphs of True Stress vs Engineering Strain for Annealed and 20%- and 50%-coldworked Type 316 Stainless Steel Test Hexcans .	33
26.	General Characteristics of Stress-Strain Graph . . . . .	34
27.	Sensitivity of Midflat Deflections to Variations in Material Properties for an Annealed Type 316 Stainless Steel Internally Pressurized Hexcan . . . . .	35
28.	Annealed Type 316 Stainless Steel Tensile Specimens before and after Testing. . . . .	36
29.	Estimated Influence of Crosshead Speed upon Magnitude of Uniaxial Yield Stress for Annealed Hexcan Tensile-test Specimens . .	38
30.	Tensile-test Data for Unit Load vs Elongation for an Annealed Hexcan Tensile Specimen (7-AN-B), Crosshead Speed Being 0.2 in./min. . . . .	39
31.	Diamond-point-hardness Survey over Wall Thickness for Annealed Test Hexcan . . . . .	40
32.	Effect of Coldworking on Mechanical Properties of Type 316 Stainless Steel. . . . .	40



## LIST OF FIGURES

<u>No.</u>	<u>Title</u>	<u>Page</u>
33.	Hardness Profile Measured along Axial Direction of Nominal 20%-coldworked Duct . . . . .	43
34.	Hardness Profile Measured from Midflat to Corner for Section from Harder Portion of 20%-coldworked Duct . . . . .	43
35.	Diamond-point-hardness Survey over Wall Thickness for 50%-coldworked Test Hexcan . . . . .	46
36.	Tensile-test Data of Elongation vs Unit Load for 50%-coldworked Hexcan Tensile Specimen (1-50-D) with Crosshead Speed of 0.02 in./min . . . . .	46
37.	Room-temperature Tensile-test Stress-Strain Data for Annealed Type 316 Stainless Steel Corrected for Plane-strain Conditions . .	48
38.	Influence of Assumed Hardening Model upon New Yield Point. . . .	49
39.	Comparison of Experimental and Calculated Midflat Displacements for Annealed Type 316 Stainless Steel Internally Pressurized Hexcan . . . . .	50
40.	Comparison of Experimental and Calculated Corner Displacements for Annealed Type 316 Stainless Steel Internally Pressurized Hexcan . . . . .	50
41.	Comparison of Experimental and Calculated Outer Midflat Strains for Annealed Type 316 Stainless Steel Internally Pressurized Hexcan. . . . .	50
42.	Unstable Collapse Modes for Externally Loaded Hexcan . . . . .	52
43.	Sample STRAW-code Calculation of Unstable Collapse Mode for Externally Loaded Hexcan . . . . .	52
44.	Final Shape of Externally Pressurized Annealed Hexcan . . . . .	52
45.	Comparison of Experimental and Calculated Midflat Displacements for Annealed Type 316 Stainless Steel Externally Pressurized Hexcan . . . . .	53
46.	Comparison of Experimental and Calculated Corner Displacements for Annealed Type 316 Stainless Steel Externally Pressurized Hexcan . . . . .	53
47.	Comparison of Experimental and Calculated Outer Midflat Strains for Annealed Type 316 Stainless Steel Externally Pressurized Hexcan. . . . .	53
48.	Simplified Pantograph Model to Estimate Midflat Deflection Component due to Plastic-hinge Rotation at Corner . . . . .	54

## LIST OF FIGURES

<u>No.</u>	<u>Title</u>	<u>Page</u>
49.	Comparison of Experimental and Calculated Midflat Displacements for Nominal 20%-coldworked Type 316 Stainless Steel Internally Pressurized Hexcan . . . . .	55
50.	Comparison of Measured Strains at Midflat of Outer Surface with Computed Strains . . . . .	56
51.	Room-temperature Tensile-test Stress-Strain Data for 50%-coldworked Type 316 Stainless Steel Corrected for Plane-strain Conditions . . . . .	57
52.	Comparison of Experimental and Computed Midflat Deflections for 50%-coldworked Type 316 Stainless Steel Internally Pressurized Hexcan . . . . .	57
53.	Comparison of Experimental and Computed Corner Deflections for 50%-coldworked Type 316 Stainless Steel Internally Pressurized Hexcan . . . . .	58
54.	Comparison of Experimental and Computed Outer-surface Midflat Strains for 50%-coldworked Type 316 Stainless Steel Internally Pressurized Hexcan. . . . .	58
55.	Comparison of Experimental and Computed Inner-surface Midflat Strains for 50%-coldworked Type 316 Stainless Steel Internally Pressurized Hexcan. . . . .	58
56.	Comparison of Experimental and Computed Midflat Deflections for 50%-coldworked Type 316 Stainless Steel Externally Pressurized Hexcan. . . . .	59
57.	Comparison of Experimental and Computed Corner Deflections for 50%-coldworked Type 316 Stainless Steel Externally Pressurized Hexcan. . . . .	59
58.	Comparison of Experimental and Computed Inner-surface Midflat Strains for 50%-coldworked Type 316 Stainless Steel Externally Pressurized Hexcan. . . . .	59
59.	Comparison of Experimental and Computed Outer-surface Midflat Strains for 50%-coldworked Type 316 Stainless Steel Externally Pressurized Hexcan. . . . .	59
A.1.	SADCAT Computation of Influence of End Constraints upon Longitudinal Deflection Profile and Comparison with Measured Deflections for Annealed Type 316 Stainless Steel Internally Pressurized Hexcan . . . . .	65

## LIST OF FIGURES

<u>No.</u>	<u>Title</u>	<u>Page</u>
A.2.	SADCAT Computation of Influence of End Constraints upon Maximum Midflat Deflection for Annealed Type 316 Stainless Steel Internally Pressurized Hexcan . . . . .	66
B.1.	Top View of Hexcan Showing Beam Elements That Deflect Radially Outward for an Internal Pressurization. . . . .	69
B.2.	Representative Hexcan Sector for Plane-strain Conditions . . . . .	69
B.3.	Increase in Plane-strain Yield Stress over Uniaxial Tensile-test Yield Stress. . . . .	72
B.4.	Uniaxial Tensile-test Stress-Strain Curve with Definitions of Incremental Elastic- and Plastic-strain Components. . . . .	73
C.1.	Empirical Fitting of Stress-Strain Relationship for Annealed Type 316 Stainless Steel. . . . .	81

## LIST OF TABLES

<u>No.</u>	<u>Title</u>	<u>Page</u>
I.	Test-plan Matrix for Hydrostatic Pressurization of Subassem- bly Duct. . . . .	16
II.	Fracture Characteristics of Internally Pressurized Type 316 Stainless Steel . . . . .	24
III.	Effect of Coldworking upon Properties of Type 316 Stainless Steel. . . . .	35
IV.	Tensile-test Results for Annealed Type 316 Stainless Steel. . . . .	38
V.	Posttest Microhardness Measurements of Duct. . . . .	42
VI.	Tensile-test Results for Nominal 20%-coldworked Duct Material at 70°F (21°C). . . . .	44
VII.	Tensile-test Results for 50%-coldworked Duct Material at 70°F (21°C) . . . . .	45

# COMPARISONS OF FINITE-ELEMENT CODE CALCULATIONS TO HYDROSTATICALLY LOADED SUBASSEMBLY-DUCT EXPERIMENTS

by

J. E. Ash and T. J. Marciniak

## ABSTRACT

The Liquid Metal Fast Breeder Reactor (LMFBR) core structure consists of a matrix of hexagonal subassembly ducts. Evaluation of the safety aspects of the core structure requires that reliable computational procedures be available to predict the deformation response of the subassembly configuration to postulated local energy releases. Finite-element computer codes have been developed to calculate deflections and strains of a hexcan subassembly wrapper subjected to internal and external dynamic pressure loadings over a wide range of material-property conditions. An experimental and analytical program has been undertaken to validate and extend the codes for describing the core structural mechanics under reactor operating conditions, including, in particular, descriptions of possible subassembly-to-subassembly damage propagation.

This report describes results of the first phase of the experimental program in which single hexcan sections were internally and externally hydrostatically pressurized out-of-pile at room temperature. The experimental data are compared with calculations from a two-dimensional finite-element structural-dynamics code, STRAW. Some additional comparisons were also made with calculations from a three-dimensional code, SADCAT. The correlations obtained between the computations and the hydrostatic experimental results were sufficiently good to validate the STRAW code and proceed to the next phase of the program involving the dynamic structural response.

## I. INTRODUCTION

Questions relating to the safety of the Liquid Metal Fast Breeder Reactor (LMFBR) involve the response of subassembly ducts and internals such as fuel pins and wire-wrap spacers, to postulated local accident conditions. At issue, essentially, is the ability of subassemblies to resist propagation of failure from subassembly to subassembly under either normal reactor operating conditions or accident conditions that involve portions of the core.

A number of mechanisms have been hypothesized by which damage may be propagated. Thermal loads imposed by molten fuel may cause thermal-stress cracks and subsequent rupture, or local melting of the duct walls. Wall failures also could be caused by severe pressure pulses arising from various sources, such as a sudden large release of fission gas or a fuel-vapor expansion resulting from a severe overpower transient.

Thermal interactions between the coolant and high-temperature molten fuel or cladding provide another mechanism through which damaging pressure pulses may be created. An actual core-failure propagation will most likely involve combinations of these high-temperature and potentially high-pressure phenomena. The dominant mode in a given subassembly event will depend both upon the initiating conditions and the accident sequence.

Since the structure in the core region is quite complex, determination of the response of the core to locally generated pressure pulses is difficult to assess, from both the analytical and experimental points of view. Factors which must be considered in the study of such events include (a) definition of local subassembly accidents which may produce significant pressure pulses; (b) definition of subassembly material properties at various times in the core life under operating or accident conditions; (c) propagation phenomena, including subassembly fracture modes and locations; and (d) geometry of the subassembly structure, including the intersubassembly coolant, the surrounding subassemblies and their internals, and of other auxiliary structures that may be involved, such as control-rod guide tubes.

The definition of local subassembly accidents poses one of the most difficult areas to resolve since a wide range of initiating conditions may be postulated followed by various mechanistic sequences. One of the more likely initiating events to occur during the life of a reactor is the failure of the cladding of one or more end-of-life fuel pins, resulting in the release of high-pressure fission gas. Events such as subassembly blockages, which could produce meltdown and thermal interactions between the coolant and hot fuel or cladding, and overpower transients, causing fuel vaporization, can be reduced to a very low probability through proper reactor design and controls. Current intensive studies of local accident-sequence phenomena should lead to the development of definitive models of more realistic pressure-time relationships.

Uncertainties also exist in the definition of the mechanical properties of the stainless steel subassembly-duct material, especially nearing the high-fluence, end-of-life conditions. Properties such as yield, ultimate strengths, and ductility, which are crucial for structural-response analysis are subject to significant variations due to local temperatures and to irradiation exposure. Under dynamic loading conditions, strain-rate effects and fracture mechanisms present additional complexities entering into the description of material behavior. The effort underway to resolve these material-property problems can be expected to lead to improved material descriptions and mathematical models, and contribute to the development of adequate margins of structural safety.

Because of the existing uncertainties in the realistic description of source-pressure pulses and the accurate prediction of subassembly-duct-material properties, a definitive experimental program to determine prototypic hexcan response to local accidents was not attempted. The objective of the current experimental program is to devise an appropriate set of tests to provide sufficient data to verify and, where required, to modify and extend the finite-element computer codes under development. Then, by providing improved descriptions of source-pressure pulses and thermal loadings as input data, and incorporating updated material-property information, we can use the computer codes for the analysis of the many possible reactor accident events.

The dynamic structural codes under development include the STRAW<sup>1</sup> and SADCAT<sup>2</sup> codes which are, respectively, two- and three-dimensional, non-linear, elastic-plastic finite-element codes. The STRAW code takes into account not only the accident subassembly, but also the next one or two rows of subassemblies together with the inclusion of the coolant-fluid behavior, and various energy and pressure sources.<sup>3</sup> The SADCAT code has been coupled to the REXCO code and provides similar pressure-source capabilities, although the surrounding ducts are not, as yet, included in the analysis.<sup>4</sup> The original versions of the codes use explicit time-integration techniques; an implicit computational procedure for STRAW has recently been completed,<sup>5</sup> and a similar implicit version of SADCAT is being developed.

Since the experimental program was designed to verify the calculational models that describe the subassembly response, and not to perform strictly prototypic tests, the test program was organized in the following way. First, quasi-static experiments were performed to define the gross response of subassembly ducts to internal and external pressure loads. Measurements of pressure, strains, and midflat deflections for specified material properties were compared with code calculations. These comparisons establish the basic soundness of the codes, and contribute to the development of refinements and to the elimination of initial uncertainties in the analytical model. Second, after the development of a calibrated reproducible and verified pressure-time source, dynamic tests in single subassemblies are to be performed. Finally, subassembly-cluster tests will be scheduled, including the effects of intersubassembly fluids to evaluate subassembly-to-subassembly propagation-coupling phenomena.

This report describes some results obtained in the first phase of the effort: the quasi-static pressurization tests. These results include several internal and external hexcan-pressurization experiments, material-property determinations, and comparisons with calculational results to demonstrate the range of validity of the small-strain, large-deflection, computer codes. Under actual reactor operating conditions the embrittling effects of irradiation exposure can cause the hexcan steel to be considerably less ductile than the nominally 20%-coldworked condition of the sample ducts received from the fabricator for the pressurization tests. The Materials Science Division at ANL

has investigated<sup>6</sup> the simulation of material properties under reactor operating conditions and developed methods for altering the hexcan steel so that the pressurization tests covered a range of ductility conditions. In addition to the 20%-coldworked test hexcans, more ductile specimens were produced by annealing, and the ductility was lowered by a special fabrication process to produce a final 50% coldworking of the subassembly duct sections.

## II. HYDROSTATIC PRESSURIZATION EXPERIMENTS

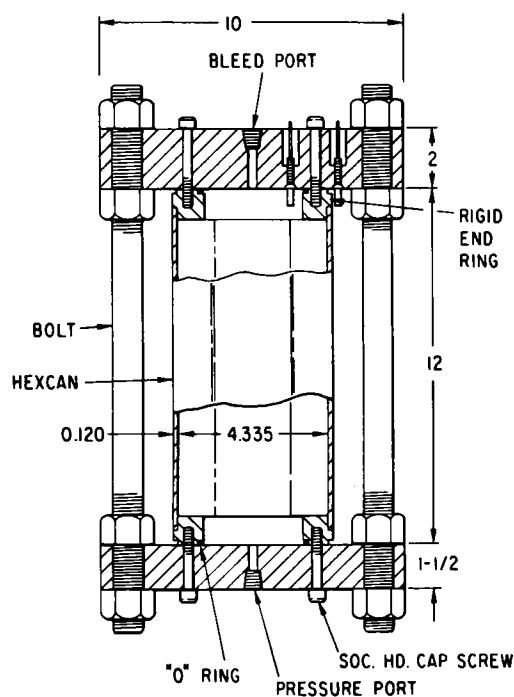
The main goals of the experimental program investigating subassembly-to-subassembly failure propagation are to verify, modify, and extend the finite-element code STRAW. A first step in this program was the design of a set of experiments to establish the capability of the code to calculate deformations of a hydrostatically loaded subassembly hexcan. These experiments were intended to supply initial verifications without the attendant uncertainties involved in the dynamics of a suddenly applied pressure pulse and to avoid possibly strong undefined strain-rate effects on the material properties. Results of the hydrostatic tests will also contribute to the prediction of response magnitudes upon which to base the design and the instrumentation requirements of the subsequent dynamic experiments.

To provide acceptable test results for comparison with STRAW calculations, several experimental requirements had to be met. Since the STRAW code requires that the hexcan deformation be formulated as a plane-strain problem, the test rig must be designed to constrain axial displacements. Because of the demonstrated response sensitivity to material properties, the stress-strain characteristics and possible hardness gradients in the duct walls must be accurately determined. Instrumentation should include the measurement of mid-flat and corner deflections, as well as midflat inner- and outer-surface strains in both the circumferential and axial direction. Sufficient redundancy is needed to ensure that the hexcan response is symmetric, to reveal possible inconsistencies in the data, and to reduce the probability of data loss through partial instrumentation failures. Because hexcan material is relatively difficult to obtain and available duct sections were of limited lengths, it was necessary to use the shortest length possibly and still achieve plane-strain conditions without significant end effects coming into play. In a previous study<sup>7</sup> it was demonstrated that a fixed end condition, constraining axial, radial, and rotational motions, would provide good results for STRAW calculations for a duct length of 1 ft (30.48 cm). Although these calculations were performed using a circular cylinder representing an "equivalent" hexcan, they did show that a length-to-diameter ratio of about three would be sufficient for the range of deflections expected in the tests. Experimental verification of this calculation was obtained by comparing 1- and 2-ft (30.48- and 60.96-cm)-length internal-pressurization tests over a wide range of pressures. These tests are described below. A more detailed presentation of the test apparatus and results than presented here has been given in Ref. 8.



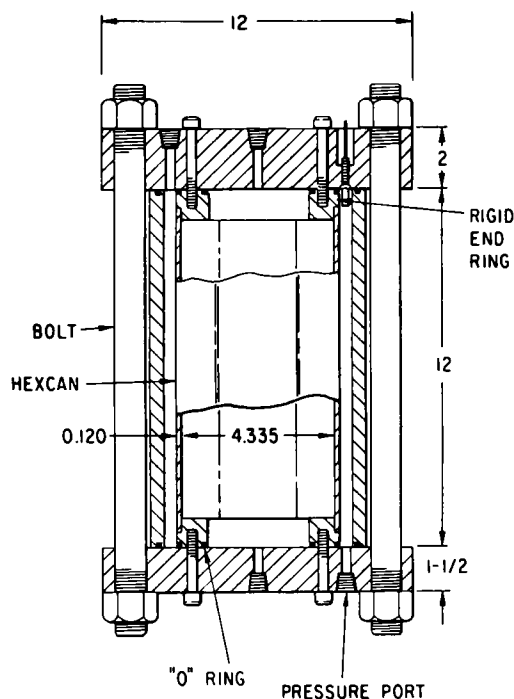
## A. Test Apparatus

To meet the experimental requirements outlined above, the test apparatus shown in schematic form in Figs. 1 and 2 was designed and constructed by Stanford Research Institute (SRI) specifically for the external-pressurization tests, which were conducted at SRI. The hexcan was first mounted in rigid end rings, and a dowel was then inserted through the ring and hexcan. This configuration was welded together to ensure rigidity and to seal the hexcan-ring junction. The assembly was next mounted in heavy end plates; the top plate was 2 in. (5.08 cm) thick and the lower 1.5 in. (3.81 cm) thick. An O-ring was used between the end ring and the plate for sealing, and the end plates were clamped in position with six 0.375-in. (0.9525 cm) socket-head capscrews. Axial movement was constrained by bolting the endplates together with a set of twelve 1-in. (2.54-cm) bolts.



ALL DIMENSIONS IN inches

Fig. 1. Test Apparatus Used in Internal Hydrostatic Pressurization of Subassembly Ducts (1 in. = 2.54 cm).  
ANL Neg. No. 900-4648.



ALL DIMENSIONS IN inches

Fig. 2. Test Apparatus Used in External Hydrostatic Pressurization of Subassembly Ducts (1 in. = 2.54 cm).  
ANL Neg. No. 900-75-218.

Although not shown in the figure, nuts were mounted both above and below the end plates. These bolts were mounted on a bolt-circle diameter of 8.3125 in. (21.114 cm). The cross-sectional area of the 12 bolts is approximately five times that of the cross-sectional area of the hexcan material. Calculations indicate that with this arrangement the axial movement of the ends would not exceed 2 mils (0.0508 mm) under an internal hexcan pressurization of 3000 psi (21 MPa). This calculation was verified and the plane-strain assumption justified in an early shakedown test in which axially oriented strain gages near the duct midplane showed small strains over the range of interest.

Pressurization of the subassembly ducts was accomplished by using a hydraulic hand pump. The pump was connected by a flexible line to the pressure-port taps shown in Figs. 1 and 2, and the pressure was measured by a gage installed in this line. For internal pressurization, the inside pressure port was used; for external pressurization, the outside port was used with the hexcan enclosed within the thick-walled cylinder, as shown in Fig. 2. This cylinder was not mounted during the internal pressurization tests, so that access to appropriate instrumentation for displacement measurement was available.

Instrumentation used in the tests consisted of the pressure gage already mentioned, strain gages, and devices to measure linear displacement. In the initial experiments, dial gages were used to measure displacements of the midflats and corners. In the later experiments, the dial gages were replaced with linear potentiometers, which are more compact and less subject to binding, and can be read remotely. The number of linear potentiometers was increased to include up to three flats and three corners in order to show that the displacements of the flats were symmetric, as well as to give an improved average of the midflat and corner displacements. Strain gages were mounted on both the outside and inside surfaces of several flats to measure circumferential strains. In some tests, notably the test using a 24-in. (61-cm) duct, gages were also mounted at several axial positions, including regions near the end ring, in order to collect data on local bending and end effects.

## B. Test-plan Matrix

The experimental program for the static pressurization of the subassembly hexcan consisted of eight tests. The tests and general parameters are given in Table I.

TABLE I. Test-plan Matrix for Hydrostatic Pressurization of Subassembly Duct

Test No.	Material Condition	Hexcan Nominal Length, in. (cm)	Type Loading	Remarks
ST-101I	20% coldworked	12 (30.5)	Internal	Shakedown test, limited instrumentation. Failed at 2400 psi (16.55 MPa).
ST-102E	20% coldworked	12 (30.5)	External	Shakedown test, limited instrumentation.
ST-103I	Annealed	12 (30.5)	Internal	Taken to failure at 4500 psi (31.03 MPa).
ST-104I	Annealed	24 (61)	Internal	Investigate end effects.
ST-105E	Annealed	12 (30.5)	External	Collapsed at 600 psi (4.14 MPa).
ST-106I	50% coldworked	12 (30.5)	Internal	Taken to failure at 3100 psi (21.37 MPa).
ST-107I	Annealed	12 (30.5)	Internal	Repeat of ST-103I with more extensive instrumentation.
ST-108E	50% coldworked	12 (30.5)	External	Collapsed at 1450 psi (10.00 MPa).

The first two tests were performed mainly as shakedown tests to eliminate, as much as possible, defects in the experimental apparatus and procedure. The instrumentation included in these tests was not quite as extensive as in the later tests. Also, for the first two tests the material properties had not been established, although some preliminary hardness tests indicated that substantial coldwork gradients from midflat to corner existed in the duct wall. Stress-strain curves were not specifically determined for the 20%-coldworked level.

The next two tests, ST-103I and -104I, were performed with solution-annealed, Type 316 stainless steel ducts. These tests were designed not only to provide data on midflat and corner deflections and strains as functions of internal pressure, but also to investigate the extent of end effects. Thus, Test ST-104I used a 2-ft (60.96-cm)-long hexcan with strain gages and linear potentiometers arranged axially along the midflat at six positions on the upper half of the duct. The results of these tests, to be described in detail below, are shown in Fig. 8 (later).

Tests ST-105E and -108E were performed to study the behavior of ducts under external loading conditions. For Test ST-105E, the Type 316 stainless steel test hexcan was annealed; and for Test ST-108E, the test hexcan was 50% coldworked to produce a considerably less ductile steel. Some interesting results pertaining to the collapse of subassembly ducts are discussed in Chap. V. In Test ST-106I, a 50%-coldworked duct was internally pressurized to determine if the calculational models were able to predict deflections of more brittle materials.

In summary, the test matrix to date has been constructed to gain data on the deformation of subassembly ducts under internal and external pressure loadings at room temperature. Also, the effects of ductility are included by testing ducts with varying degrees of coldworking ranging from fully annealed to nominally 50% coldworking. The influence of end effects on the measurement was determined by performing a well-instrumented test on a hexcan twice the length of those normally used in the tests.

### C. General Results

The objective of this section is to indicate in general terms the results of the experiments. The detailed discussion of experimental results is deferred to Chap. V, in which the experimental results and code calculations are compared. Here we would like to emphasize those experimental data that (1) show that the plane-strain conditions were satisfied, (2) show that end effects were minimal, and (3) illustrate some fracture phenomena on those ducts that were pressurized to failure. Also discussed are general test results of midflat deflections, corner displacements, and strains from representative tests of annealed and 20%- and 50%-coldworked hexcans.

The results of Test ST-103I, which was instrumented with redundant strain gages, helped to demonstrate that the hexcan deformation remained very nearly symmetric throughout the internal pressurization and that the center section was in essentially a plane-strain condition.\* Note that this symmetry persists only for the internally pressurized hexcans; external pressurization led to an asymmetrical collapse mode, as would be expected since the system is in an essentially metastable condition.

The dial- and strain-gage locations are shown in Fig. 3. The dial gages measured the deflections of flats A and D, and corner displacements at A/B and D/E. Strain gages were placed to measure inside and outside circumferential strain, and three strain gages were used to measure axial strain. The symmetry of the hexcan deformation is shown by the comparison of the midflat deflections of flats A and D shown in Fig. 4. There is little difference in deflection up to about 200 psi (1.4 MPa), when a slight difference of about 10 mils (0.254 mm) may be noted. The deflections at corners A/B and D/E were also compared and showed little disagreement. A characteristic of the pressurization tests with ductile hexcan materials is that the corner first moves in about 25 mils (0.6 mm) and then expands outward as the hexcan assumes a right-circular cylindrical shape.

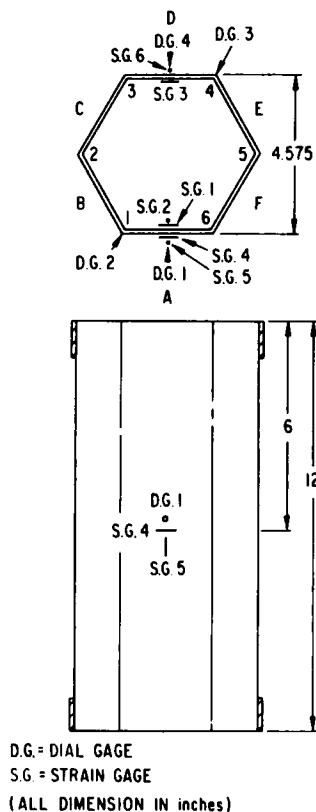


Fig. 3

Typical Locations of  
Instruments for Deflec-  
tion and Strain Measure-  
ments (Test ST-103I)  
(1 in. = 2.54 cm)

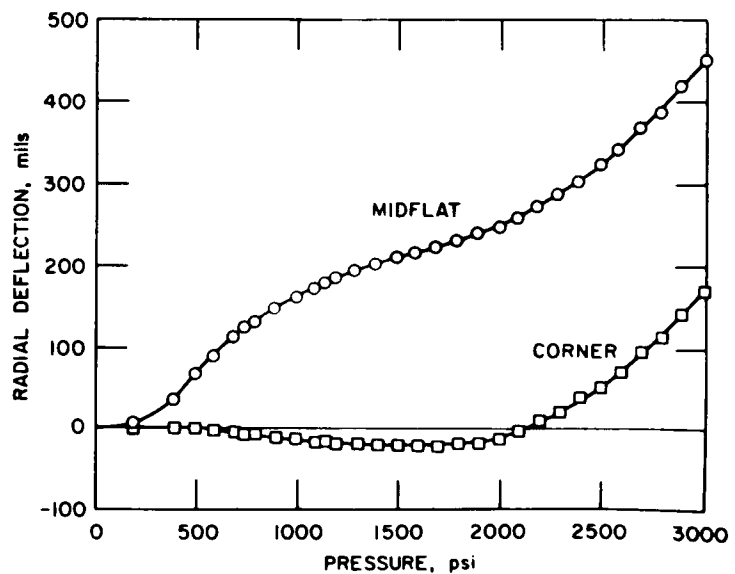


Fig. 4

Measured Midflat and Corner Displacements for  
Annealed Type 316 Stainless Steel Test Hexcan  
(Test ST-103I) (1 mil = 0.0254 mm;  
1 psi = 6.895 kPa)

\*Test ST-107I was also redundantly instrumented and was used as the basis for the comparison in Chap. V. The results of Tests ST-107I and -103I are in agreement.

Of major importance in these tests is the necessity for maintaining plane-strain conditions in the midplane section between the ends of the hexcan.

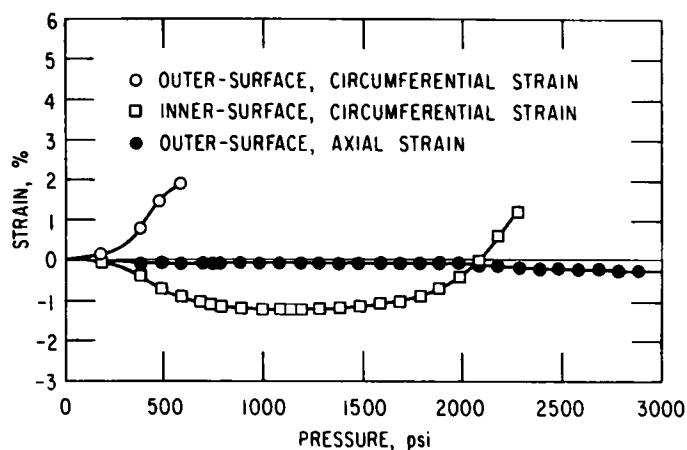


Fig. 5. Measured Strains at Midflat Inner and Outer Surfaces of Annealed Hexcan (Test ST-103I)  
(1 psi = 6.895 kPa)

but as the internal pressurization increased the hexcan shape approached that of a circular cylinder and a strain reversal occurred; the inner surface was in tension at about 2000 psi (14 MPa).

That a test hexcan length of 12 in. (30.48 cm) is sufficient to essentially eliminate end effects is demonstrated in the comparisons shown in Figs. 6-8 between 12- and 24-in. (30.48- and 60.96-cm)-long test sections. Test ST-103I was for a 12-in. (30.48-cm)-long and ST-104I for a 24-in. (60.96-cm)-long hexcan; both hexcans were of annealed Type 316 stainless steel. The comparison

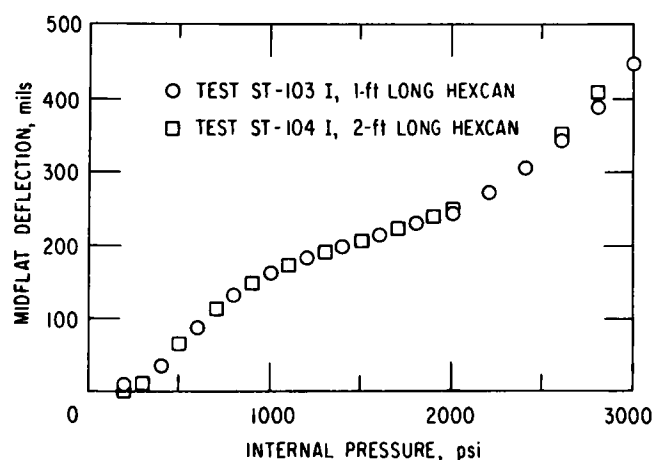


Fig. 6. Effect of Test Length upon Midflat Deflection of Annealed Hexcan  
(1 ft = 30.48 cm; 1 psi = 6.895 kPa;  
1 mil = 0.0254 mm)

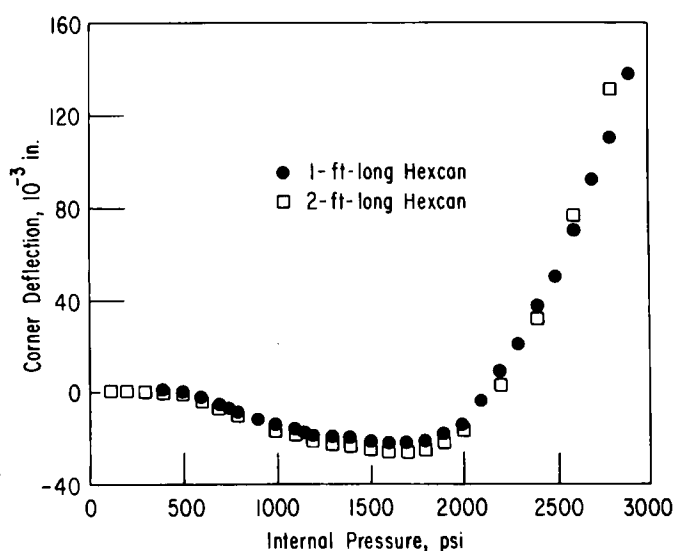


Fig. 7. Effect of Test Length upon Corner Deflection of Annealed Hexcan (1 in. = 2.54 cm;  
1 ft = 30.48 cm; 1 psi = 6.895 kPa). ANL  
Neg. No. 900-75-221.

in Fig. 6 of the midflat, midplane deflections of a duct wall shows that the deflections were essentially identical through a pressurization up to 3000 psi (21 MPa), which is essentially at the upper range of interest. Similarly in Fig. 7, the corner displacements also compare almost exactly over the same range of pressure loadings. As a further demonstration of the minimal effect on test results due to end effects, longitudinal deflection profiles for various pressure levels are shown in Fig. 8. These results show that end effects involving strong local bending were confined to a neighborhood of about one hexcan diameter from the rigid end-ring weldments. Thus, in the 12-in. (30.48-cm)-long specimens, we could expect a section of at least 2 in. (5.08 cm) midway between the ends where end effects would be negligible and plane-strain conditions would prevail.

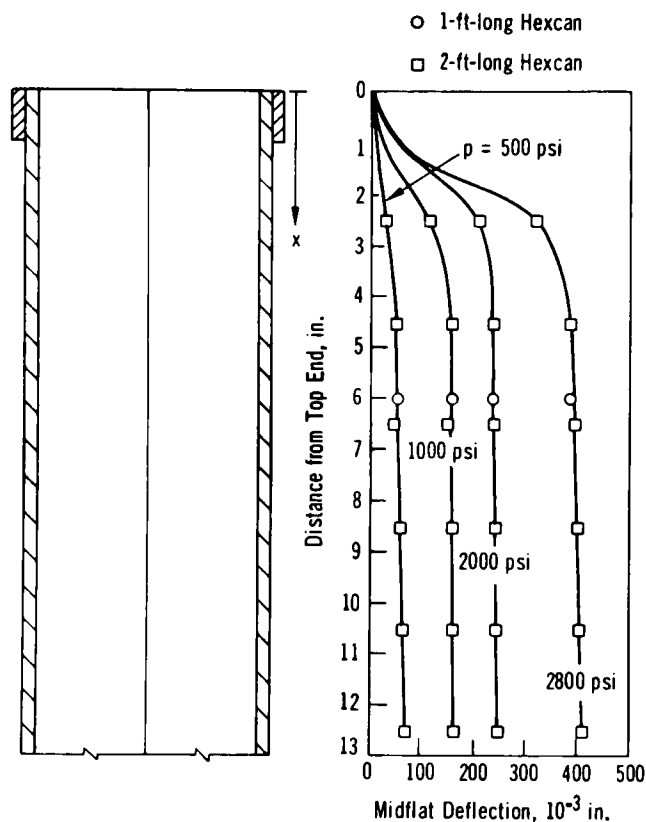


Fig. 8

Effect of Test Length upon Deflection Profiles in Axial Direction of Annealed Hexcan (1 in. = 2.54 cm; 1 ft = 30.48 cm; 1 psi = 6.895 kPa). ANL Neg. No. 900-75-212.

Results of the internal pressurization of annealed and nominally 20%-coldworked hexcan tests are shown in Figs. 9-11. Figure 9 shows the midflat deflections for both materials as a function of internal pressure. The differences in the graphs are directly attributable to the higher yield and ultimate strength of the 20%-coldworked duct. Also, because 20%-coldworked steel fractures at a significantly lower local strain value than the annealed material, the 20%-coldworked duct failed at about 2400 psi (16.5 MPa) while the annealed hexcan withstood a pressure of about 4500 psi (31 MPa) before failure. Both ducts failed either at or very near a corner of the hexcan, where the highest stress concentrations occur, even though the annealed hexcan, due to its high ductility, had already deformed to a nearly cylindrical shape.

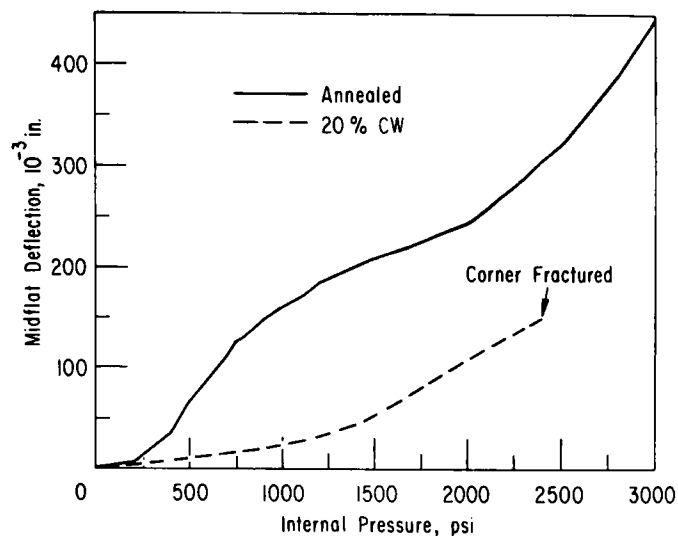


Fig. 9. Comparison of Experimental Midflat Deflections of Annealed and Nominal 20%-coldworked Hexcans under Internal Pressurization at Room Temperature (1 in. = 2.54 cm; 1 psi = 6.895 kPa). ANL Neg. No. 900-75-214.

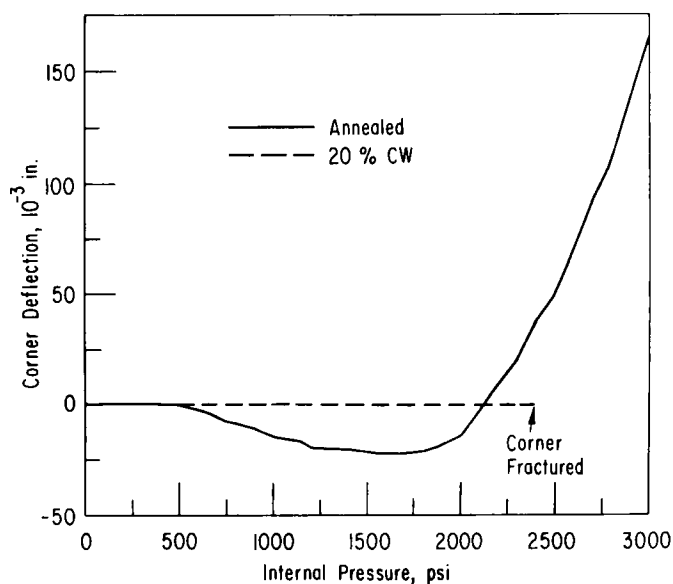


Fig. 10. Comparison of Experimental Corner Deflections of Annealed and Nominal 20%-coldworked Hexcans under Internal Pressurization at Room Temperature (1 in. = 2.54 cm; 1 psi = 6.895 kPa). ANL Neg. No. 900-75-217.

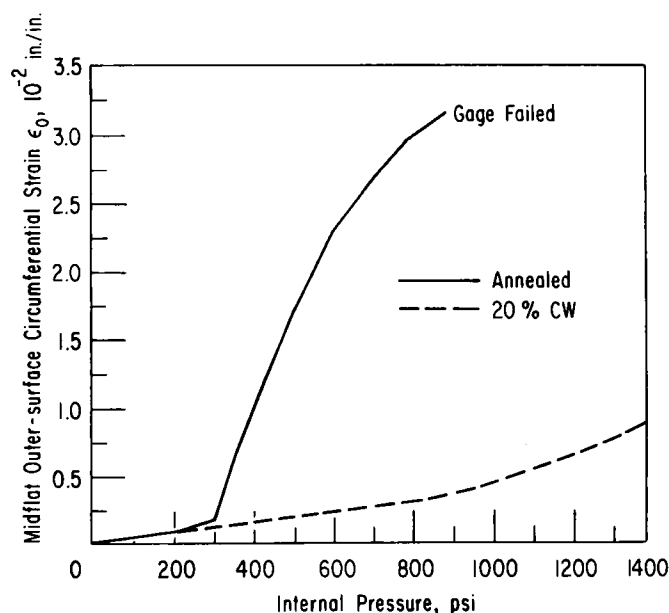


Fig. 11

Comparison of Experimental Midflat Outer-surface Strains of Annealed and Nominal 20%-coldworked Hexcans under Internal Pressurization at Room Temperature (1 in. = 2.54 cm; 1 psi = 6.895 kPa). ANL Neg. No. 900-75-216.

The corner deflections of both ducts are shown in Fig. 10 as a function of the internal pressure loading. The annealed duct clearly shows inward corner movement and then outward movement before failure; the 20%-coldworked duct shows almost no movement before failure. These differences in response can again be traced to the mechanical properties of the ducts. Figure 11 compares the midflat outer-surface strains as a function of internal pressure. Due to the techniques for mounting strain gages in these early tests, the strain measurements were limited to about 3-4% before the strain gage failed. Later improvements in mounting techniques allowed reliable measurements of strain to about 10%.

Similar results were obtained for the internal pressurization of a nominally 50%-coldworked duct section under an internal pressure loading.

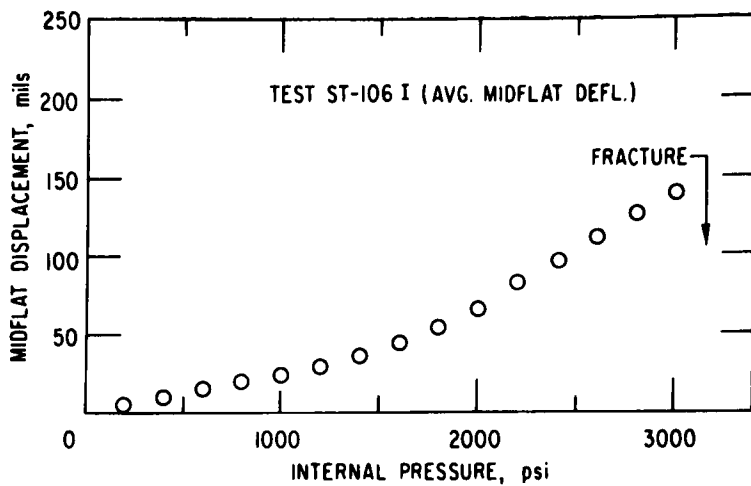


Fig. 12. Measured Midflat Displacement of 50%-coldworked Hexcan under Internal Pressurization at Room Temperature  
(1 mil = 0.0254 mm; 1 psi = 6.895 kPa)

This test was performed, as noted earlier, in order to obtain reliable data on a duct made of material with a reduced ductility, since tensile tests of 50%-coldworked Type 316 stainless steel showed a uniform elongation of only about 2%. However, significant increases in yield strength and ultimate strength also occurred, as would be expected. Figure 12 shows the midflat deflections of the duct as a function of internal pressure. This duct behaved in a much stiffer fashion than either the annealed or 20%-coldworked duct discussed previously. As noted in Table I, this duct failed at an internal pres-

sure of 3100 psi (21.4 MPa). These data represent an average of all six flats. The duct-wall deformation was essentially elastic to a pressure of about 1400 psi (9.7 MPa), at which point a change in slope of the graph of deflection versus pressure occurred because of plastic yielding in the corners. Corner displacement as a function of internal pressure is shown in Fig. 13. This graph shows that there was a small inward movement of the corner during the test before failure, and that plastic yielding in the corner was initiated at a pressure of about 1400 psi (9.7 MPa). Figure 14 shows the average inside midflat strain and Fig. 15 the outside midflat strain as functions of internal pressure. These graphs indicate that the hexcan flat was definitely in a bending

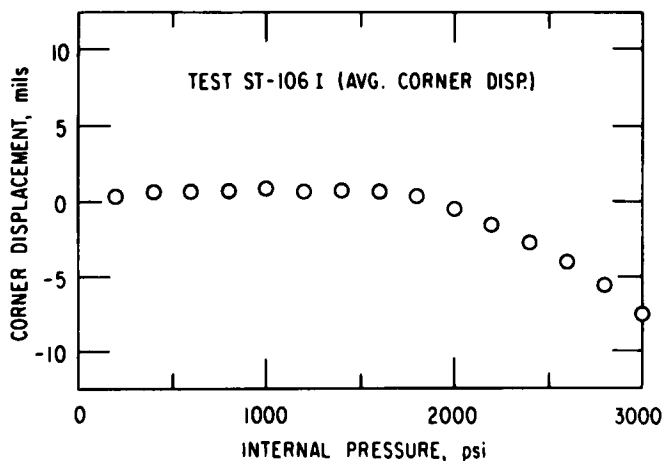


Fig. 13. Measured Corner Displacement of 50%-coldworked Hexcan under Internal Pressurization at Room Temperature  
(1 mil = 0.0254 mm; 1 psi = 6.895 kPa)

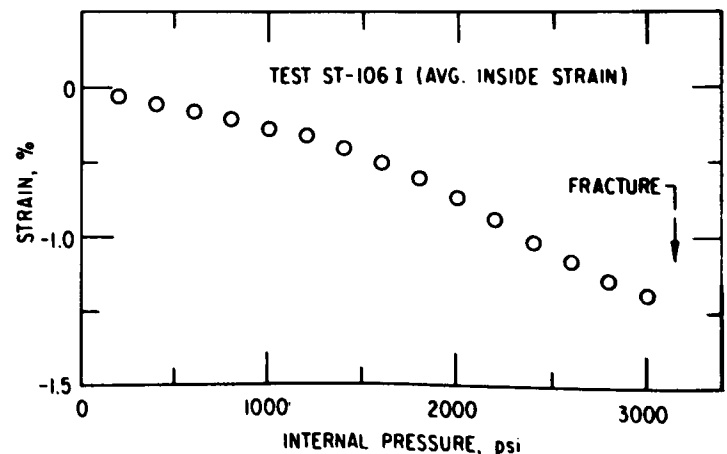


Fig. 14. Measured Strain at Inner Midflat Surface of 50%-coldworked Hexcan under Internal Pressurization at Room Temperature  
(1 psi = 6.895 kPa)



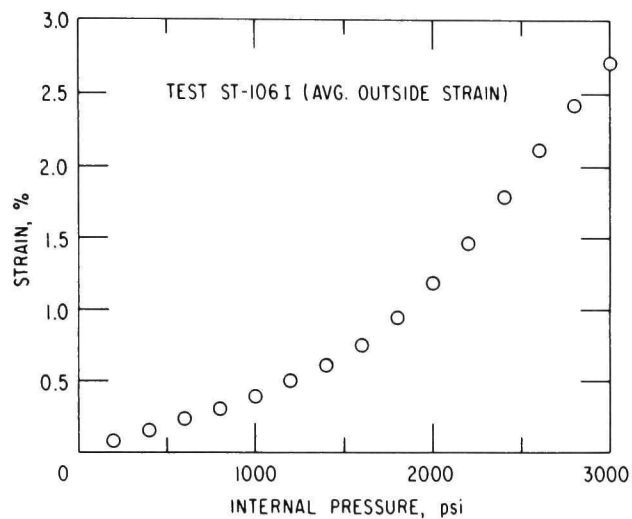


Fig. 15

Measured Strain at Outer Midflat Surface of 50%-coldworked Hexcan under Internal Pressurization at Room Temperature (1 psi = 6.895 kPa)

mode due to the uniform load, with an inside compressive strain, while the outside surface was in tension. Again, these curves represent the average of six measurements.

The condition of the fractured corners for the tests using annealed, and 20%- and 50%-coldworked ducts are shown in Figs 16-19. The final shape

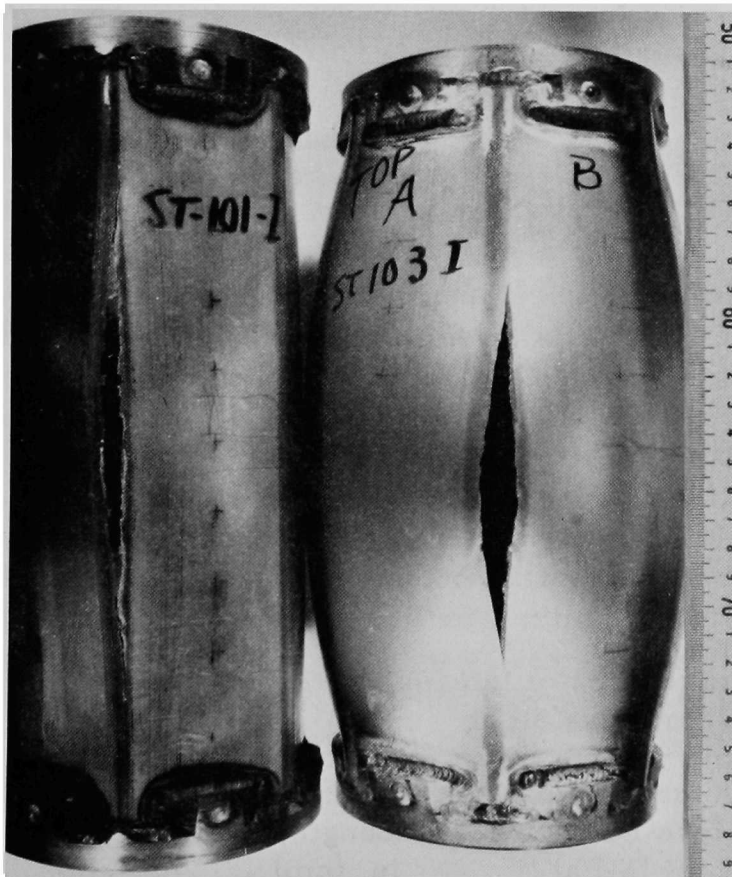


Fig. 16. Annealed and Nominal 20%-coldworked Test Hexcans Internally Pressurized to Failure. Neg. No. MSD-60431.

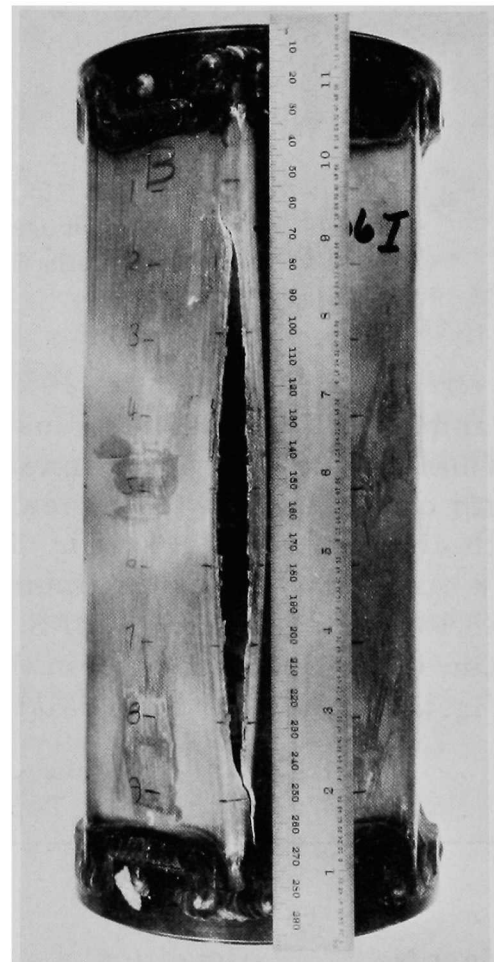


Fig. 17. The 50%-coldworked Hexcan Internally Pressurized to Failure. Neg. No. MSD-61132.

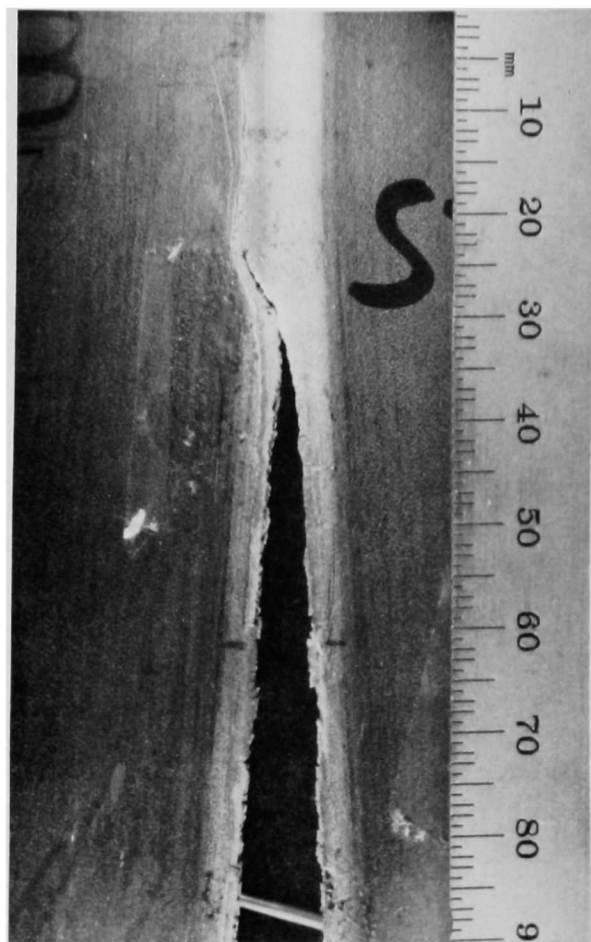


Fig. 18. Detail of Upper Crack Tip for 50%-coldworked Hexcan Internally Pressurized to Failure. Neg. No. MSD-61134.

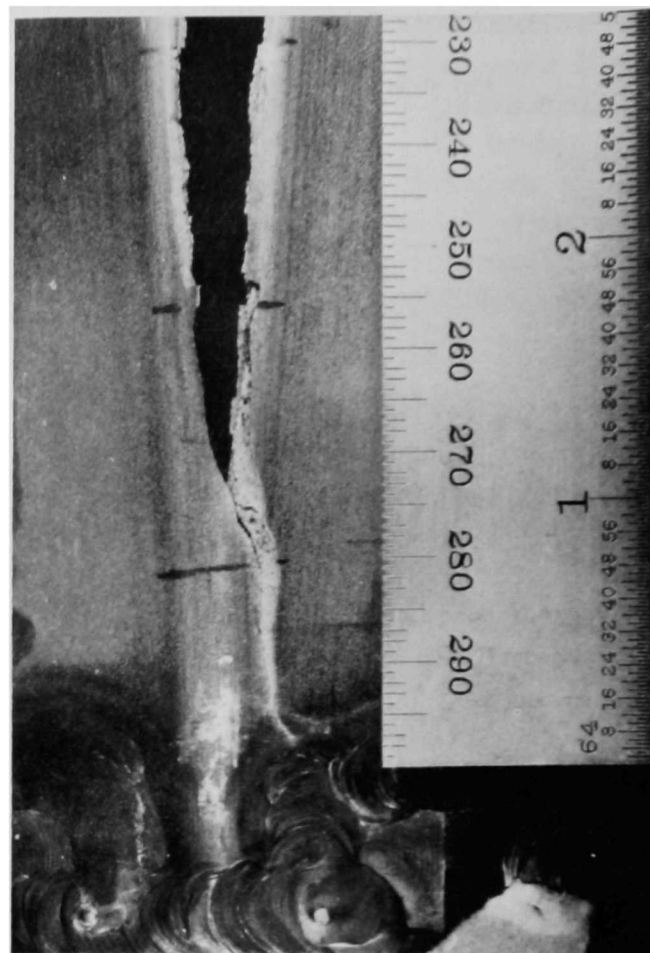


Fig. 19. Detail of Lower Crack Tip for 50%-coldworked Hexcan Internally Pressurized to Failure. Neg. No. MSD-61133.

and corner fracture of the 20%-coldworked duct are shown on the left in Fig. 1c; the annealed Type 316 stainless steel duct is shown on the right. The significant ballooning out of the annealed can before failure is readily noted. The length of the split in the annealed hexcan was about 5.7 in. (14.5 cm) and the width about  $1/2$  in. (1.3 cm). The 20%-coldworked duct fracture was 7.4 in. (18.8 cm) long with a maximum fracture width of about  $1/4$  in. (0.6 cm). A much longer crack length of 8.9 in. (22.6 cm), with a maximum width of about  $3/8$  in. (0.95 cm), appears in the photograph of the 50%-coldworked duct shown in Fig. 17. These fracture data are summarized in Table II.

TABLE II. Fracture Characteristics of Internally Pressurized Type 316 Stainless Steel

Test No.	Material Condition	Approximate Failure Pressure, psi (MPa)	Fracture Length, in. (cm)	Fracture Width, in. (cm)
ST-103I	Annealed	4500 (31.0)	5.7 (14.5)	$1/2$ (1.3)
ST-101I	20% coldworked	2400 (16.5)	7.4 (18.8)	$1/4$ (0.6)
ST-106I	50% coldworked	3100 (21.4)	8.9 (22.6)	$3/8$ (0.95)

The data tabulation in Table II show that the crack length increased as a function of the coldworking of the duct material. This essentially corresponds to reduction in the ductility of the material. Note that, in the test of the 50%-coldworked duct, the fractures terminated near, or in, the heat-affected welding zone and may thus have been arrested by significant material-property changes. The crack tips in test ST-106I are shown in Figs. 18 and 19. Another characteristic of the fractures noted in the hexcans is that the center portion of the fracture appeared to occur due to a tensile stress, whereas near the ends, a transition to shear occurred. As the ductility of the ducts decreased, the tensile zone increased, while the shear zone decreased as a proportion of the total fracture length.

Although the fracture lengths increased monotonically with increasing coldwork, no corresponding pattern was seen in the failure pressure. Increasing the coldworking has two counterbalancing influences. The yield stress is increased, making the hexcan "stronger" in the sense that the elastic range is increased and the material more stiffly resists deflections. On the other hand, the material becomes increasingly brittle in that the capacity for local relieving of stress concentrations by plastic flow is diminished, and fracture will occur at much lower local strains. Because of these opposing influences, there is no assurance that the capacity of the hexcan to withstand pressurization will vary monotonically with coldworking. This, of course, does not include the effect of local material cracks, dents, or other undetected flaws. The data in Table II suggest that the 20%-coldworked can is "weaker" than both the more ductile annealed and the more brittle 50% coldworked hexcans. A generalization cannot be made without further study. It is possible that the strong coldworking gradients in the 20% hexcan have a tendency to weaken the material and induce premature failure. The properties of both the annealed and 50%-coldworked hexcans were much more uniform. It is also possibly that undetected microflaws contributed to a premature fracture. Fracture phenomena were not of major concern in these tests, and much more intensive analysis and testing are required to explain the detailed mechanics of the fracture relationships.

Several tests were also performed to determine the response of the subassembly ducts to external pressurization. It was expected that since the system was essentially in a metastable condition, the hexcan would probably collapse in an asymmetric mode that would not necessarily correlate with calculations which assume symmetric collapse. These test results are discussed in Chap. V, where the comparisons are made.

### III. THE COMPUTER CODE

A major objective of the experimental work is to evaluate the performance of the finite-element, structural-analysis computer code STRAW by comparisons of computed deflections and strains with actual test results. In the initial phase of the experimental program, sample hexcan sections were subjected to hydrostatic loading conditions. In these tests, the pressure was slowly increased to avoid inertial effects; at any instant, the deformed hexcan configuration satisfies static-equilibrium conditions. As the pressurization was progressively increased, the deflections and strains were continuously monitored at selected locations, and pressures were recorded.

In the hydrostatic experiments, the deformations were maintained essentially two-dimensional in a test region midway between the ends of the hexcan. The test region is sufficiently remote from the ends so that possible variations in the axial or  $z$  direction due to end effects are negligible. Of course, since the hexcan is not axially symmetric, the deflections and strains vary in the circumferential  $\theta$  direction. Also, stress and strain distributions occur through the hexcan wall thickness (i.e., in the radial  $r$  direction), so that in terms of a conventional  $(r, \theta, z)$  cylindrical-coordinate system, variations occur in the radial  $r$  and circumferential  $\theta$  directions, and conditions over the test section are uniform in the  $z$ -direction. Hence, the shell equations describing the deformation of the hexcan walls do not involve  $z$ ; only  $r$  and  $\theta$  appear as independent spatial variables.

For the dynamic conditions, the time  $t$  appears as a third independent variable, but according to convention the problem is still referred to as "two-dimensional" when only two spatial dimensions are involved. In this sense, the STRAW code is a two-dimensional, dynamic, finite-element code. A three-dimensional extension of STRAW, called SADCAT, has been developed at Argonne National Laboratory to treat variations in the axial direction (see Appendix A).

Variations in the  $z$  direction were minimized by maintaining a uniform pressure loading in the  $z$  direction and by restricting attention to only those sections sufficiently remote from end effects. The loading was automatically axially uniform for the hydrostatic case, as the pressure was uniform everywhere. For the dynamic case, to be investigated later in the program, elimination of pressure gradients in the  $z$  direction presented a problem. In the dynamic test program a pressure source was developed consisting of a tube extending along the axis from end to end of the test hexcan. Explosive-product gases escaping from ports uniformly distributed along this line source created a pressure pulse with small variations in the  $z$  direction at any instant of time. The resulting pressure loading in the axial direction will, of course, rise and fall uniformly with time. The line source must not only be nearly uniform in the axial direction, but must also be centrally located to maintain two-dimensional conditions. If the line source is eccentrically located, the loading

will be greater on one side of the hexcan than the other, and the entire hexcan will bend along its length as a beam fixed at its ends. As a result, for an eccentrically positioned line source, even if axially uniform discharge conditions are maintained, a three-dimensional code such as SADCAT will be required to compute the deformations. In any case, whether static or dynamic, the SADCAT code would be required to compute deformations in the end regions.

In this report, attention is focused upon comparing STRAW-code computations with hydrostatic-test results. A second report will treat the dynamic-test program. Analysis and interpretation of the hydrostatic-test data precede examination of the dynamic-test data for several reasons. The most obvious reason for first performing the hydrostatic experiments is that the test conditions are clearly defined and much more simple than for the dynamic tests. Unlike the dynamic tests, the hydrostatic pressurization will be distributed perfectly uniformly, and at any instant the pressure can be accurately measured at a single point. For the dynamic tests, perfectly uniform burning of the charge and uniform discharge of the combustion gases throughout the length of the line source present difficult flow-control problems. Pressure-wave reflections at the hexcan ends will introduce further uncertainties into the assumption of uniform pressure loading in the axial direction.

The hydrostatic-test data are more reliable also because possible ambiguities in the transient response of the instrumentation system will be minimized. Static deflections and strains can be accurately measured, and the pressurization process can be stopped at any stage to check out any measurements as carefully as desired.

Another major reason for performing the hydrostatic tests before the dynamic tests is to first evaluate the influence of the material properties upon the sensitivity of the hexcan deformation. Our tests have established that the yield point and the strain-hardening, plastic-flow, region of the stress-strain curve have a strong influence upon the amplitude of the hexcan response. The role of work hardening and of variations in the yield point can be isolated in the hydrostatic tests from the dynamic inertial effects and the strain-rate effects.

Although the STRAW code was designed to solve dynamic problems, it is also quite suitable to treat static problems. The code computes the deformation response of the hexcan at successive time intervals throughout the varying pressure load. The method used in the STRAW code is referred to as an "explicit" computational procedure. This method is an alternative to the so-called "implicit" procedure. In the implicit procedure, the simultaneous solution is obtained at each time interval for the complete system of equations describing the dynamic equilibrium conditions (i.e., force equals mass times acceleration) at every point. This procedure requires that all quantities pertinent to the computation be stored in the computer for every point. The explicit procedure is more efficient in terms of computer-storage

requirements because the equations at a given local point are solved directly; the computation then proceeds to the next point without storing intermediate values. Solving the local equations in this manner at all the points at a given time interval completes a "computational cycle." For the next time interval the computation is again repeated at each of the points.

In this procedure, the solution of the equations at a local point is only approximate. The accuracy of the approximation depends upon choosing a sufficiently small time increment to control accumulation of the computational error as the configurations are traced from an initial known state to the desired final state. The advantage of the explicit method is its simplicity in solving directly the limited number of local equations in each computation rather than the entire simultaneous global system of equations. Much less computer storage is required than for the implicit method. The disadvantage of the explicit method is that questions of numerical convergence are more critical and many more computational cycles are required because the time increment must be kept much smaller.

The concept of "path dependence" of the computation is important to understand because it demonstrates the necessity to perform experiments to establish the validity of the computational procedure. There is at present, no analytical means for proving that the computation converges to the correct description of the actual physical process. For a dynamic problem, the configuration depends not only upon the loading at that instant, but also upon the previous loading history. This means that the specific loading at any given instant does not uniquely determine the geometrical configuration of the hexcan. As an aid to understanding this fact, it is convenient to visualize the processes involved by reference to a "phase space" in which the geometrical configuration can be regarded as a function of the loading. The configuration (i.e., the "value" of the function) for any given loading depends upon the "pathline" of previous states that the hexcan has undergone before the given loading. Hence, for dynamic loading, we say that the configuration is "path-dependent," and to compute the configuration it is necessary to compute all the prior states starting from the zero loading condition.

An exception can be noted for the very special circumstances in which the loading would proceed so slowly that inertial effects can be ignored and the material nowhere exceeds the elastic limit. The deformation process would then be "reversible" in the thermodynamic sense, and the resulting configuration would be a unique function of the loading. In this case, the deformation process is "path-independent" and the configuration state at any instant is a "point function." Computation of intermediate states would then be unnecessary. It would be sufficient simply to satisfy the static-equilibrium equations to obtain a solution. An implicit code would be most appropriate to solve this type of problem. Unfortunately, for the hexcan problem, stress concentrations in the corner regions will very quickly lead to plastic-flow conditions, so that, even for very slow-loading conditions, under which inertial efforts are negligible, the deformations will not be path-independent.

We see then that, for a hydrostatic problem that involves inelastic deformations, there is no advantage in using an implicit code, because the path dependence requires that all intermediate states be computed. Hence, the explicit STRAW code is adequate to compute hydrostatic as well as dynamic problems, and a meaningful basis for evaluation of the code performance can be derived from correlations with hydrostatic test results.

The necessity of running experiments to establish the range of accuracy of code computations for path-dependent problems should be emphasized. Such validating experiments are required, even when it appears that the calculations are converging. The absence of obvious numerical instabilities, as evidenced by diverging numerical oscillations or a rapid unrealistic growth of a computed quantity, is no assurance that the numerical solution is converging to the correct description of the physical events. Satisfying convergence criteria imposes a necessary but not a sufficient condition for a correct answer. For example, if an energy-balance condition is violated, it is evident that the computation is diverging. However, satisfying an energy criterion does not guarantee that the computation is correct for a path-dependent process because the solution is not unique.

As the computation proceeds, errors can be expected to grow, not only for an explicit computational procedure, but also for an implicit procedure in which the system of equations is solved exactly at each time cycle. Errors occur because it is possible to "March ahead" in time only by finite time steps. The computed current configuration is an approximate extrapolation from the preceding state. Although the error for a single step can be made arbitrarily small by choosing a sufficiently small time interval, the number of computational cycles required to reach a specified time will increase. There is no analytical way to fix an upper bound for the accumulated error. Only by comparisons with experimental results can the degree of divergence be gauged.

It has been noted that path dependence arises because of dynamic effects (e.g., strain-rate dependence and nonequilibrium) and because plastic deformations are irreversible. Geometric considerations can also influence path dependence. For example, constraining a motion to one degree of freedom may make the motion path-independent. If a rod is loaded in a tensile test machine, the resulting uniaxial stress-strain relationship is uniquely determined in the range up to the ultimate stress point provided the strain increases monotonically, and slowly enough to avoid significant strain-rate effects. The deformation of the rod is essentially constrained to a one-dimensional rectilinear motion. In the STRAW code the finite elements are modeled as beams that consist of independent longitudinal layers or "fibers" that are uniaxially stressed just as are the tensile specimen. Hence, these STRAW-code fibers have a unique stress-strain relationship provided there are no stress reversals.

Consider, on the other hand, the hexcan wall sector with two geometrical degrees of freedom, rather than constrained to rectilinear motions. Although the sector may be loaded so that stress reversals do not occur, the final equilibrium shape will not be a point function, but will depend upon the loading history. This means that, because the STRAW code allows two degrees of freedom, the deformation of the hexcan is path-dependent, even for hydrostatic pressurization. All intermediate states must be computed from the initial unloaded state to the final hydrostatic state, whether the code is explicit (as STRAW is) or implicit.

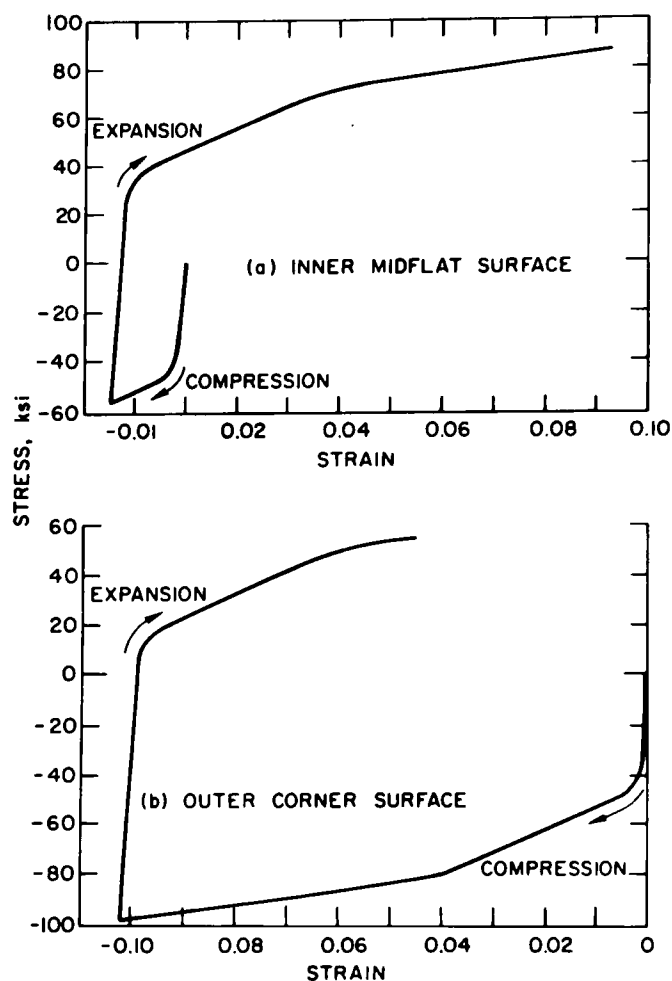


Fig. 20. Examples of Strain Reversals at Corner Outer Surface and Midflat Inner Surface for Internal Pressurization of Annealed Hexcan at Room Temperature (1 ksi = 6.895 MPa). ANL Neg. No. 900-5323.

apparently lies partially in the additional degree of freedom, and correspondingly greater complexity, of the SADCAT computational procedure.

The main conclusions to this somewhat extended discussion can be summarized as follows:

1. To calculate the deformation of a hydrostatically pressurized hexcan, all the intermediate states, starting from the unloaded can, must be computed.
2. Because of the state path dependence there are no reliable measures of convergence, so the accuracy of the computed results must be established by experiments.

It should be remarked that as the hexcan is pressurized, strain reversals occur at the outside surface of the corner regions and at the inner surface at the midflat, as shown in Fig. 20, so that the uniaxial stress-strain relation is also not unique. This additional nonuniqueness contributes further to the path dependence and consequently to possible further divergence from the true solution.

Similarly, the introduction of a third degree of freedom into the problem will introduce an even greater path dependence and a greater tendency for the computations to diverge. The SADCAT code follows a three-dimensional computational procedure. When the code is applied to a nominally two-dimensional problem, it appears (see Fig. 21) that the computation diverges slightly more than for the application of the STRAW code to the same problem. The explanation



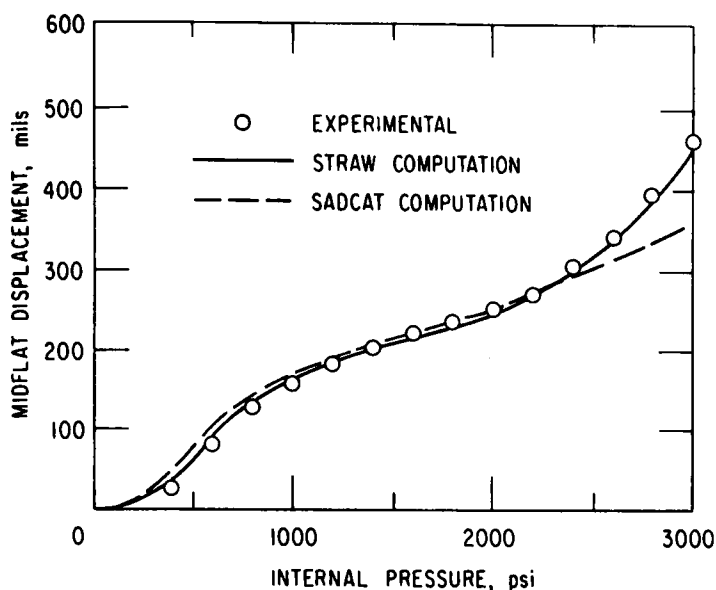


Fig. 21. Comparison of Measured Midflat Displacements with STRAW and SADCAT Computations for Internally Pressurized Annealed Hexcan at Room Temperature (1 mil = 0.0254 mm; 1 psi = 6.895 kPa)

For further discussion of the technical details of the STRAW code and of the three-dimensional SADCAT code, see Appendix A and Refs. 1-5.

#### IV. MECHANICAL PROPERTIES OF THE STEEL

The mechanical response of the hexcan to pressure loads is strongly dependent upon the material properties of the steel. The material properties that influence the deformation response are represented by the stress-strain relationship. A graph of the stress-strain relationship may be plotted based upon tensile tests of a Type 316 stainless

steel specimen cut from the hexcan and stretched in a tensile test machine. The initial stress-strain relationship is linear-elastic, but with increasing load the limit of the linear range of slope equal to Young's modulus  $E$  will be reached, and the slope of the stress-strain graph will begin to decrease. This point is called the "proportional limit."

For strains slightly beyond the linear region the material may retain its elasticity, i.e., be nonlinearly elastic in the sense that the original configuration will be restored with no permanent deformation upon removal of the load. However, plastic flow, which produces permanent deformation, will quickly ensue under further extension. The point at which plastic flow is defined to start is called the "yield point." Since plastic yielding begins very close to the proportional limit, the "yield stress" will be defined on the stress-strain graph as the point at which the graph begins to deviate from the initial elastic straight line. For Type 316 stainless steel, as for many real materials, this point is not easily distinguished because the transition in slope is very gradual. Because of this difficulty in determining precisely where the line begins to change slope, a common practice is to define a 0.2% "offset yield" at the point where, after release of the load, the tensile specimen retains a permanent 0.2% residual strain.

The yield stress for the Type 316 stainless steel can vary over a wide range, depending upon the ambient conditions, and upon the history of the metallurgical and forming processes that the steel undergoes. The hexcan is formed from a hollow, circular cylinder. The cylinder is drawn through a succession of dies, which simultaneously shape the hexcan corners and reduce the wall thickness. The material is hardened during the drawing process. The degree

of hardening is related by an empirical correlation (see Fig. 22) to the "cold-working," which is measured by the percent reduction in the cross-sectional

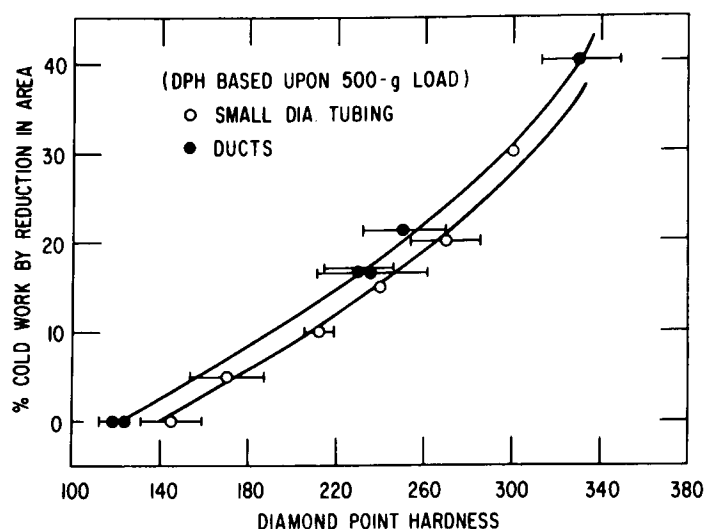


Fig. 22. Empirical Correlation of Coldworking and Hardness for Type 316 Stainless Steel (from Paxton et al., HEDL 7306-51.7)

nealing, the final draw reduces the cross-sectional area of the wall to the desired coldworked level, which should be uniform over the circumference of the cylinder, since the corner and the midflat wall thicknesses are equally reduced. The measurements of diamond-point hardness (DPH) shown in Fig. 23 for the nominal, as-received 20%-coldworked hexcan show that the hardness is not quite as uniform as expected, but that a hardness profile exists with an increasing gradient from the midflat to the corner. An averaged gradient is shown in Fig. 24. The corner has DPH values of about 310 and values at the midflat of about 280. The DPH value of 280 corresponds to a

area. The corner also undergoes additional hardening due to the bending work, so that a gradient of increasing hardening extends from the midflat to the corner. However, to reduce the gradient, between each step of the drawing process, the steel is annealed to remove all work hardening developed by the previous draw.

Before the last draw, the hexcan shape is fully developed and the corners have undergone all the required bending. Hence, the last draw should produce work hardening due only to a final reduction in the wall thickness. After a final an-

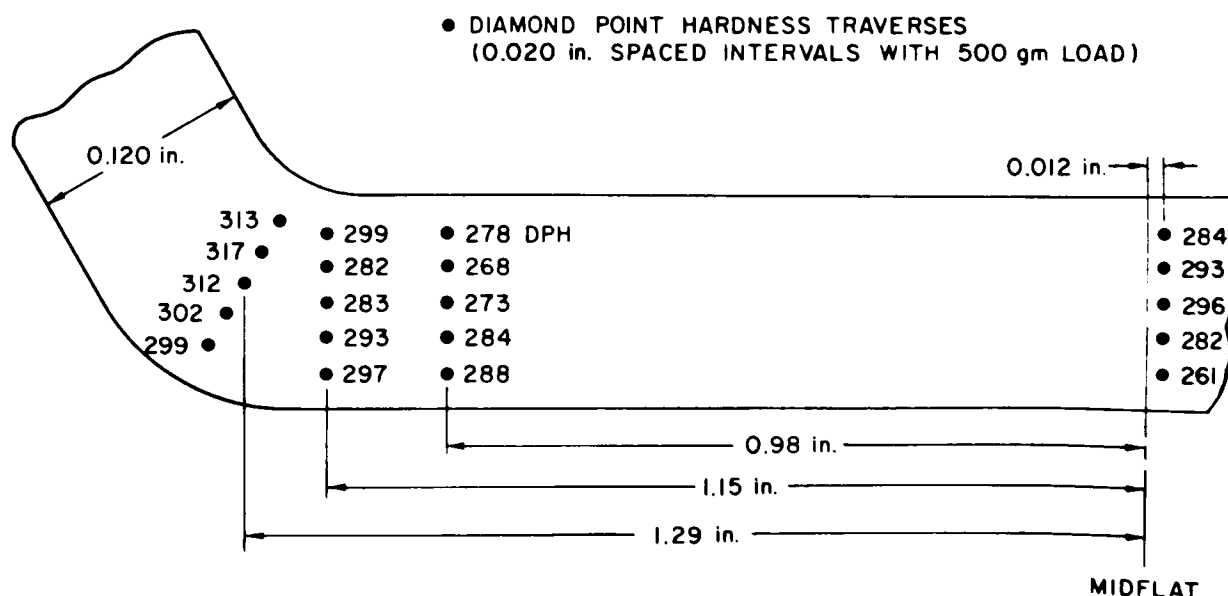


Fig. 23. Survey of Diamond Point Hardness of Sample over Wall Thickness for a Nominal 20%-coldworked Hexagonal Duct in Condition Received from Vendor (1 in. = 2.54 cm)

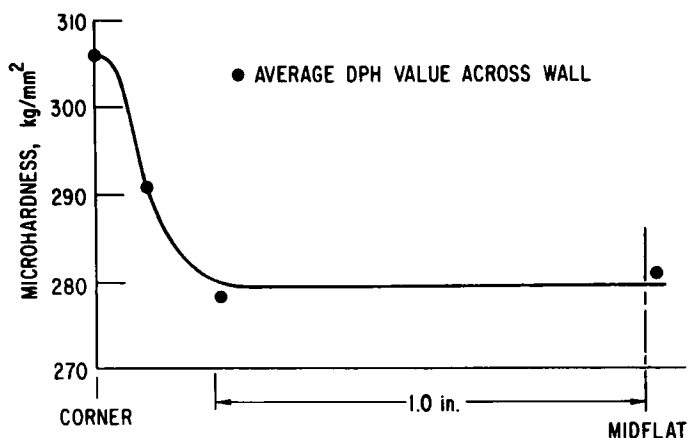


Fig. 24

Average Hardness Profile from Mid-flat to Corner for Sample, Nominal 20%-coldworked, Hexagonal Duct Section (1 in. = 2.54 cm)

coldworking greater than 20% (see Fig. 23), and the higher value in the corner indicates that residual strain hardening may remain from earlier forming draws.

Based upon the DPH profile, we can infer that the nominal 20%-coldworked hexcan is harder and stiffer, with residual coldworking in excess

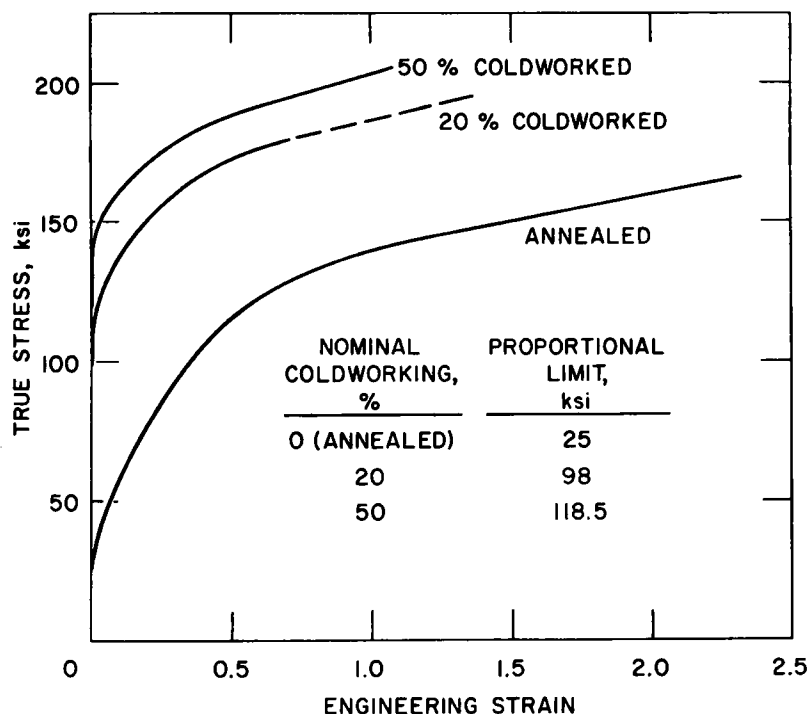


Fig. 25. Graphs of True Stress vs Engineering Strain for Annealed and 20%- and 50%-coldworked Type 316 Stainless Steel Test Hexcans (1 ksi = 6.895 MPa)

of 30% in the corners. The term "stiffness" refers specifically to the relative magnitude of the yield stress at the elastic limit of the steel. The stress-strain graphs in Fig. 25 show that the material becomes stiffer (and less ductile) as the percent coldworking, or correlated work hardening, is increased.

The hydrostatic tests have demonstrated that the value of the yield stress has a strong influence upon the magnitude of the hexcan deflection produced by a specified pressure loading. Lowering the yield stress will obviously increase the deflection, and stiffening the hexcan material will reduce the deflection. To

determine the sensitivity of the deflections to variations in ductility, a series of hexcans was tested over a range of mechanical material properties. The maximum ductility for the test series was obtained by solution-annealing an as-received 20%-coldworked test section. The yield point was lowered from

98 to 25 ksi (675.7 to 172.4 MPa) for the annealed specimens. A stiff hexcan specimen was specially fabricated. A new set of dies was designed to modify the wall-thickness reduction between successive draws. The final draw produced a 50% rather than the usual 20% coldworking. The yield stress was then raised from 98 to 119 ksi (675.7 to 820.5 MPa). In this way, a range of ductility conditions was made available for testing.

Graphs of the stress-strain relationships for the annealed, the nominal 20%, and the 50%-coldworked Type 316 stainless steel hexcan test specimens are shown in Fig. 25. The annealed material is quite ductile, and the annealed tensile specimen was drawn out to a local strain of about 230%. Compared with this final strain at fracture, the strain at the elastic limit is only about 0.089% and can scarcely be detected on the scale shown in Fig. 25. The initial, linear-elastic range of the graph appears as a straight, almost vertical, line with a high slope equal to a Young's modulus  $E$  of  $28 \times 10^6$  psi ( $193 \times 10^6$  kPa). When the strain increases beyond the proportional limit, the slope of the graph, or tangent modulus  $E_{tan}$ , monotonically declines. For a perfectly plastic material, the slope would change discontinuously from the elastic value  $E$  to a zero value at the proportional limit. No further increase in the

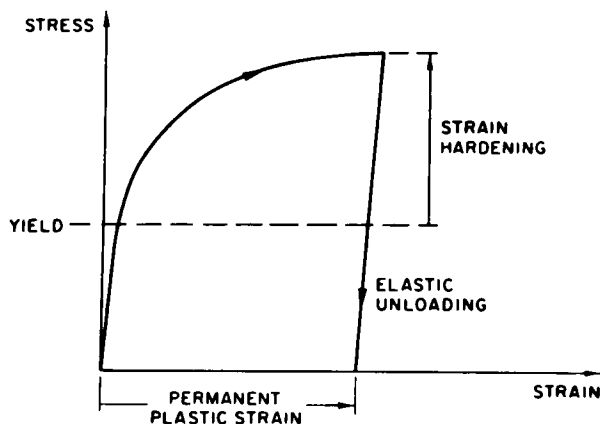


Fig. 26. General Characteristics of Stress-Strain Graph

stress would occur; the yield-stress value would be maintained for plastic strains. However, the large stress increase measured after the yield point shows that considerable strain hardening occurs for the Type 316 stainless steel.

Note that the stress-strain relationships shown in Fig. 25 for the tensile-test specimens are for a monotonically increasing strain. If the specimen were unloaded, the stress would be relieved along a linear-elastic line, as shown in Fig. 26. The residual permanent strain is a measure of the plastic flow. Any incremental strain in the strain-hardening plastic-flow range of the graph can be resolved into plastic and elastic components, as shown in Fig. B.4 of Appendix B. The "local plastic slope"  $E_p$  is defined by the plastic-strain component (see Eq. 13, Appendix B), and since the plastic-strain component is much larger than the elastic-strain component, the plastic slope  $E_p$  is a good approximation to the actual tangent slope  $E_{tan}$  of the graph (defined by the total strain component).

The influence of coldworking upon the mechanical properties of the hexcan steel is shown in Fig. 25. An increase in coldworking raises the yield stress, making the hexcan considerably more resistant to deflections. This influence is demonstrated in Table III, which compares the peak midflat

deflections for three test hexcans under an internal pressurization of 2400 psi (16.5 MPa). The three hexcans span a range of yield stress from 25 ksi (172.4 MPa) for the annealed steel to 119 ksi (820.5 MPa) for the 50%-coldworked steel. The stress-strain curves for the three hexcan materials are shown in Fig. 25.

TABLE III. Effect of Coldworking upon Properties of Type 316 Stainless Steel

Coldwork, %	Yield Stress, ksi (MPa)	Peak Radial Deflection at 2400 psi (16.5 MPa), mils (mm)
0 (annealed)	25 (172.4)	300 (7.62)
20	98 (675.7)	148 (3.76)
50	119 (820.5)	85 (2.16)

Table III shows that the 50%-coldworked steel is much stiffer than the annealed steel. The peak deflection appears roughly to vary inversely with the yield stress. Under actual reactor operation, the ambient conditions will strongly influence the mechanical material properties. The elevated temperatures lower the yield stress; the embrittling effects of irradiation, which accumulate over a longer time period, will have the opposite effect, tending to raise the yield stress. The room-temperature tests presented in this report are not intended to model the in-reactor operational hexcan. Rather, test results were compared with STRAW computations to verify the code performance.

Because of the sensitivity of the hexcan response to the stress-strain relationship (see Fig. 27), in particular to the value of the yield stress, it is

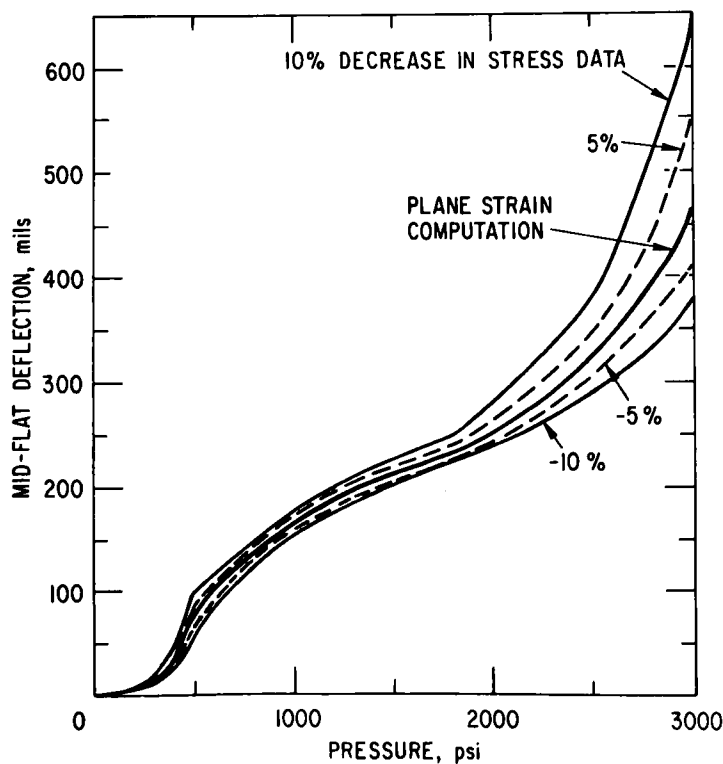


Fig. 27

Sensitivity of Midflat Deflections to Variations in Material Properties for an Annealed Type 316 Stainless Steel Internally Pressurized Hexcan (1 mil = 0.0254 mm; 1 psi = 6.895 kPa). ANL Neg. No. 900-5313 Rev. 1.

apparent that the actual mechanical properties of the steel in each test hexcan must be established. To accomplish this, sample tensile coupons were cut from each test hexcan and the mechanical properties of the sample were measured by the Materials Science Division at Argonne National Laboratory. The determination of the stress-strain relations shown in Fig. 25 is described below.

#### A. Annealed Type 316 Stainless Steel

The hexcan shape is formed by successive draws through a series of dies. The first draw reduces the wall thickness and leaves the steel in a coldworked state. This coldworking is then removed by annealing before the next draw. After completion of the final drawing, the nominal coldworking is 20%, as based upon the area reduction of the last draw.

To achieve a higher coldworking of 50%, a new set of dies was designed so that the final draw reduced the cross-sectional area by 50%. The test hexcans referred to as "annealed" were obtained from ducts for which the

final drawing leaves the steel in the nominal "as-received" state of 20% coldworking. The coldworking was then removed by solution-annealing at 1850°F (1010°C) for 10 min, followed by a slow cooling.

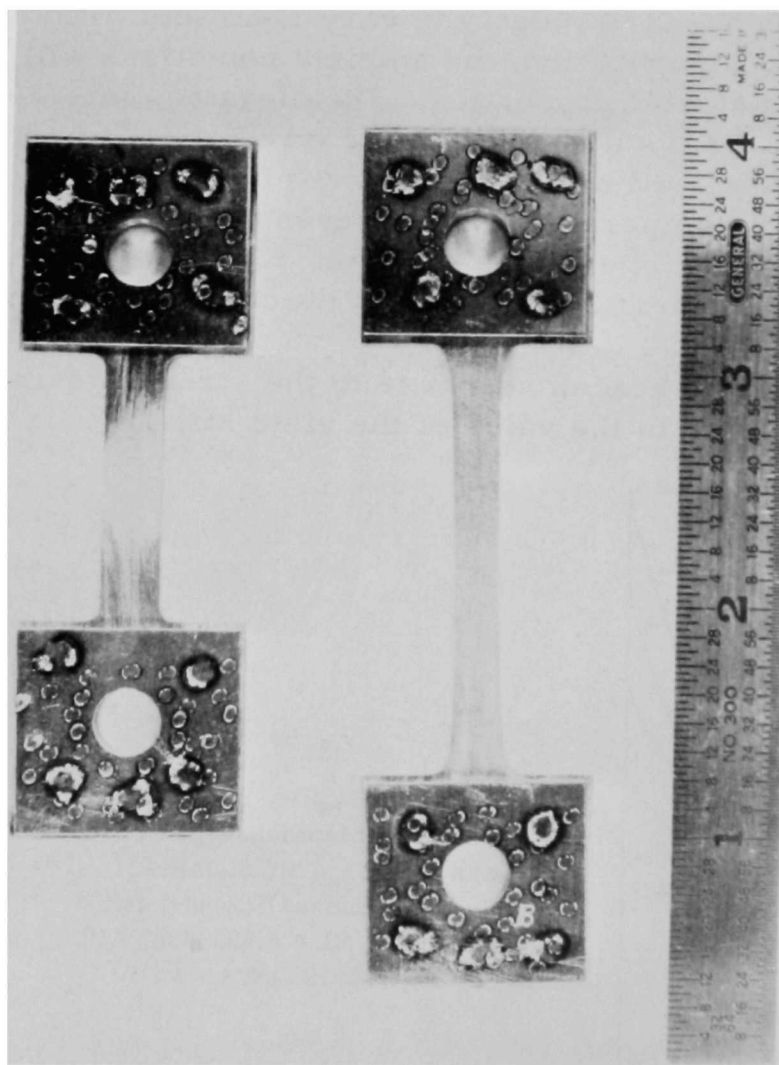


Fig. 28. Annealed Type 316 Stainless Steel Tensile Specimens before and after Testing. Neg. No. MSD-59522.

Before the test hexcans were subjected to pressurization experiments, a 3-in. (7.62-cm)-long sample section was cut from each test hexcan. All sectioning was performed with cutoff wheels to avoid the introduction of stray hardening. Tensile coupons were then machined from alternate flats of the sample section. The shape of the tensile specimen is shown in Fig. 28. From one of the remaining flats of the sample section, a transverse section was prepared for a determination of the microhardness profile. The section was metallographically mounted and carefully polished. Initial grinding was done with a Whirlimet grinder and wet abrasive-paper disks, removing at least 0.5 mm of

metal before a finish grinding with 320- and 400-grit disks. Polishing was done with 500-g weights and Linde A wet alumina on nylon cloth in a Syntron polisher for 2 hr.

The length of the gage section of the tensile-test specimen was chosen to be 1 in. (2.54 cm). Because a further length of 1 in. (2.54 cm) was required at each end for clamping purposes (see Fig. 28), the total sample length removed from the hexcan was 3 in. (7.62 cm). Because of limitations in material availability, longer gage sections were not tested. In addition, the 1-in. (2.54-cm) gage length was convenient because the elongation for uniform strain is directly equal to the engineering strain. Young's modulus could not be accurately determined from the tensile test because the elongation was so small in the elastic range for the short gage section. The conventional nominal value of  $28 \times 10^6$  psi ( $1.96 \times 10^8$  kPa) is representative for Type 316 stainless steel and was assumed for computational purposes. Young's modulus is nearly independent of the strain rate, and the permanent deformations that are of principal concern are not sensitive to the value of Young's modulus. The value of the yield stress is of much greater importance.

Strains were determined from displacements measured with an extensometer mounted directly on the specimen gage section. When the load is increased an unstable point is reached at which the specimen begins to neck down at some section. At this point, the load reaches a maximum and the corresponding stress is called the "ultimate stress." Under further extension the load will diminish. Extensometer measurements made beyond the ultimate point, represent only an average strain over the specimen gage length and are not applicable for the computations since the resulting stress-strain graph is not unique. The local strain beyond the ultimate stress was determined from measurements of the area contraction at the minimum area of the necked-down specimen. The stress-strain tests were run on an Instron tensile test machine operated at a specified constant crosshead speed. The strain data were obtained from an auxiliary X-Y recorder connected to an extensometer and the Instron load circuit. The test data for annealed specimens as reported by the Materials Science Division at ANL are summarized in Table IV.

The tensile-test data shown in Table IV are for specimens taken from four annealed test hexcans (prefix numbers 7-10). For each hexcan, a specimen was taken from each of three alternate flats (i.e., three specimens with suffix labels B, D, and F for each can). As is well known, the rate at which the steel is strained has an influence upon the value of the yield stress. In the tensile tests, the crosshead moves at a small but finite speed. In fact, in the hydrostatic hexcan tests, the hexcans are slowly pressurized so that there are no inertial effects, but a question can be raised concerning the influence of the small but finite strain-rate effects upon the yield-point value of the steel. The assumption is made that the yield stress obtained for the slowest crosshead speed [ $0.02$  in./min ( $8.46 \times 10^{-3}$  mm/sec)] will correspond sufficiently accurately to the yield stress of the hydrostatically pressurized hexcans. The

discrepancy in the actual values should not exceed the scatter [standard deviation of 0.7 ksi (4.8 MPa) for the seven data points at 0.02 in./min ( $8.46 \times 10^{-3}$  mm/sec)] in the tensile-test data. Based upon the limited number of data points at higher crosshead speeds, the slope of the graph (see Fig. 29) of yield stress versus crosshead speed appears to be small, so that variations in yield stress at low strain rates will not noticeably affect the hexcan computations.

TABLE IV. Tensile-test Results for Annealed Type 316 Stainless Steel<sup>a</sup>

Sample	Initial Area, in. <sup>2</sup> (cm <sup>2</sup> )	Crosshead Speed, in./min (mm/sec)	0.2% Yield Stress, ksi (MPa)	Ultimate Strength, ksi (MPa)	Maximum Uniform Strain, %	Final Load, lb (kg)	Aneck, <sup>b</sup> in. <sup>2</sup> (mm <sup>2</sup> )
7-AN-B	0.02991 (0.19297)	0.20 (0.085)	31.4 (216.5)	81.1 (559.2)	53.5	1550 (703)	0.0083 (5.355)
7-AN-D	0.03141 (0.20264)	0.02 (0.008)	29.3 (202.0)	79.3 (546.8)	64	1680 (762)	0.0085 (5.484)
7-AN-F	0.02914 (0.18800)	5.0 (2.117)	39.5 (272.3) <sup>c</sup>	79.8 (550.2)	46	1750 (794)	0.0089 (5.742)
8-AN-B	0.02980 (0.19226)	2.0 (0.847)	31.9 (219.9) <sup>c</sup>	79.2 (546.1)	47.4	1525 (692)	0.0085 (5.484)
8-AN-D	0.03101 (0.20006)	0.02 (0.008)	27.7 (191.0)	78.9 (544.0)	68	1485 (674)	0.0082 (5.290)
8-AN-F	0.03006 (0.19394)	0.02 (0.008)	28.4 (195.8)	79.3 (546.8)	63	1500 (680)	0.0075 (4.839)
9-AN-B	0.03006 (0.19394)	0.02 (0.008)	28.8 (198.6)	80.2 (553.0)	63	1510 (685)	0.0081 (5.226)
9-AN-D	0.02957 (0.19077)	0.02 (0.008)	29.1 (200.6)	81.5 (561.9)	67	1600 (726)	0.0085 (5.484)
10-AN-B	0.02969 (0.19155)	0.02 (0.008)	27.6 (190.3)	78.8 (543.3)	65	1480 (671)	0.0078 (5.032)
10-AN-D	0.03010 (0.19419)	0.02 (0.008)	27.4 (188.9)	78.2 (539.2)	67	2025 (919)	0.0108 (6.968) <sup>d</sup>

<sup>a</sup>Engineering values for samples of rectangular gage section, 0.12 x 0.25 in. (0.3 x 0.6 cm), and 1-in. (2.54-cm) original gage length.

<sup>b</sup>Posttest cross-sectional area at failure site. These cross sections were of concave rectangular shape. Maximum and minimum dimensions were measured with a 0.03-in. (0.7-mm)-thick blade micrometer to calculate average area.

<sup>c</sup>High values due partly to Instron amplifier rate limitation [later test indicated a value of 35 ksi (241 MPa)].

<sup>d</sup>Test stopped before sample failure.

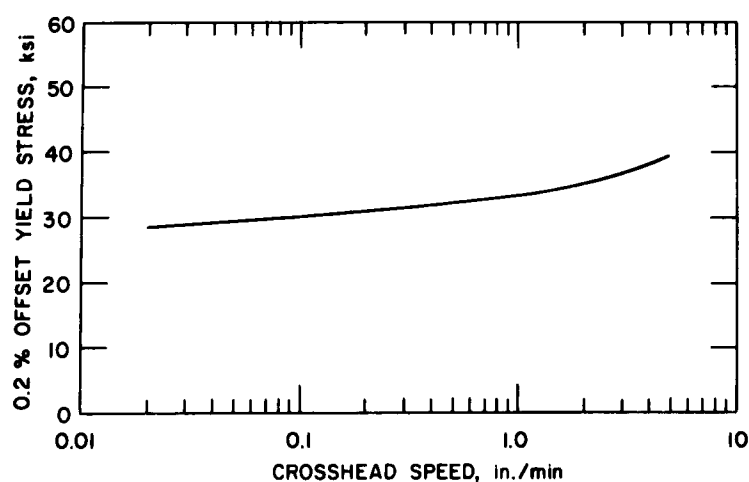


Fig. 29

Estimated Influence of Crosshead Speed upon Magnitude of Uniaxial Yield Stress for Annealed Hexcan Tensile-test Specimens (1 ksi = 6.895 MPa; 1 in./min = 0.423 mm/sec)

An example tensile-test-data plot of load (per unit original area) versus percent elongation of the 1-in. (2.54-cm) gauge section is shown in Fig. 30. The tensile force, as measured with a load cell, divided by the original gage-section average area corresponds to the conventional "engineering stress" for strains up to the point of maximum load. Beyond this ultimate point, the engineering stress as defined by the graph is not applicable for the computations. However, the STRAW code uses the "true stress" (i.e., the load divided by the instantaneous local area) and the engineering strain as input data.



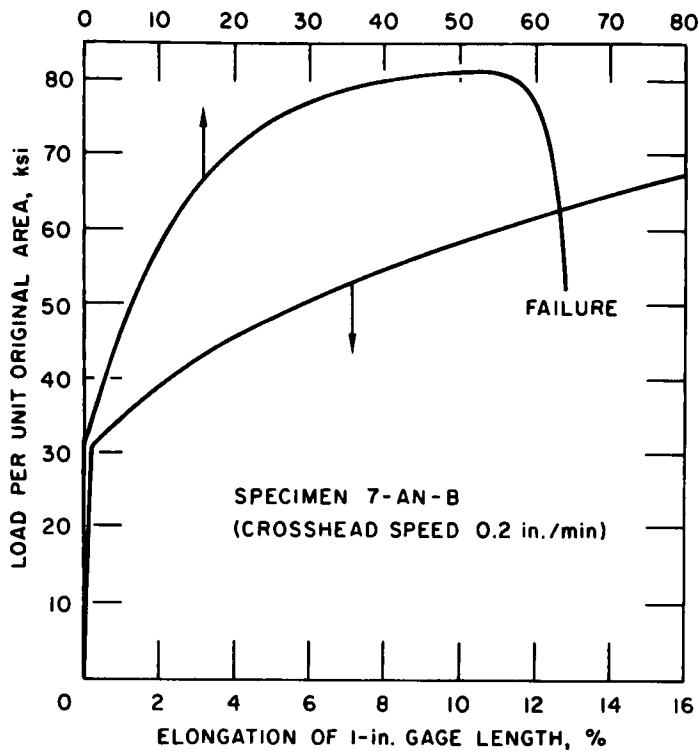


Fig. 30

Tensile-test Data for Unit Load vs Elongation for an Annealed Hexcan Tensile Specimen (7-AN-B), Crosshead Speed Being 0.2 in./min (1 ksi = 6.895 MPa; 1 in. = 2.54 cm; 1 in./min = 0.423 mm/sec)

Up to the ultimate point, the true stress is uniform over the gage length and is derived from the engineering stress by the formula (see Appendix C)

$$\sigma_t = \sigma(1 + \epsilon),$$

where  $\sigma_t$  is the true stress, and  $\sigma$  and  $\epsilon$  are the engineering stress and strain, respectively. The engineering strain is the percent elongation of the gage length of the tensile specimen for uniform strains up to the ultimate point. Beyond the ultimate point, the stresses and strains become nonuniform, and the local true stress is given simply by the load divided by the minimum area  $A$  of the necked-down region.

The engineering strain is determined (see Appendix C) from the measured area  $A$  and the initial gage-section area  $A_0$ :

$$\epsilon = \frac{A_0}{A} - 1.$$

Note that the stress-strain graph shown in Fig. 30 is not unique for strains beyond the ultimate point. For this reason, the load per unit area and percent elongation are not used for computations beyond the ultimate point. The graphs will differ for different gage lengths or cross-sectional areas.

Microhardness surveys were made for each of the four annealed test hexcans listed in Table IV. An example of a diamond-point-hardness (DPH) survey is shown in Fig. 31.

The variations in the hardness values can be attributed to typical fluctuations in such microstructural details as grain boundaries and precipitates.

The trend in the hardness values indicates that the solution-annealing was not perfectly uniform and that some residual coldworking remained in the corner region. If we assume that the average DPH value of 134 at the midflat corresponds to perfect annealing, then the increased DPH value of about 137 at the corner corresponds to about a 2% increase in coldworking. This estimate is based upon the empirical correlation between DPH values and percent coldworking shown in Fig. 22. Based upon Fig. 32, this 2% increase in coldworking should correspond to an increase of about 5 ksi (34.5 MPa) for the yield stress in the corner.

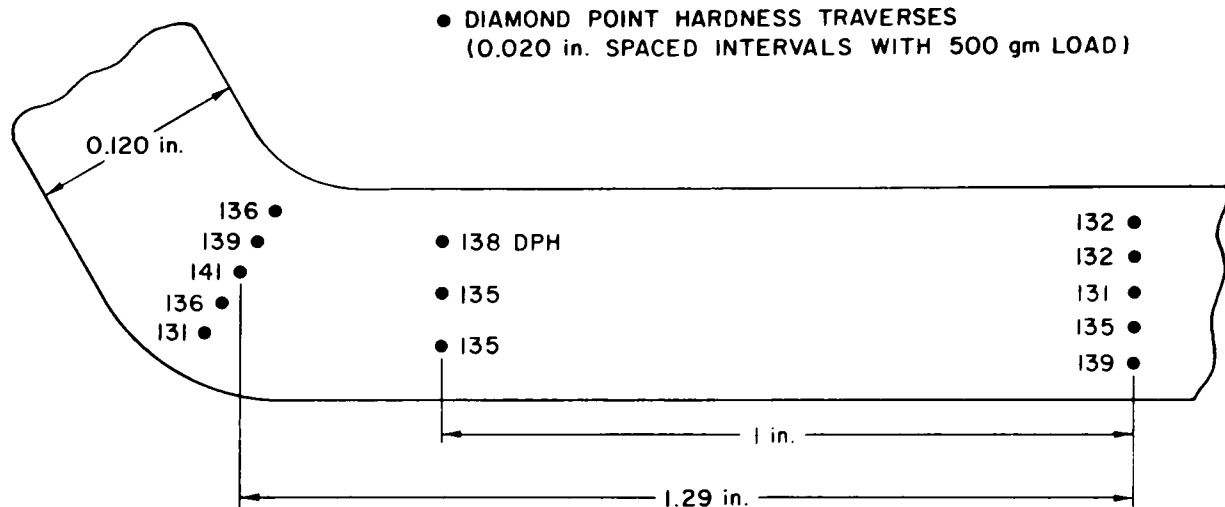


Fig. 31. Diamond-point-hardness Survey over Wall Thickness for Annealed Test Hexcan (1 in. = 2.54 cm)

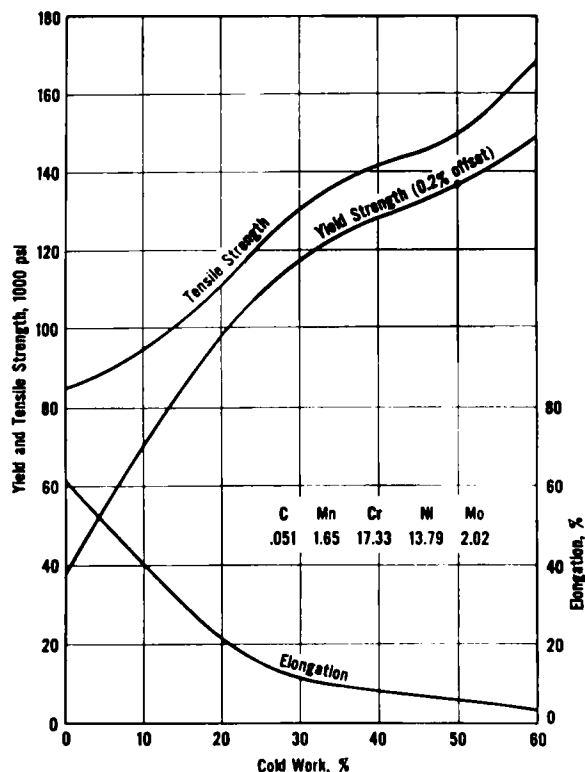


Fig. 32

Effect of Coldworking on Mechanical Properties of Type 316 Stainless Steel (International Nickel Co.) (1 psi = 6.895 kPa).  
ANL Neg. No. 900-4706.

Note in Fig. 31 that not only does the hardness increase along the wall from the midflat to the corner region, but there is also a significant variation

in DPH values across the wall thickness. This variation may indicate that the hardness was influenced by factors other than the simple coldworking as measured by the area reduction from drawing, extrusion, or rolling processes. For example, when the corner is shaped, the outer surface is stretched and the inner surface is compressed, so that differences in hardness through the wall thickness should not be unexpected.

To further illustrate that the yield point is not completely determined by the area-reduction measure of coldworking, reference can be made to some reported tensile tests.<sup>6</sup> The yield stresses of two 50%-coldworked samples were measured. One sample was taken from a duct following the first hexagonal draw. The wall thickness was 0.130 in. (0.33 cm), corresponding approximately to a 50% reduction in cross-sectional area. The other sample was prepared from solution-annealed material cut from a rejected duct that was then rolled down to a 50% reduction in area. Although both samples had 50% coldworking, the yield stress for the sample from the drawing process was 140 ksi (965 MPa), compared to 155 ksi (1069 MPa) for the rolled specimen.

The dependence of the yield stress upon the type of working process may indicate an anisotropy in the tensile properties. It is possible that the yield stress for tension in the longitudinal direction of the duct (i.e., the axial direction) may differ from the yield stress for tension in the transverse, or lateral, duct direction. The tensile-test specimens (those whose results are given in Table IV) were cut so that the tension direction corresponded to the longitudinal direction of the duct. However, the filament layers of the finite-beam elements used in the STRAW code are subjected to tension (and compression) in the transverse direction of the duct so that possible anisotropy may account for some variations in the yield-stress values.

To check the influence of possible anisotropies, an additional tensile-test specimen (8-AN-E, not included in Table IV) was cut from the duct material so that the tension direction corresponded to the lateral, rather than the longitudinal, duct direction. For a crosshead speed of 0.02 in./min (0.008 mm/sec), the yield stress was 28.9 ksi (199 MPa). This result is consistent with the data for the specimens cut in the longitudinal direction and indicates the apparent anisotropic influence.

When the annealed hexcan was pressurized, considerable permanent deformation took place before fracture occurred in the corner region (see Fig. 16). During the expansion of the hexcan, the wall thickness was reduced from 120 to about 95 mils (3.0 to ~2.4 mm), corresponding to an area decrease of about 20% (i.e., 20% coldworking). After the pressurization test, a diamond-point-hardness survey was made for a sample cut from the ruptured hexcan. The results shown in Table V are roughly consistent with the coldworking increase during the pressurization. For comparison, the posttest hardness of the nominal 20%-coldworked test hexcan is also shown in Table V. The permanent diametral flat-to-flat increase was only about 0.3 in. (0.762 cm)

compared to an increase of about 2.81 in. (7.14 cm) for the annealed can. The failure pressure was also much lower, 2300 psi (15.9 MPa) compared to about 4500 psi (31.0 MPa) for the annealed can. For the much smaller deflection the reduction in wall thickness was almost negligible, and little increase in hardness was observed. Hence, we see that the posttest hardness values for the annealed can are comparable to the posttest values for the nominal 20%-coldworked can.

TABLE V. Posttest Microhardness Measurements of Duct

Location on Duct	Average <sup>a</sup> Vickers Microhardness, kg/mm <sup>2</sup>	
	Duct ST-101I	Duct ST-103I
Near fracture	316	328
On flat, 1/2 in. (1.27 cm) from fracture	299	282
On flat, midway between fracture and corner	300	271
On flat, 1/2 in. (1.27 cm) from unfractured corner	297	275

<sup>a</sup>Each value is an average of five indents made with 500-g load.

#### B. The 20%-coldworked Steel with Hardness Gradients

A microhardness examination of a hexcan duct received directly from a vendor indicated that the prescribed nominal 20% coldworking was not uniform throughout the duct. The longitudinal hardness profile shown in Fig. 33 reveals two regions of distinctly different hardness. A sharp change in the DPH values occurred at a transitional texture line extending around the circumference of the duct a short distance from the load pad. A circumferential hardness survey made in the region of greater hardness shows in Fig. 34 a distinct hardness gradient, ranging from 300 DPH units in the midflat region to over 350 in the corner region. Based upon the empirical correlation of Fig. 22, the DPH values indicate a coldworking gradient from a midflat value of about 35% to over 40% in the corner. These coldworking values are considerably higher than might be expected for a prescribed nominal 20%-coldworked duct.

A comparison is made in Fig. 34 with a more expected hardness profile reported by M. Paxton (HEDL, private communication) that corresponds to a variation in coldworking from about 20% over the midflat to 35% in the corner.

This coldworking profile is more consistent with the softer part of the duct, corresponding in Fig. 33 to the right side of the transition line. The nominal 20%-coldworked duct for Test ST-101I, shown in Fig. 16, was cut from this softer part of the duct. Figure 23 shows the circumferential microhardness survey for softer material, from which the test duct was composed; the averaged profile shown in Fig. 24 is more consistent with the HEDL values. The DPH value of 280 at the midflat corresponds to about 23-25% coldworking, and the DPH value of 310 in the corner corresponds to about 30% coldworking.

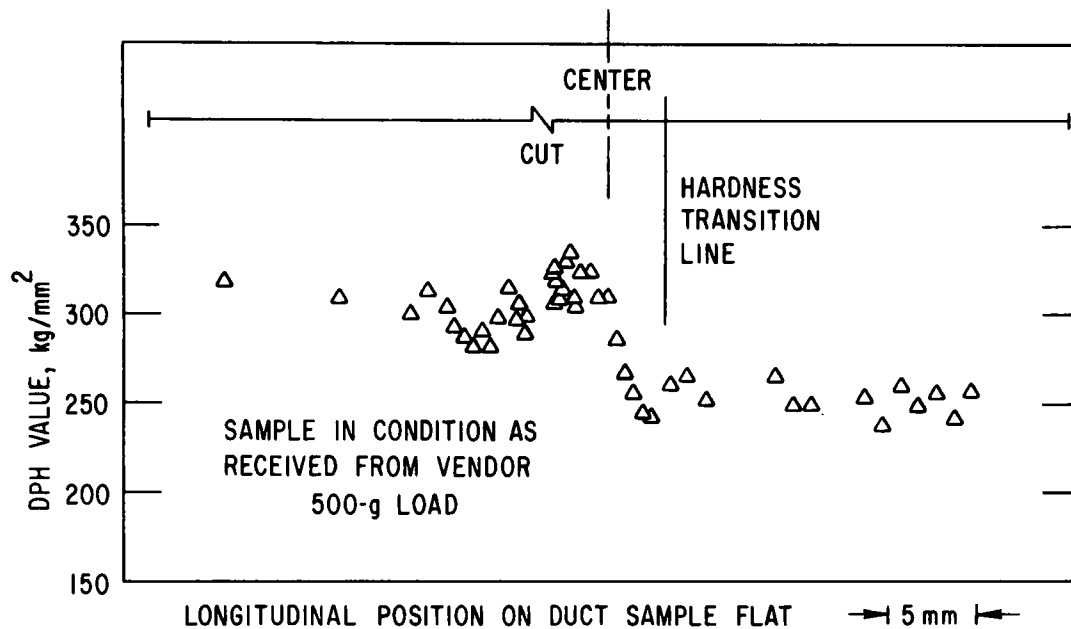


Fig. 33. Hardness Profile Measured along Axial Direction of Nominal 20%-coldworked Duct

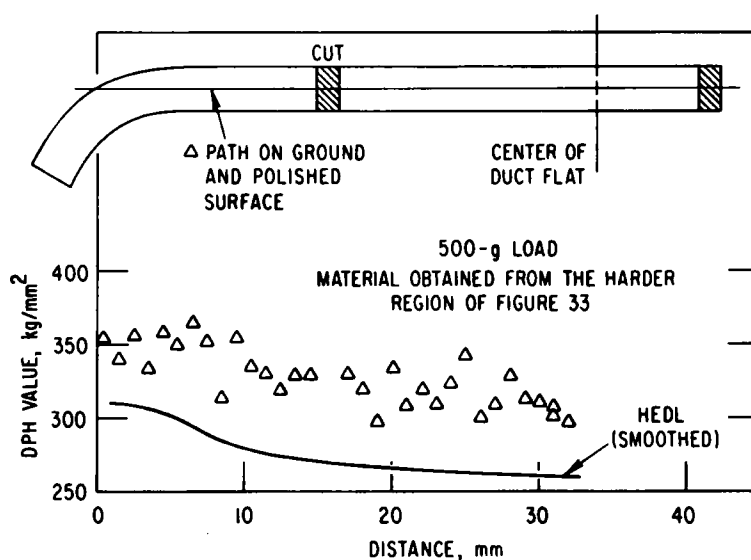


Fig. 34

Hardness Profile Measured from Midflat to Corner for Section from Harder Portion of 20%-coldworked Duct

In addition to the microhardness surveys, samples cut from the test-duct material were subjected to tensile tests. Three sample tensile specimens were cut from alternate flats of the test duct. The tensile axis of each specimen was in the direction of the longitudinal axis of the duct. The results of the tensile test are shown in Table VI. The gage section of the tensile specimen was rectangular with a width-to-thickness ratio of 2/1.

TABLE VI. Tensile-test Results for Nominal  
20%-coldworked Duct Material at 70°F (21°C)

Initial Area, in. <sup>2</sup> (cm <sup>2</sup> )	Crosshead Speed, in./min (mm/sec)	0.2% Offset Yield Stress, ksi (MPa)
0.03105 (0.2003)	0.05 (0.02)	115.3 (795.0)
0.03010 (0.1942)	0.05 (0.02)	116.3 (801.9)
0.03081 (0.1988)	1.00 (0.42)	115.3 (795.0)

The crosshead displacements recorded on a strip chart of load versus extension included the extensions of the pull rods as well as the total extension of the tensile specimen. Since the strip chart is not considered to provide a reliable measure of the strains, the yield strain is not included in Table VI. For the later tensile tests of the annealed and the 50%-coldworked steel, an extensometer was attached directly to the gage section of the specimen. The 0.2% offset yield stress of about 115 ksi (793 MPa) corresponds to a coldworking of about 25% in the empirical graph shown in Fig. 32. This is consistent with the coldworking value of the test duct as indicated by the measured microhardness of 280 DPH units (see Fig. 24), which corresponds in Fig. 22 to a coldworking of about 25%.

#### C. The 50%-coldworked Type 316 Stainless Steel

The tensile-test specimens for the 50%-coldworked test ducts were cut as previously described for the annealed tensile specimens. The tensile properties of four different duct test sections were measured. Sample specimens were cut from alternate flats for each of the test ducts, so that a total of 12 tensile tests were run. The results of these tensile tests are listed in Table VII. Microhardness surveys were also made for additional samples taken from the remaining flats; the distribution of DPH values for a typical sample is shown in Fig. 35. The hardness is reasonably uniform, with no apparent increased hardness in the corner region, as existed for the nominal 20%-coldworked duct.

A representative average DPH value of 332 for the samples corresponds to a coldworking of about 40%. (See Fig. 22 for the correlation of DPH values and coldworking.) In accordance with Fig. 32, the corresponding 0.2% offset yield stress is about 130 ksi (896 MPa). This yield stress is consistent with the measured tensile-test values listed in Table VII. We may infer, on the basis of Fig. 32, that the actual coldworking value is closer to 40% rather than the nominal value of 50% as specified by the area reduction. A representative graph of uniaxial tensile load (per unit initial gage section area) versus extension per unit gage length is plotted in Fig. 36 for one of the tensile-test specimens. It should be emphasized that, beyond the ultimate point, the graph is nonunique and depends upon the tensile-specimen dimensions.

TABLE VII. Tensile-test Results for 50%-coldworked  
Duct Material at 70°F (21°C)<sup>a</sup>

Sample	Initial Area, in. <sup>2</sup> (cm <sup>2</sup> )	Crosshead Speed, in./min (mm/sec)	0.2% Yield Stress, ksi (MPa)	Ultimate Strength, ksi (MPa)	Maximum Uniform Strain, %	Final Load, lb (kg)	A <sub>neck</sub> , <sup>b</sup> in. <sup>2</sup> (cm <sup>2</sup> )
1-50-B	0.02971 (0.19168)	0.02 (0.01)	134.3 (926.0)	139.5 (961.8)	3.4	2825 (1281)	0.0140 (0.0903)
1-50-D	0.03097 (0.19981)	0.02 (0.01)	131.6 (907.4)	138.2 (952.9)	4.2	2920 (1325)	0.0134 (0.0865)
1-50-F	0.03001 (0.19361)	0.02 (0.01)	132.0 (910.1)	138.5 (954.9)	5.2	2920 (1325)	0.0140 (0.0903)
2-50-B	0.03034 (0.19574)	0.02 (0.01)	131.8 (908.7)	138.1 (952.2)	3.9	3450 (1565)	0.0164 (0.1058) <sup>c</sup>
2-50-D	0.03018 (0.19471)	0.02 (0.01)	133.4 (919.8)	138.8 (957.0)	4.5	2820 (1279)	0.0131 (0.0845)
2-50-F	0.03064 (0.19768)	1.0 (0.42)	134.5 (927.3)	141.2 (973.5)	4.8	2900 (1315)	0.0149 (0.0961)
3-50-B	0.03067 (0.19787)	0.02 (0.01)	135.0 (930.8)	140.9 (971.5)	4.1	2900 (1315)	0.0142 (0.0916)
3-50-D	0.03046 (0.19652)	0.02 (0.01)	136.9 (943.9)	141.7 (977.0)	4.2	3090 (1402)	0.0146 (0.0942)
3-50-F	0.02952 (0.19045)	0.02 (0.01)	138.9 (957.7)	146.5 (1010.1)	4.6	2980 (1352)	0.0140 (0.0903)
4-50-F	0.03063 (0.19761)	0.02 (0.01)	137.4 (947.3)	141.4 (974.9)	4.1	2940 (1334)	0.0138 (0.0890)

<sup>a</sup>Engineering values for samples of rectangular gage section, 0.12 x 0.25 in. (0.30 x 0.64 cm) and 1-in. (2.54 cm) original gage length.

<sup>b</sup>Posttest cross-sectional area at failure site. These cross sections were of concave rectangular shape. Maximum and minimum dimensions were measured with a 0.03-in. (0.0762-cm)-thick blade micrometer to calculate average area.

<sup>c</sup>Test stopped before specimen failure.

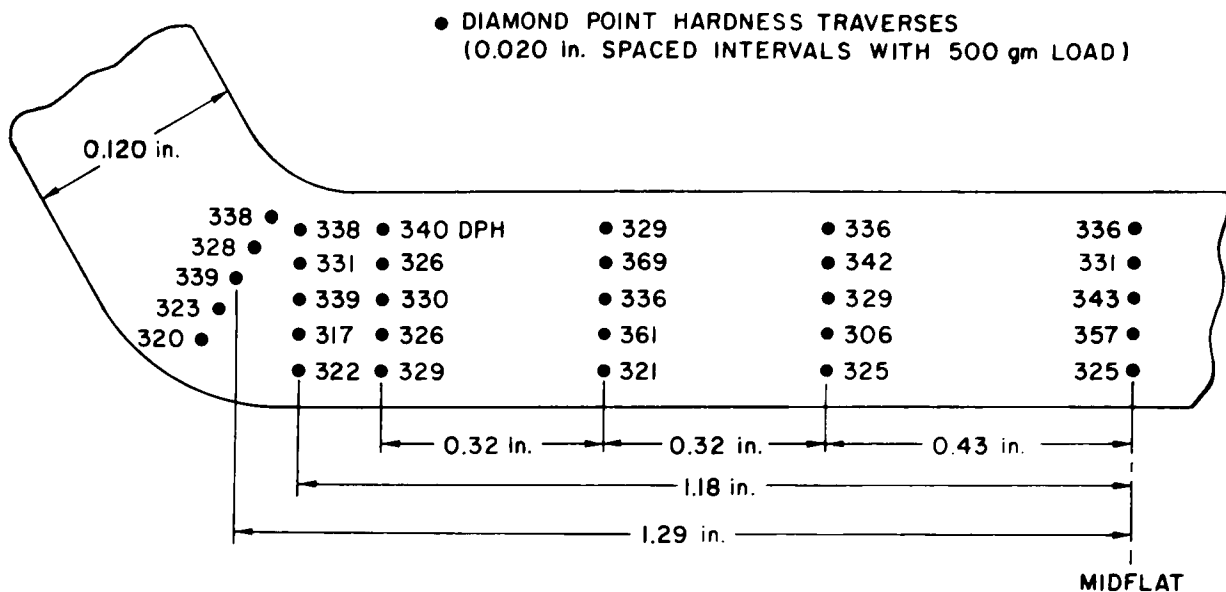
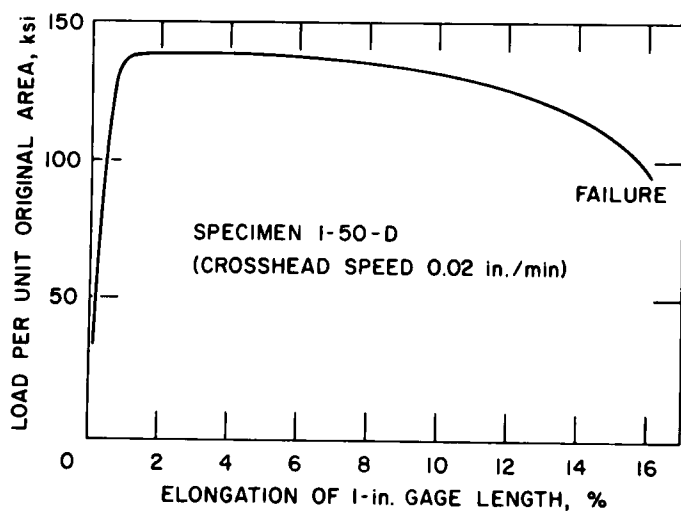


Fig. 35. Diamond-point-hardness Survey over Wall Thickness for 50%-coldworked Test Hexcan (1 in. = 2.54 cm)



**Fig. 36**

**Tensile-test Data of Elongation vs Unit Load for  
50%-coldworked Hexcan Tensile Specimen  
(1-50-D) with Crosshead Speed of 0.02 in./min  
(1 ksi = 6.895 MPa; 1 in./min = 0.423 mm/sec)**



## V. COMPARISONS OF CALCULATIONS WITH EXPERIMENTS

Room-temperature experiments were performed to study the deformation of Type 316 stainless steel test hexcan sections under internal and external hydrostatic pressure loadings. The tests were conducted at Stanford Research Institute as part of an effort to obtain data on the gross mechanical response of LMFBR-type hexcans. The main objective of the tests was to provide reliable data for the verification of analytical computer codes being developed to predict the response of hexagonal-subassembly wrappers to local accidental events.

The sample test ducts are nominally 20% coldworked when received directly from the manufacturer; additional residual coldworking exists in the corner regions ranging up to 35%. Hydrostatic tests were run with these as-received, nominal 20%-coldworked ducts; to determine the influences of material properties upon the hexcan response, additional tests were run for hexcans with changed material properties. The as-received hexcan was solution-annealed to increase the ductility of the steel. The yield stress was lowered to about one-third that of the 20%-coldworked material.

An advantage of the annealing process was to provide a hexcan with a uniform hardness throughout, thus eliminating the computational difficulties associated with the presence of coldworking gradients. To extend the range of material properties, special low-ductility test hexcans with a higher yield stress were fabricated with a specified final area reduction corresponding to 50% coldworking. The experimental results are described below for the three sets of hydrostatic tests: (1) the uniform annealed, (2) the nominal 20% coldworked with hardness gradients, and (3) the 50%-coldworked hexcans. Comparisons are made with computer-code calculations.

The test rig used for the hydrostatic experiments is shown in Figs. 1 and 2. Deflections and strains were measured over a central gage section of the test hexcan midway between the ends. This gage section was sufficiently remote from the ends to avoid end effects. It was demonstrated by computations, and corroborated by experiments, that a hexcan length of 1 ft (30.48 cm) was adequate to prevent end effects from reaching the central gage section. The ends were constrained against axial displacements by twelve 1-in. (2.54-cm)-dia bolts that locked the 2-in. (5.08-cm)-thick end plates in place. This constraint imposed plane-strain deformations upon the gage section. Strain gages were located at the midflats and corners; displacements at these locations were measured with dial gages and linear potentiometers. Tests were conducted for hexcans pressurized internally and also externally. A manually operated hydraulic pump was used for the pressurization.

## A. Hydrostatic Tests with Annealed Hexcan

### 1. Internal-pressurization Tests

Comparisons have been made between calculations and the experimental results of hydrostatic internal-pressurization tests (performed at room temperature) of solution-annealed Type 316 stainless steel hexcans. The overall objective of the tests was to provide reliable data on hexcan deformation using a material having uniform properties without the hardness gradients present in the as-received, nominal 20%-coldworked ducts.

Because of the significant increase in ductility produced by the annealing, large deformations can be achieved before fracture occurs, so that the range of allowable strains can be determined for which the application of the STRAW code will be valid. Because of the use of convected coordinates, the code permits large deflections, but is restricted in the magnitude of permissible relative strains because second-order and higher strain terms are neglected in the numerical-approximation procedure.

The material properties of the annealed Type 316 stainless steel were determined by tensile tests of samples taken directly from the hexcans. In the step-by-step computation of the hexcan deflection, the response of each finite element to the applied pressure and the internal stress forces is calculated. The stress is determined from the stress-strain relationship, and the resulting force is the product of the stress and the true area. This area is not the original unstrained area, but diminishes as the wall thickness decreases with the hexcan expansion. Consequently, the true stress, rather than the engineering stress, is used in the force-balance equations.

The graph of the true stress, which is provided as input to the STRAW code, is shown in Fig. 37 as a function of the engineering strain. For

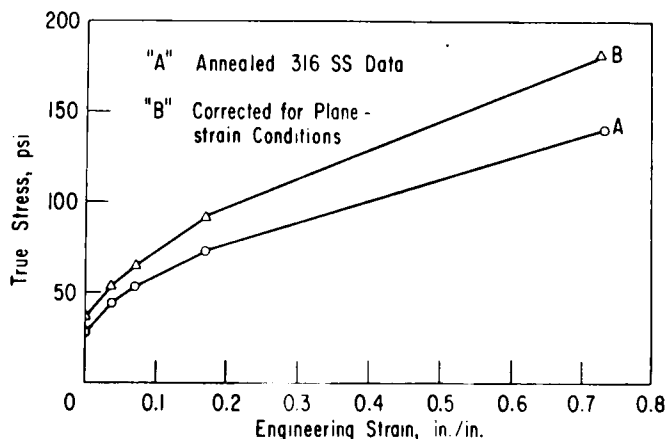


Fig. 37. Room-temperature Tensile-test Stress-Strain Data for Annealed Type 316 Stainless Steel Corrected for Plane-strain Conditions (1 psi = 6.895 kPa; 1 in. = 2.54 cm). ANL Neg. No. 900-75-220.

each finite flexural-beam element, the strain varies over the thickness of the beam as a function of the distance  $y$  from the neutral axis. At each distance  $y$ , the strain corresponds to the engineering strain of a longitudinal fiber extending the length of the element. The engineering strain is the elongated (or compressed) length of the fiber divided by the original unstrained length. Curve A in Fig. 37 is the relationship between uniaxial true stress and engineering strain, derived directly from the tensile-test specimen.

Since the deformation of the hexcan test section is assumed to

deform in a plane-strain mode, rather than under uniaxial stress conditions, the tensile-test data must be modified (see Appendix B). The modification consists essentially of a point-by-point increase in the graph slope by a factor of  $4/3$ . Curve A is thus shifted and raised to the curve B shown in Fig. 37. These modified data, represented by curve B, provide input to a STRAW subroutine from which a stress is determined corresponding to a previously computed engineering strain. The subroutine has the capability to correct the stress for strain-rate effects and also, when a strain reversal occurs, to modify the yield-stress point for changes due to strain-hardening effects. Strain reversals take place at the outer surface of the corners and at the inner midflat surface, as shown in Fig. 19.

Under internal pressurization, the corner outer surface first undergoes compression due to the bending deformation mode of the flat as it deflects outward. With increasing pressurization, a point is reached at which a hexcan-expansion deformation mode dominates, and the plastically compressed material at the outer corner surface will unload along a new elastic line. Under increased pressurization, the outer surface will strain under elastic tension, until eventually a tensile yield-stress point is reached. The value of the new yield-stress point depends upon the choice of hardening model. The extremes are the kinematic and isotropic hardening models.

An example of the two hardening models is shown in Fig. 38. The kinematic model assumes no strain-hardening influence in that the magnitude of the elastic range is unchanged.

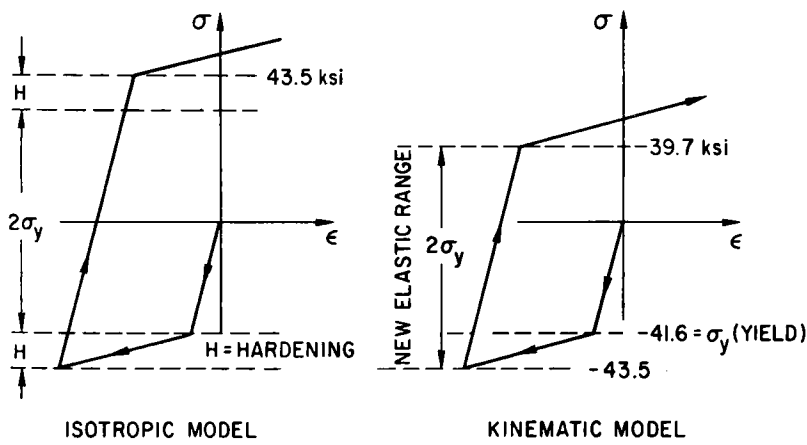


Fig. 38. Influence of Assumed Hardening Model upon New Yield Point (1 ksi = 6.895 MPa).  
ANL Neg. No. 900-4646 Rev. 1.

The isotropic model assumes that both the tensile and compressive parts of the elastic range are each increased by an amount equal to the work hardening. As a result, the total elastic range is increased by twice the work hardening.

An intermediate model is that of "fixed" hardening, for which the new tensile yield stress is equal to the original value. In this latter case, the new elastic range is increased by a stress

increment equal to the work hardening induced during the plastic-flow strain hardening. Based upon the recommendation suggested by Mendelson,<sup>9</sup> the strain-hardening model used in the STRAW computations assumed a yield point midway between the fixed and kinematic models, i.e., a yield-stress increment amounting to one-half the work hardening.

The initial internal-pressurization tests performed with the annealed hexcans demonstrated that a 1-ft (30.48-cm)-long test length of a duct

is sufficient to provide a centrally located gage section free from end effects. The absence of end effects was demonstrated by showing that the gage-section deflections were independent of axial length for hexcans 1 ft (30.48 cm) long or greater. Hydrostatic tests were run for 1- and 2-ft (30.48- and 60.96-cm)-long hexcans; the measured midflat deflections are compared in Fig. 6. The corner deflections are compared in Fig. 7. Since the measured deflections for the two tests show no significant disagreement, we may conclude that end effects were negligible over the complete pressure range up to 2800 psi. The annealed hexcan had the greatest range of deformations in comparison to the 20%- and 50%-coldworked hexcans. It may therefore be safely assumed that a 1-ft (30.48-cm)-long test section is adequate also for the tests on these less ductile hexcans.

Figures 39-41 compare computed and experimental data for midflat and corner deflections, and strains at the outer midflat surface, measured

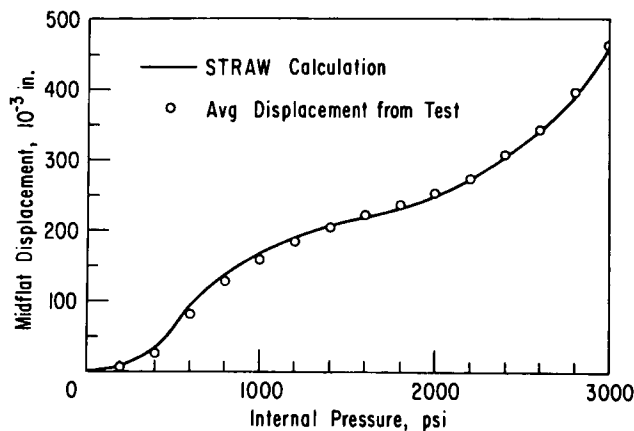


Fig. 39

Comparison of Experimental and Calculated Midflat Displacements for Annealed Type 316 Stainless Steel Internally Pressurized Hexcan (1 in. = 2.54 cm; 1 psi = 6.895 kPa). ANL Neg. No. 900-5792.

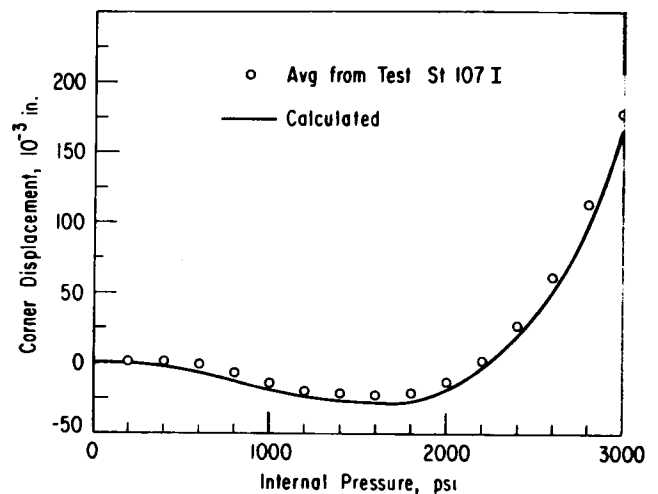


Fig. 40

Comparison of Experimental and Calculated Corner Displacements for Annealed Type 316 Stainless Steel Internally Pressurized Hexcan (1 in. = 2.54 cm; 1 psi = 6.895 kPa). ANL Neg. No. 900-75-213.

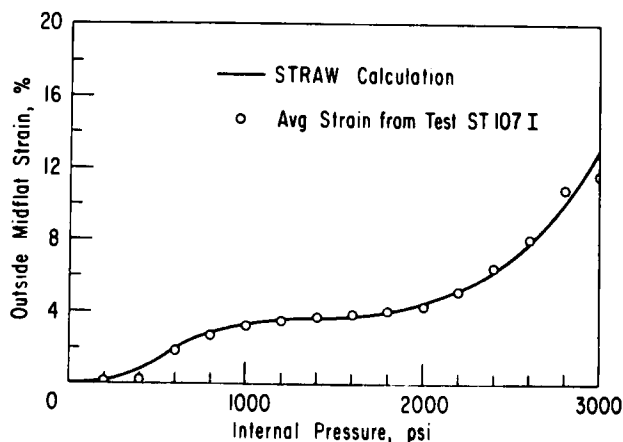


Fig. 41

Comparison of Experimental and Calculated Outer Midflat Strains for Annealed Type 316 Stainless Steel Internally Pressurized Hexcan (1 psi = 6.895 kPa). ANL Neg. No. 900-5793.

over the gage section of an annealed hexcan under internal pressurizations up to 3000 psi (20.7 MPa). The experimental data are from the Stanford Research Institute test labeled ST-107I, which had strain gages and linear potentiometers positioned on each flat and corner. The correlation with the STRAW computations is nearly perfect. Each data point shown in the figures is the average for the six sides of the hexcan.

Two other tests labeled ST-103I and -104I for 1- and 2-ft (30.48- and 60.96-cm)-long test hexcans yielded data very nearly the same as shown in Figs. 39-41. The corner deflections appeared to deviate from the computed values to a slightly greater degree than the deviations from the computed midflat deflections. The greater percentage deviation is to be expected because of the much smaller magnitude of the corner deflections, and the expanded ordinate axis magnifies the appearance of the deviation. Actually, each of the six corners did not deflect by the same amount; the scatter between the individual corner deflections was comparable to the deviation between the computed and the average experimental values.

## 2. External-pressurization Tests

Consideration of the possibility of failure propagation from an accident subassembly to the neighboring core regions requires an analysis of the mechanical response of the neighboring subassemblies. The hexcan wrappers of the adjacent subassemblies will be subjected to external pressure loads originating from the accident subassembly. In anticipation of performing future hexcan-cluster tests to simulate the mechanics of subassembly-to-subassembly propagation, some initial tests were performed in which an annealed Type 316 stainless steel hexcan was hydrostatically loaded from the outside. The deformed equilibrium configuration of an externally loaded hexcan does not possess the stability that an internally pressurized hexcan has and is consequently subject to asymmetric collapse, or buckling, modes. Initiation of this buckling phenomenon could originate either from irregularities in the hexcan geometry, or from irregularities or nonuniformities in material properties that may result in one corner yielding before any of the others.

Figure 42 shows possible modes of collapse. The first possibility is a symmetric response characterized by pure bending of the hexcan flats, as shown in Fig. 42a. A sample STRAW-code calculation of this mode of collapse is shown in Fig. 43. Another possibility is a "pantograph-type" collapse, or some variation of this mode, due to geometrical or material irregularities, as shown in Fig. 42b. On the basis of the experiments, the most likely shape to be assumed by an externally pressurized hexcan is a combination of the above two modes, as shown in Fig. 42c.

For the annealed Type 316 stainless steel hexcan in Test ST-105E, a collapse mode began at an external pressurization between 400 and 500 psi (2.76 and 3.45 MPa). Further pressurization beyond the initiation point of the

collapse instability resulted in relatively large deformations for only slight increases in pressure. The final outside shape of the hexcan cross section at an external pressure of 600 psi is shown in Fig. 44 compared with the initial undeformed hexagonal shape. In Fig. 44 we see a combination of plastic bending of the flats, together with the pantograph collapse mode as indicated by the significantly greater diagonal distance of 4.9 in. (12.446 cm) from corner F/A to C/D, compared to the distance of 4.5 in. (11.43 cm) from corner E/F to B/C. The longer diagonal from corner F/A to C/D appears to define a symmetry plane, behaving somewhat as if these corners were hinged. It is obvious that the projected area over which the uniform external pressure acts is greatest along this longer diagonal; consequently, the greatest crushing force will tend to flatten the hexcan into this symmetry plane.

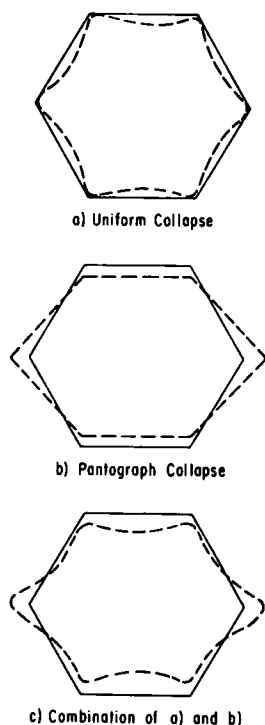


Fig. 42

Unstable Collapse Modes  
for Externally Loaded  
Hexcan. ANL Neg.  
No. 900-75-211.

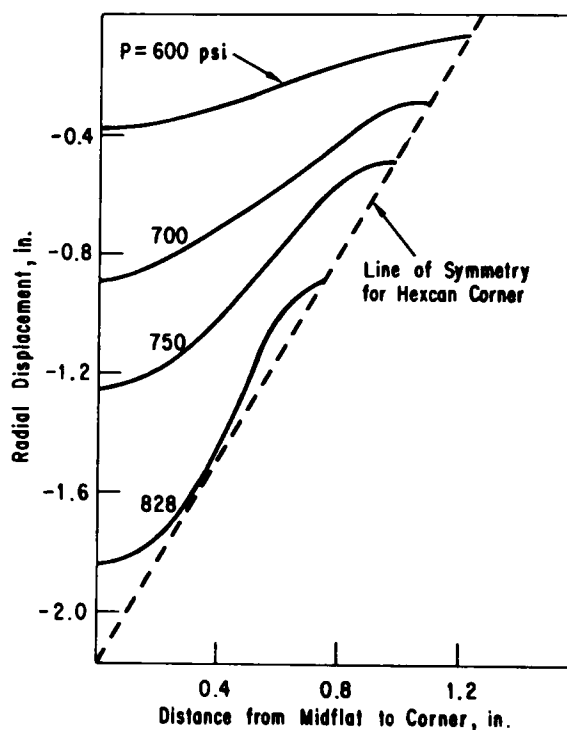


Fig. 43

Sample STRAW-code Calculation of  
Unstable Collapse Mode for Externally  
Loaded Hexcan (1 in. = 2.54 cm).  
ANL Neg. No. 900-4598.

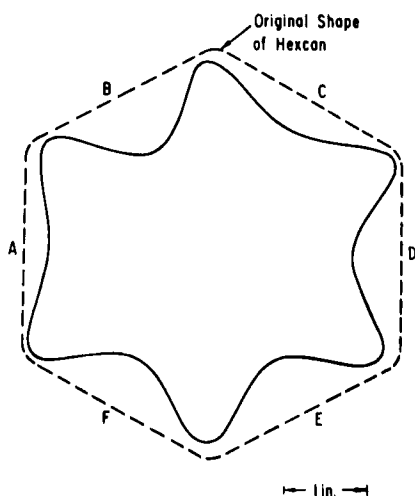


Fig. 44

Final Shape of Externally Pressurized  
Annealed Hexcan (1 in. = 2.54 cm).  
ANL Neg. No. 900-75-209.

STRAW-code calculations for deflections and strains are compared with experimental measurements in Figs. 45-47. Figure 45 compares the calculated and experimentally determined midflat deflections. The calculation, although qualitatively resembling the shape of the experimentally determined curve, is underpredicting the deformation significantly. This behavior is more pronounced when the calculated and experimentally determined deflections at the corner are compared in Fig. 46. Here a strong discrepancy is revealed which can be explained by the asymmetric collapse of the hexcan. Apparently the hexcan is collapsing in a mode in which flat A is essentially rotating around corner A/F. The measured strains plotted in Fig. 47 tend to confirm this supposition.

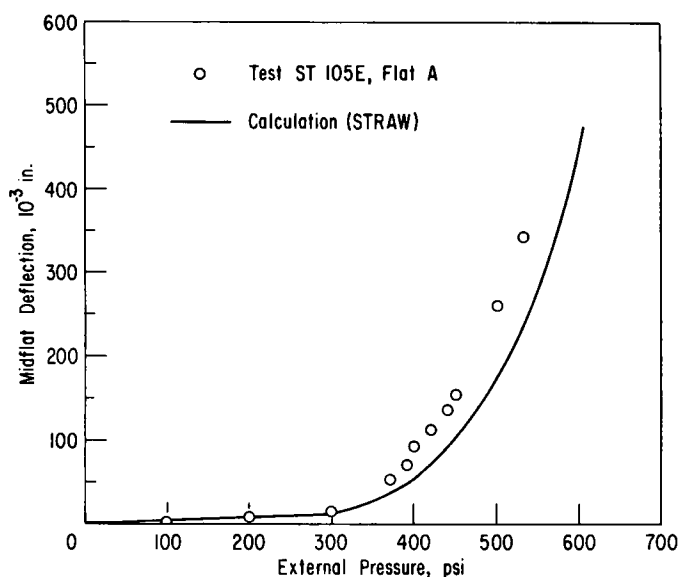


Fig. 45. Comparison of Experimental and Calculated Midflat Displacements for Annealed Type 316 Stainless Steel Externally Pressurized Hexcan (1 in. = 2.54 cm; 1 psi = 6.895 kPa). ANL Neg. No. 900-75-208.

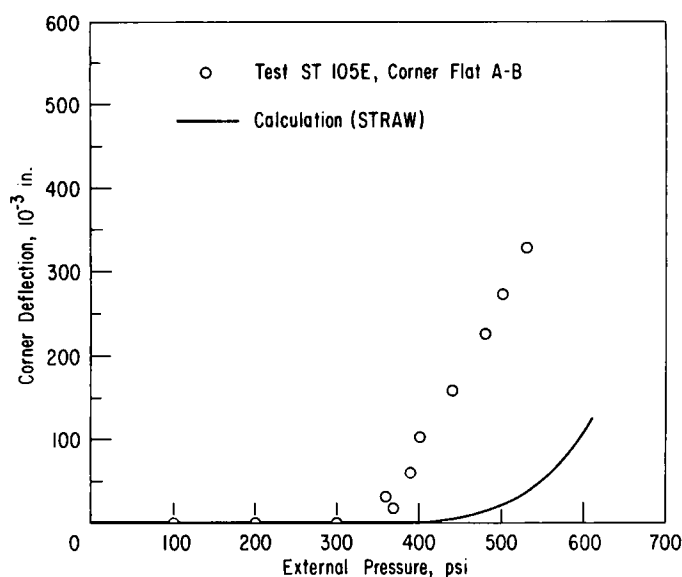


Fig. 46. Comparison of Experimental and Calculated Corner Displacements for Annealed Type 316 Stainless Steel Externally Pressurized Hexcan (1 in. = 2.54 cm; 1 psi = 6.895 kPa). ANL Neg. No. 900-75-207.

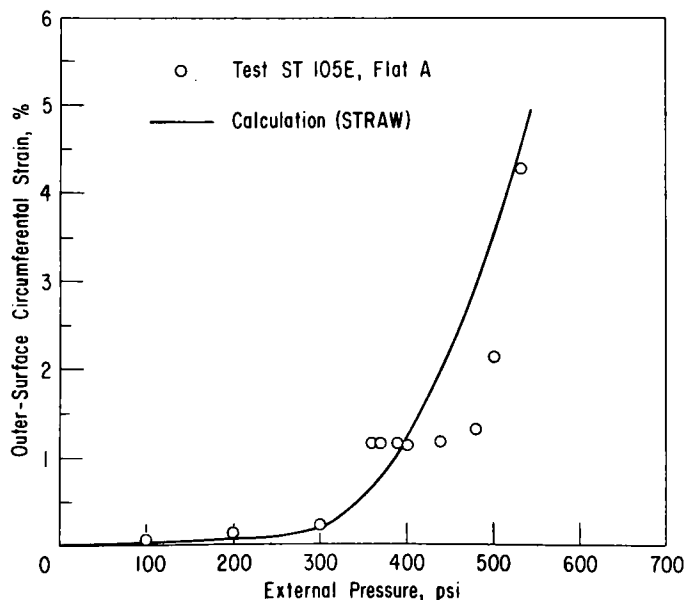


Fig. 47

Comparison of Experimental and Calculated Outer Midflat Strains for Annealed Type 316 Stainless Steel Externally Pressurized Hexcan (1 psi = 6.895 kPa). ANL Neg. No. 900-75-210.

The measured strains at flat A are consistent with the calculated strains (based upon assumed symmetry) out to a pressure of about 300 psi (2.07 MPa). However, at pressures between 350 and 400 psi (2.41 and 2.76 MPa), the measured strains do not change, indicating that flat A is essentially undergoing a rigid-body rotation, and the lack of correlation with the computed deflections indicates that the symmetry assumption is no longer maintained. Apparently, flat A initially deformed as a beam out to a pressure of 300 psi (2.07 MPa). Increasing the pressure initiated the pantograph collapse mode, at which point corner A/F began to behave as a plastic hinge about which flat A rotates.

To support the hypothesis that rotation of the flat was occurring about a plastic-hinge corner, a simplified model was assumed in which further

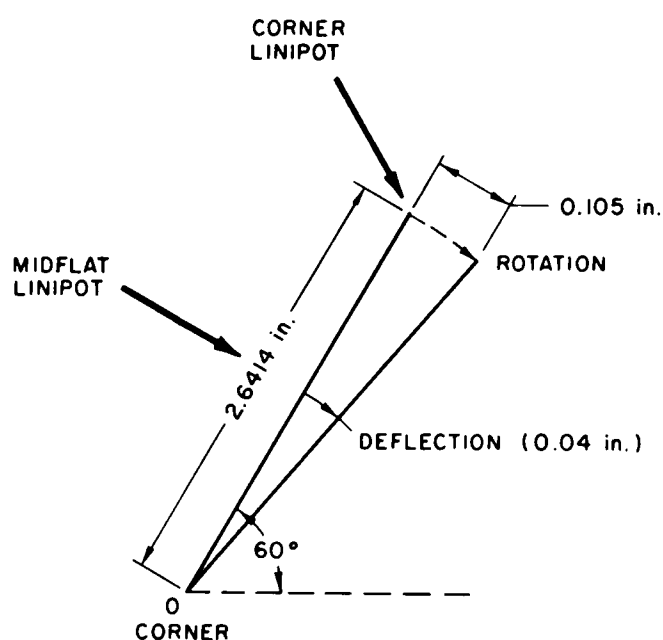


Fig. 48. Simplified Pantograph Model to Estimate Midflat Deflection Component due to Plastic-hinge Rotation at Corner (1 in. = 2.54 cm)

bending of the flat was delayed. The model is shown in Fig. 48, and the flat is assumed to rotate about point O. For the geometry shown, the midflat displacement corresponding to rotation is 0.04 in. (1.016 cm), which should be added to the calculated deflection for the symmetric bending. Referring to Fig. 45, we see that adding 40 mils (1.016 mm) to the computed deflection gives a total deflection consistent with the measured deflection.

The type of instability described above for externally loaded hexcans is not likely to occur for operational reactors, because the fuel pins inside the subassembly will inhibit asymmetric collapse modes. Also, the external loading will most likely be caused by a pressure pulse

dynamically loading one side of the duct, rather than a hydrostatic pressure uniform about the duct circumference.

## B. The Nominal 20%-coldworked Hydrostatic Tests

The annealed and the 50%-coldworked test-hexcan materials were specially processed at Argonne National Laboratory to ensure reasonably uniform material properties before shipment to Stanford Research Institute for the pressurization tests. Detailed microhardness surveys were performed, and a number of tensile specimens were cut from the ducts to determine the stress-strain relationships. The material properties of the nominal 20%-coldworked test hexcans, were not as carefully determined and controlled. These test hexcans were cut directly from the ducts as received from the



vendor. No attempt was made to modify the hardness properties, which were nonuniform and not exactly 20% coldworked. When pressurized out to failure, the final deformation of the 20%-coldworked hexcan was significantly less than that for the annealed hexcan, as shown in the comparison of Fig. 16. The much lower ductility corresponds to the greater hardness of the coldworked material.

A microhardness survey made of the duct material before Test ST-101T is shown in Fig. 23. The profile plotted in Fig. 24 of the averaged microhardness values shows the variation from midflat to corner. Comparing these DPH values with the values measured after the test, listed in Table V, we see that the relatively small deformations incurred during the hexcan pressurization out to failure did not result in any significant additional work hardening of the material. By contrast, we see in Table V that the annealed hexcan underwent significant work hardening during pressurization, so that the final coldworking state was comparable to that of the nominal 20%-coldworked test hexcan. The hardness variation from 280 at the midflat to 310 DPH units in the corner corresponds, according to the empirical correlation shown in Fig. 22, to a coldworking from 23 to 26% over the midflat, and from 30 to 34% in the corner region.

Because of the nonuniformity of the coldworking, the deflection computations are not considered to be as reliable as for the more clearly defined material properties of the annealed and 50%-coldworked test hexcans. For the nominal 20%-coldworked hexcan, several sets of computations were made for a range of assumed material properties. The computed deflections are compared with experimental measurements in Fig. 49 and with the midflat outer-surface strains in Fig. 50. The graph labeled "ANL Material Properties"

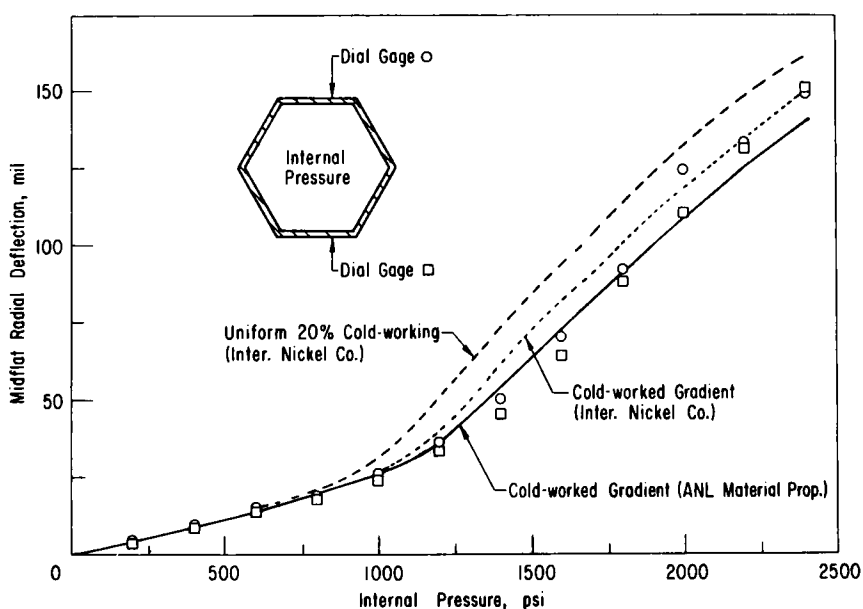


Fig. 49. Comparison of Experimental and Calculated Midflat Displacements for Nominal 20%-coldworked Type 316 Stainless Steel Internally Pressurized Hexcan (1 mil = 0.0254 mm; 1 psi = 6.895 kPa)

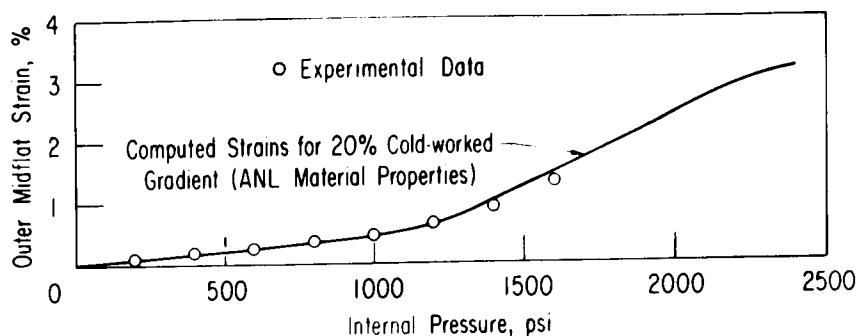


Fig. 50. Comparison of Measured Strains at Midflat of Outer Surface with Computed Strains (1 psi = 6.895 kPa)

correlates best with the test data and represents the STRAW computation for the material properties corresponding to the measured microhardness profile shown in Fig. 24. The graph labeled "Inter. Nickel Co." is based upon the Type 316 stainless steel properties shown in Fig. 32 as a function of coldworking. The coldworking gradient was assumed to vary from 20% over the midflat region to 33% in the corner. Since these coldworking values are lower than those indicated by the measured microhardness profile, the assumed yield stress will be somewhat low and the corresponding computed deflections will be high. For example, at 1800 psi (12.4 MPa) this lowered yield stress value results in a 10% increase in the deflection, from about 90 to 100 mils (2.29 to 2.54 mm).

To study the effect of corner hardness upon the deflection, the graph shown in Fig. 49 was computed for a uniform 20% coldworking with no hardness gradients. Removing the increased hardness in the corner raises the midflat deflection by about 14% at 1800 psi (12.4 MPa), from 100 to 114 mils (2.54 to 2.90 mm). By comparison, the effect upon the midflat deflection for grossly lowering the yield stress by annealing the steel is shown in Fig. 9. The midflat deflection of the 20%-coldworked hexcan was about one-half the deflection of the annealed hexcan at a pressure of 2410 psi (16.6 MPa) (the failure pressure for the coldworked hexcan); the deflection was reduced from about 300 to 150 mils (7.62 to 3.81 mm).

The rigidity of the 20%-coldworked hexcan is demonstrated in Fig. 10 by the negligible deflection of the corner under the increasing pressurization out to failure. A further comparison with the annealed hexcan is made in Fig. 11, which shows that the midflat strain at the outer surface has been reduced by a factor of about 6. The limiting strain for the strain gage was about 3%; the gage failed when this point was exceeded at about 900 psi (6.2 MPa) for the annealed hexcan.

### C. The 50%-coldworked Hydrostatic Tests

#### 1. Internal-pressurization Tests

The 50%-coldworked steel is considerably less ductile than the annealed steel and more nearly approximates the hexcan under prototypic

operating conditions. Compared with the annealed hexcan, the 50%-coldworked steel hexcan deformed much less at corresponding pressures. Under a pressurization of 3000 psi (20.7 MPa), the midflat deflection was only 140 mils (3.56 mm) compared with 465 mils (11.81 mm) for the annealed hexcan. The purpose of the annealed-hexcan experiments was to check the range of applicability of the STRAW code. The STRAW code is based upon the equations for small strains (i.e., second-order strain terms are dropped) while permitting large deflections. The more ductile annealed hexcan underwent a wide range of strains before fracture occurred along one corner. Good correlations between computations and test data were maintained up to midflat strains in excess of 14%. For the more brittle 50%-coldworked steel, the strains were much less; hence, we can conclude that the 50%-coldworked hexcan tests are well within the STRAW-code capability.

The material properties shown in Fig. 51 are based upon tensile tests for seven sample specimens. The median graph for the seven tests is shown in Fig. 51 together with the graph modified for plane-strain conditions. The upper range of the stress values extends about 10% above the median. The computed values for the midflat deflection shown in Fig. 52 are somewhat greater than the experimental values. A nearly perfect correlation is obtained if the steel is assumed to be 10% stiffer, corresponding to the upper range of the spread in the tensile-test material-property data.

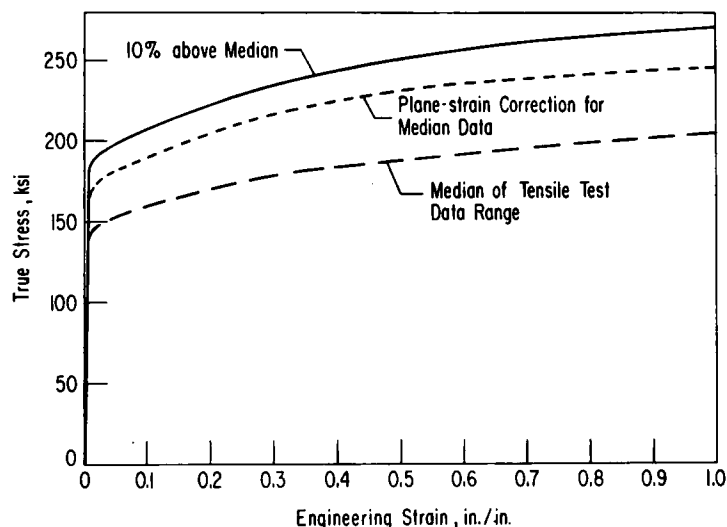
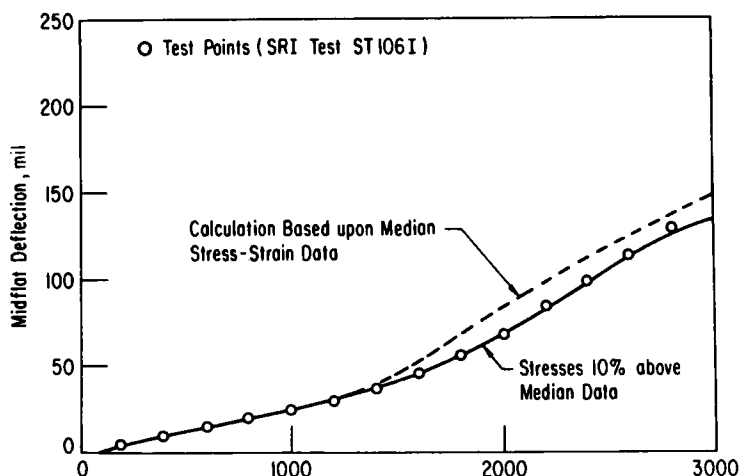


Fig. 51

Room-temperature Tensile-test Stress-Strain Data for 50%-coldworked Type 316 Stainless Steel Corrected for Plane-strain Conditions (1 ksi = 6.895 MPa; 1 in. = 2.54 cm). ANL Neg. No. 900-75-219.

Fig. 52

Comparison of Experimental and Computed Midflat Deflections for 50%-coldworked Type 316 Stainless Steel Internally Pressurized Hexcan (1 mil = 0.0254 mm; 1 psi = 6.895 kPa). ANL Neg. No. 900-75-215.



The deflection magnitudes for the corners are so small that a precise correlation cannot be expected because the limit of accuracy of the deflection measurements is approached.

However, the trend of the computed corner deflections shown in Fig. 53 follows the experimental data. The percent difference between the measured and computed corner deflections is relatively great, but the actual magnitude of the discrepancy is small. The computed deflection differs from the experimental at 3000 psi (20.7 MPa) by only a few mils.

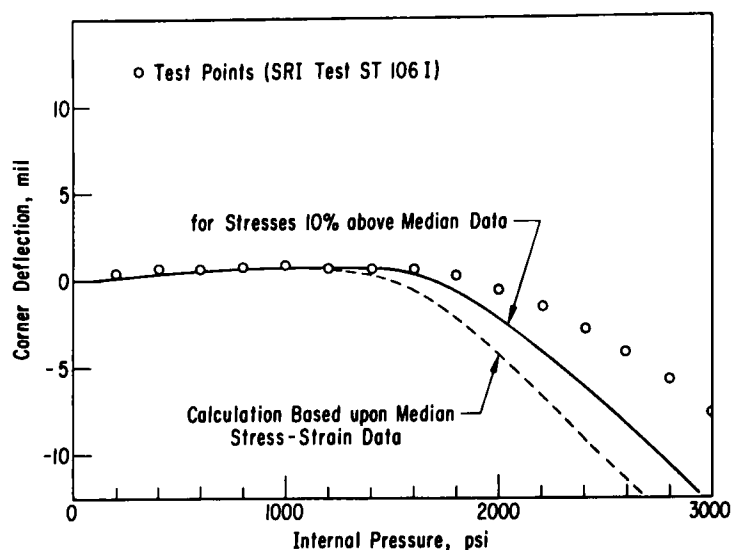


Fig. 53. Comparison of Experimental and Computed Corner Deflections for 50%-coldworked Type 316 Stainless Steel Internally Pressurized Hexcan (1 mil = 0.0254 mm; 1 psi = 6.895 kPa). ANL Neg. No. 900-75-222.

The computed strains at the outer and inner surfaces of the midflat region shown in Figs. 54 and 55 correlate well with the measured strains. When the stress-strain graph is raised 10% above the median data, the correlation becomes nearly perfect. The strains

at the outer surface are in tension, as expected; the lower surface strains are in compression. The maximum compressive strain at the lower surface was about -1.3%. If continued straining were possible under further expansion without the occurrence of fracture at the corner, the strain at the lower midflat

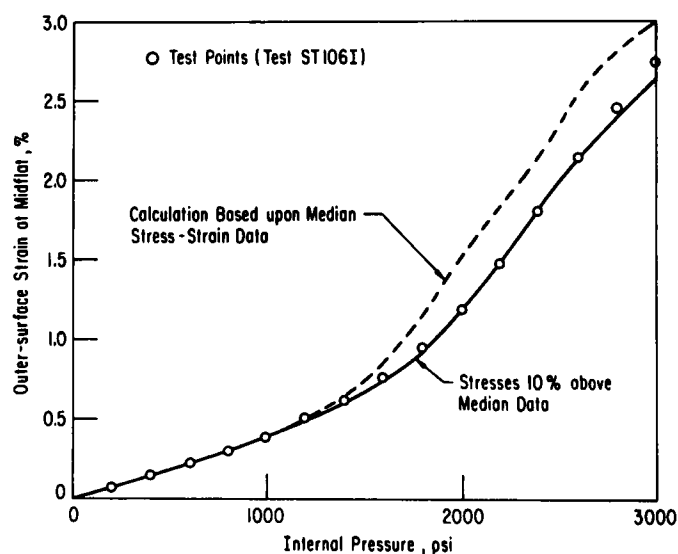


Fig. 54. Comparison of Experimental and Computed Outer-surface Midflat Strains for 50%-coldworked Type 316 Stainless Steel Internally Pressurized Hexcan (1 psi = 6.895 kPa). ANL Neg. No. 900-75-223.

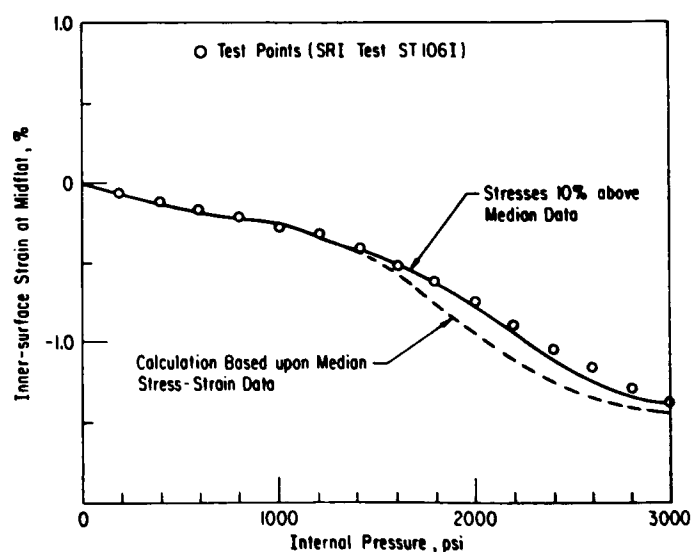


Fig. 55. Comparison of Experimental and Computed Inner-surface Midflat Strains for 50%-coldworked Type 316 Stainless Steel Internally Pressurized Hexcan (1 psi = 6.895 kPa). ANL Neg. No. 900-75-225.

surface would show a reversal in direction and approach the tensile-strain values of the upper surface; i.e., the strain gradient across the wall thickness would become uniform as the hexcan expands out to a circular shape.

## 2. External-pressurization Tests

The response of the 50%-coldworked hexcan to external pressurization did not show the unstable pantograph buckling mode exhibited by the externally loaded annealed hexcan. A reasonably uniform bending mode of collapse appeared to initiate at an external pressure of about 1200 psi (8.3 MPa), as shown in Figs. 56-59. Hence, the 50%-coldworked hexcan was much more

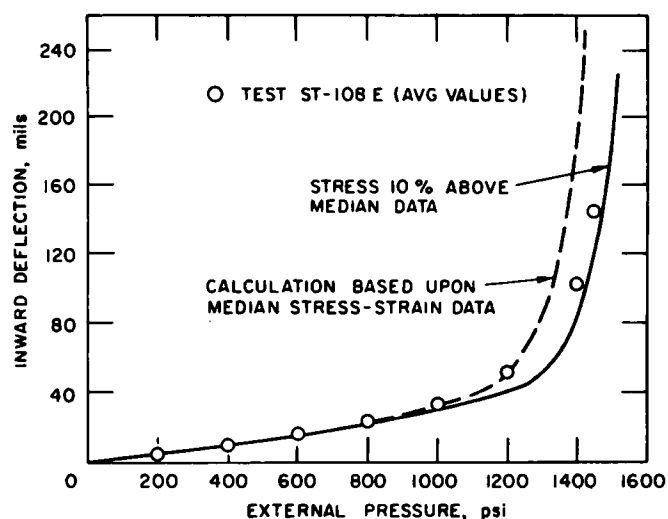


Fig. 56. Comparison of Experimental and Computed Midflat Deflections for 50%-coldworked Type 316 Stainless Steel Externally Pressurized Hexcan (1 mil = 0.0254 mm; 1 psi = 6.895 kPa)

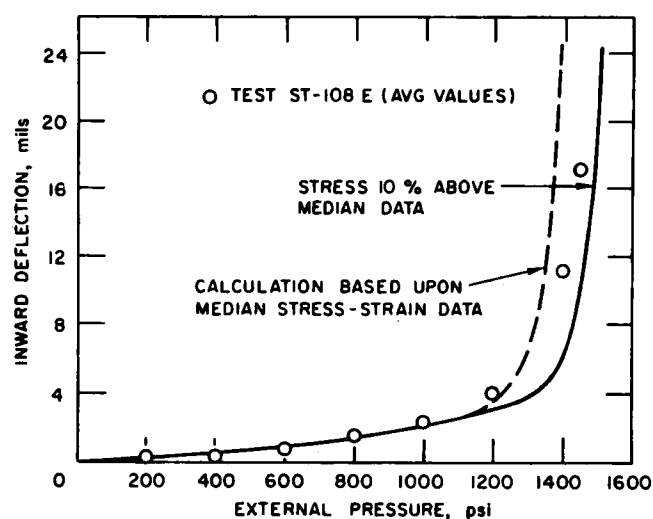


Fig. 57. Comparison of Experimental and Computed Corner Deflections for 50%-coldworked Type 316 Stainless Steel Externally Pressurized Hexcan (1 mil = 0.0254 mm; 1 psi = 6.895 kPa)

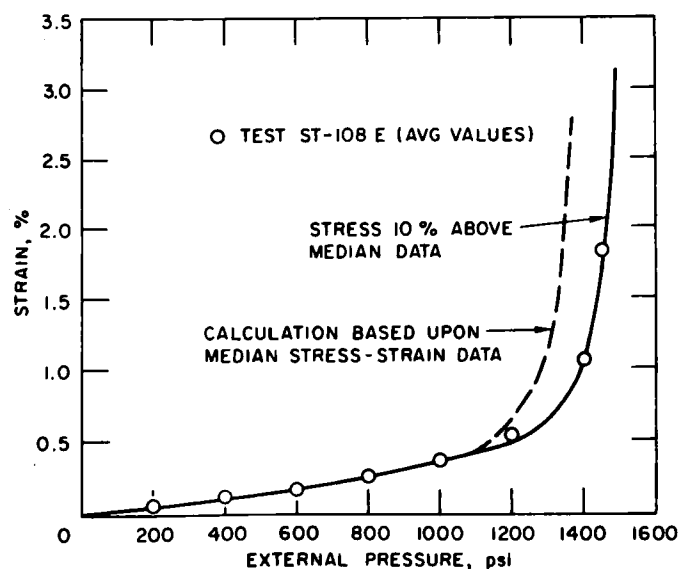


Fig. 58. Comparison of Experimental and Computed Inner-surface Midflat Strains for 50%-coldworked Type 316 Stainless Steel Externally Pressurized Hexcan (1 mil = 0.0254 mm; 1 psi = 6.895 kPa)

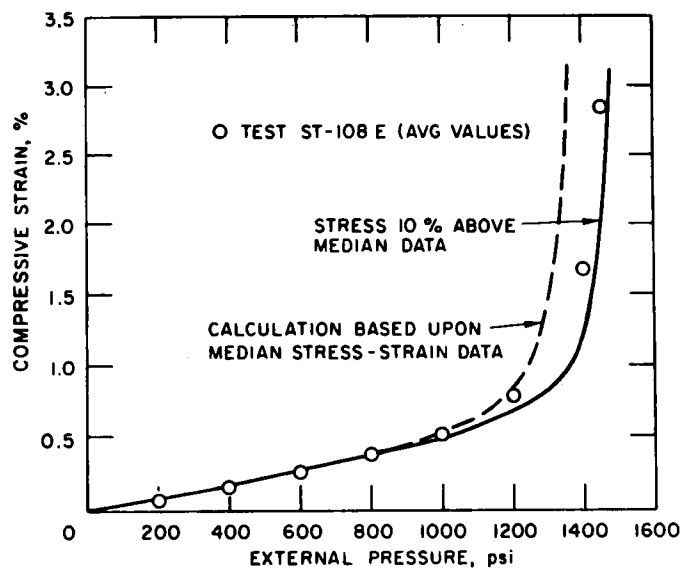


Fig. 59. Comparison of Experimental and Computed Outer-surface Midflat Strains for 50%-coldworked Type 316 Stainless Steel Externally Pressurized Hexcan (1 mil = 0.0254 mm; 1 psi = 6.895 kPa)

rigid to external loads than the annealed hexcan, which began to collapse at about 400 psi (2.8 MPa) (see Figs. 45 and 46). The midflat and corner deflections in Figs. 56 and 57 increased linearly with pressure out to about 1100 psi (7.6 MPa), and the computed and experimental values correlate very well. Beyond 1100 psi (7.6 MPa), the deflections increased very rapidly.

If the material properties are assumed to correspond to the median of the tensile-test data, the computed deflections are greater than the measured deflections, whereas if the material properties are assumed to correspond to the less ductile upper range of the tensile-test data (10% above the median), then the hexcan is slightly too stiff; i.e., the computed deflections are less than the measured values. Hence, the two computed curves bracket the experimental values. For the strains at the inner and outer midflat surfaces shown in Figs. 58 and 59, the computed curves appear to correlate best with the assumed upper range of stress-strain material properties. The better correlation with the assumed less ductile material properties is consistent with the comparisons for the internal-pressurization tests. We can conclude that the STRAW computations for the externally loaded hexcan compares with the experimental values within the data spread possible because of uncertainties in the material properties.

## VI. SUMMARY AND CONCLUSIONS

Test LMFBR-type hexcans have been subjected to hydrostatic internal and external pressure loads, and the measured deformations and strains have been compared with computed values. These hydrostatic tests and the corresponding comparisons with analysis constitute the first phase of an experimental and analytical program to predict the mechanical response of LMFBR-type subassemblies to pressure loadings from local-subassembly accidents. The purpose of the experiments is to provide data for the validation and, when necessary, modification and extension of the computational models. The resulting substantiated computer codes will then be available to calculate the response of subassembly ducts under in-reactor accident conditions with reasonable confidence.

The mechanical material properties of the Type 316 stainless steel hexcans were found to have a strong influence upon the deflection magnitude resulting from a given hydrostatic loading. To study the effects of the mechanical properties, the ductility of several sample test hexcans was increased by annealing the nominal 20%-coldworked hexcan material that was received from the vendor. In addition, several low-ductility hexcans were manufactured with a final coldworking of 50% to provide even more brittle samples.

Consequently, hydrostatic test data were available for three different hexcan material properties: (1) annealed steel with a yield stress of 25 ksi (172.4 MPa); (2) nominal 20% coldworking with a yield stress of 98 ksi (675.7 MPa); and (3) 50% coldworking with a yield stress of 118 ksi (813.6 MPa).

Decreasing the ductility significantly reduced the hexcan deflections: For an internal pressurization of 2000 psi (13.8 MPa), the deflection of the annealed hexcan was about 240 mils (6.1 mm); for the nominal 20%-coldworked hexcan, the deflection was decreased to 110 mils (2.8 mm), less than one-half the deflection for the annealed material; and for the 50%-coldworked hexcan, the peak deflection was 53 mils (1.3 mm), a reduction to about one-half that for the 20%-coldworked duct.

Hardening the steel increased the "strength" in the sense that the deflection response to a given pressure load decreased; increased hardening diminished the maximum local strain that the hexcan could withstand without rupturing. However, it is not clear that hardening will increase the capacity of a hexcan to withstand internal pressurization without rupturing. Two opposing mechanisms must be taken into consideration: (1) Hardening increases the yield stress so the hexcan is more resistant to deformation, and (2) hardening apparently lowers the allowable local failure strain, so that the more brittle material will fracture at a smaller deformation. The trade-off between these two mechanisms is illustrated by the fact that, because of its ability to tolerate a large local strain, the annealed hexcan withstood an internal pressurization of about 4500 psi (31 MPa) before rupturing. On the other hand, because of the much reduced allowable local strain, the 20%-coldworked hexcan failed at 2400 psi (16.5 MPa).

Further hardening reversed the trend of diminishing pressurization capacity; the increased resistance to deformation of the 50%-coldworked hexcan permitted the pressure to reach 3100 psi (21.4 MPa) before rupture occurred. This pressure is higher than the rupture pressure for the 20%-coldworked hexcan, but is lower than that for the annealed hexcan. These observed hexcan rupture failures for only three tests do not provide an adequate experimental basis to form conclusive generalizations about hexcan fracture. The occurrence of fracture may depend strongly upon preexisting microcracks and imperfections in the corner. To resolve these issues, a further study of the fracture mechanics involved in hexcan failures and experiments designed to investigate fracture phenomena must be performed.

The correlations between the hydrostatic-test results and the computations for the annealed and the 50%-coldworked hexcans provide sufficient substantiation of the computer code STRAW to permit proceeding to the next phase of the program, which involves the investigation of the dynamic response of hexagonal-duct subassemblies.

The annealed and the 50%-coldworked test hexcans cover a wide range in material ductility. For both steel hardnesses, the mechanical properties were carefully determined by an extensive series of tensile tests, and the uniformity of the properties throughout the hexcan was established by microhardness surveys both along the duct length from corner to midflat and through the wall thickness. The correlation between the experimental data and the computations for the nominal 20%-coldworked hexcan was also good.

No attempt was made to alter the initial nonuniform material properties of the hexcan in the condition it was received from the vendor. A microhardness survey indicated the corner regions to be significantly harder, up to a 35%-coldworking value. A detailed determination of the stress-strain relationship for each degree of coldworking throughout the hexcan was not made; consequently the correlation between the hydrostatic pressurization results and the computations for the nominal 20%-coldworked hexcan is not considered in itself to represent a sufficient validation of the STRAW code.

Experience gained from the performance of the hydrostatic tests and the calculations will be of value in executing and interpreting dynamic tests. The sensitivity of material properties upon the response has been revealed and demonstrates the desirability of maintaining uniform properties throughout the test hexcan. Further, for the evaluation of the dynamic tests, strain-rate effects should be taken into consideration.

It has been demonstrated that a test hexcan length of 1 ft (30.48 cm) is sufficient to provide a representative plane-strain central section free from end effects. Plane-strain deformation data are necessary for comparisons with the two-dimensional STRAW code and are maintained over the central section when the axial displacements of the sample hexcan are constrained by the test rig.

For the externally pressurized test hexcans, good correlations were obtained for small deflections. Under higher external pressure loads, the empty hexcan became mechanically unstable, and large asymmetric deflection modes developed. Under actual reactor operating conditions, this instability will be eliminated in fuel subassemblies by the symmetric support provided by the internal fuel-pin structure. However, this would not necessarily be true for control subassemblies that are empty during operation.



## APPENDIX A

### The STRAW and SADCAT Codes

#### 1. The STRAW Code

The STRAW code is a finite-element computer code designed to analyze transient dynamic structural-analysis problems that can be modeled by a system of flexural-beam elements. The code is limited to treat only one- or two-dimensional problems. Hence, the application of the code to analyze hexcan deformations is restricted to cases in which variations in the axial  $z$  direction can be neglected. Referring to Figs. B.1 and B.2 of Appendix B, we see that variations are confined to the transverse  $(r, \theta)$  plane, and the computations are applied to a representative cross-sectional sector of unit height in the  $z$  direction. Because of symmetry, only 1/12th of the cross-sectional hexcan perimeter need be considered. The hydrostatic pressurization is uniformly distributed, so that symmetry boundary conditions apply at the midflats and corners, and the computation need be applied only to the region between the midflat and corner of one face. This region is partitioned into flexural-beam elements as shown in Fig. B.1 of Appendix B. Each beam element is divided into longitudinal fibers, which can be extended or compressed.

The fibers are assumed to be independent, in the sense that no mutual shearing stresses are exerted between fibers, so that only uniaxial stresses are considered to occur in the beam element. A local coordinate system is attached to each element and is convected with the element. The flexural-beam equations are expressed relative to this coordinate system so that arbitrarily large rotations and translations may occur, provided that deformations relative to the coordinate system are small. This means that the magnitudes of the strains, and also the relative rotations of transverse planes, must be limited. The specific magnitude of the limitation depends upon the problem under consideration. For the hexcan, comparisons with experimental data indicate that strains could reach 20% in the corners while reasonably good correlations with computed deflections are maintained.

For each beam element, the STRAW code computes the distribution of strains over the ends of the element. To understand the nature of the approximations made to compute the strains, the main concepts involved in the computational model will be briefly summarized.

The flexural-beam element consists of a neutral axis coincident with the rigid-frame  $x$  axis. The  $y$  axis is normal to the  $x$  axis, and under flexure the transverse planes rotate through an angle  $\varphi$  with respect to the  $y$  axis. If we consider the beam to have a deflection shape with respect to the  $x$  axis, then  $\varphi$  is the slope of that shape and  $\partial\varphi/\partial x$  is the curvature. The length  $\ell$  of the beam element is defined by the straight-line distance between lumped-mass nodal points. The nodal points defining the ends of two adjacent beam elements carry the sum of one-half the mass of each element.

The internal and external forces are also concentrated at the nodal points, so that the nodal displacement can be computed by numerical integration of the equations of motion of the nodal mass points. The convected nodal points determine the x-axis position, and the distance  $\ell$  determines the membrane strain  $\epsilon_m$  of the neutral-axis fiber, which is assumed uniform through the length of the element. The angular rotation of the transverse plane is computed by numerical integration of the rotational equation of motion for the node. For the rotational equation of motion, the beam moments of inertia are lumped at the nodes and the resulting angular acceleration under the action of the moment applied at the node is integrated to give the angular displacement. The strain at any transverse location  $y$  measured from the neutral axis is the superposition of the membrane strain and the bending strain:

$$\epsilon = \epsilon_m - y \frac{\partial \varphi}{\partial x}.$$

A shape function must be assumed to determine the curvature  $\partial \varphi / \partial x$ . The displacement shape is approximated by a cubic polynomial. The coefficients of the polynomial are determined from the boundary conditions (i.e., zero displacements and known slopes  $\varphi_1$  and  $\varphi_2$  at the ends). The resulting strain distributions at the ends are

$$\epsilon = \epsilon_m + y \frac{4\varphi_1 + 2\varphi_2}{\ell} \quad \text{at } x = 0$$

and

$$\epsilon = \epsilon_m - y \frac{2\varphi_1 + 4\varphi_2}{\ell} \quad \text{at } x = \ell.$$

We see here the reason for the small-strain limitation. The membrane strain  $\epsilon_m$  is assumed uniform over the element, and the flexurally deformed transverse planes are assumed to remain plane.

One advantage of the finite-element method over finite-difference methods is that the elements into which the region is partitioned can be much larger, so that relatively few elements are required. However, because the membrane strain actually varies along the total length, rather than remaining uniform as in a single element, and since the displacement curve will not in general be exactly fitted by a cubic polynomial, it is necessary to introduce enough elements to yield a satisfactory resolution of strains, deflections, and dynamic frequencies. In particular, because of the high strain gradients in the corner region of the hexcan, the size of the element is limited.

Although resolution is improved by the use of smaller elements, a penalty is paid in greatly increased computer running time. The number of computational cycles is increased because of the stability requirements

imposed upon the maximum allowable time increment. The time step should be limited so that, in each time cycle, a longitudinal membrane wave will propagate no further than about 40-80% of the smallest element. For the hexcan section partitioned (as shown in Fig. B.1 of Appendix B) into eight elements, the time increment was limited to  $0.2 \mu\text{sec}$ . Hence, for example, to cover a time increment of only 4 msec, 20,000 computational cycles are required. As a general rule of thumb, when the number of cycles reaches the order of  $10^5$ , round-off errors can become significant. Also to be considered is the error accumulation resulting from the approximations made in the numerical model (e.g., lumping of masses and inertial moments at the nodes, truncation errors from neglect of higher-order strain terms and linearizations, shape-function assumptions, and finite time increment).

## 2. The SADCAT Code

For hydrostatic pressurization, the loading exerted on the hexcan walls is uniformly distributed with no variations in the axial  $z$  direction. For a sufficiently long hexcan section [experiments indicate that a 1-ft (30.48-cm) length is adequate], the end effects do not extend to the central test section, so that deformations in this section are essentially two-dimensional. Variations are constrained to the transverse  $(r, \theta)$  plane. However, to compute deformations in the end regions, variations in the  $z$  direction must also be considered. To include the effects of nonuniformities in the axial  $z$  direction, the analysis has been extended and a new code called SADCAT, which has the capability to treat three-dimensional plate and shell problems, has been developed.

An example of a SADCAT computation of the deflection profile in the  $z$  direction is shown in Fig. A.1. This computation was performed to investigate the effect of axially constraining the ends of the test hexcan. We see in Fig. A.1 that the axial constraint has little effect upon the deformation for

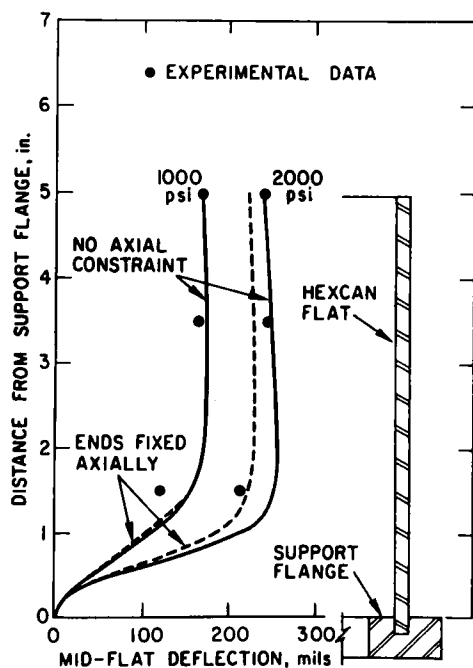


Fig. A.1

SADCAT Computation of Influence of End Constraints upon Longitudinal Deflection Profile and Comparison with Measured Deflections for Annealed Type 316 Stainless Steel Internally Pressurized Hexcan (1 in. = 2.54 cm; 1 psi = 6.895 kPa; 1 mil = 0.254 mm). ANL Neg. No. 900-5310.

an internal pressure of 1000 psi (6.9 MPa). However, for an increased pressure of 2000 psi (13.7 MPa), the influence of the end constraint is to reduce the deflection. It may also be noted that the SADCAT code computes a slight bulging at about 1 in. (2.54 cm) from the support flange at the end. Comparison of the computed deflections with the experimental measurements is reasonably consistent, but the presence of the end bulging is not corroborated. The increasing influence of the end constraint with increasing pressure is shown in Fig. A.2.

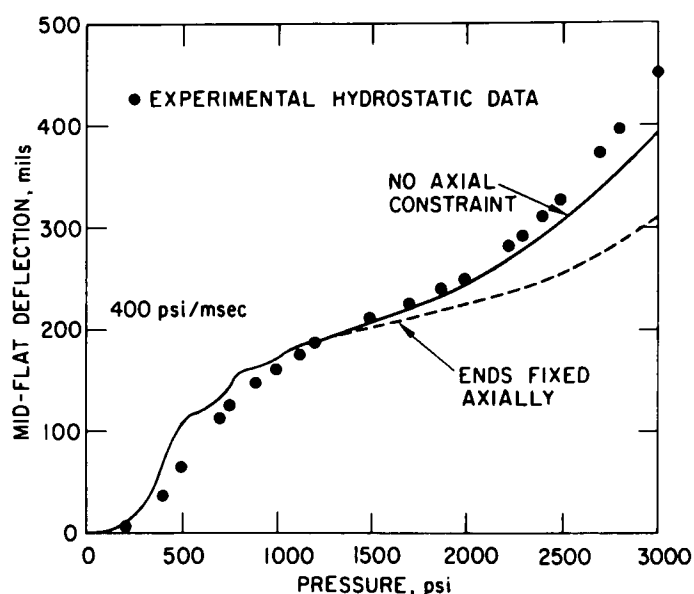


Fig. A.2

SADCAT Computation of Influence of End Constraints upon Maximum Midflat Deflection for Annealed Type 316 Stainless Steel Internally Pressurized Hexcan (1 mil = 0.0254 mm; 1 psi = 6.895 kPa). ANL Neg. No. 900-5318.

Attempts have been made to maintain two-dimensional conditions under dynamic loading conditions by designing a line source of uniform strength. By positioning this line source along the axis of the hexcan, it is hoped that the pressure distribution in the axial direction can be uniform, and that deflections and strains can be compared with the STRAW code. However, if this line source is not centrally located, the pressure loading will not be axisymmetric, and the hexcan will bend as a beam between its end supports. In this case, variations in strains will occur in the axial direction and the three-dimensional SADCAT code will be required. Three-dimensional effects will also arise if the line source is of nonuniform strength or if a point source is used.

Similarly to STRAW, the SADCAT code is formulated as a lumped-mass system and follows an explicit time-integration computational procedure. The code is especially suited for structures subjected to high loading rates because of its capability to treat inelastic material deformations and large displacements.

The formulation within the code is based on the finite-element procedure, in which the discrete model of the structure consists of an assemblage of flat, triangular plate elements connected by nodes. Each element is associated with a convected coordinate system, which is attached to the element.

The convected coordinate system moves with the element and approximates the rigid-body motion of the element. In addition, each node is associated with a set of body coordinates, which rotate with the node and coincide with the principal axes of the mass moment of inertia of the node.

The lumped masses and rotational inertias of the nodes are obtained by the following procedure. The mass and moment of inertia of each element are calculated and then subdivided into three equal parts, each associated with the respective node of the element. When this procedure is applied to all elements, the final mass and moment of inertia at each node consist of contributions from all adjacent elements. At the node, the principal moments of inertia are determined, and the associated principal directions constitute the initial body coordinates.

The total displacement of the element is decomposed into a rigid-body motion and a deformation. The rigid-body motion is defined by the motion of the convected coordinate system; the deformation of the element is measured by the displacement relative to the convected coordinates. Rotations of the nodal coordinates are described by Euler angles, and the components are updated at every time step. The plate element is assumed to have linear in-plane displacements and cubic transverse displacements. The deformation displacements are computed from the relative displacements and relative rotations of the nodes. Following Argyris,<sup>10</sup> the in-plane deformations are determined by side elongations of the element. The nonconforming shape functions developed by Bazeley<sup>11</sup> determine the flexural component of deformation. The strains are computed in the convected coordinate system. The first derivative of the in-plane displacement provides the membrane component of strain, and the second derivative (curvature) of the shape function yields the flexural component of strain.

Internal nodal forces and moments are derived using a five-point trapezoidal integration across the element thickness and a three-point integration over the element plane. The transverse nodal forces are obtained from the requirement that the nodal forces of an element must be self-equilibrated. In some problems in which the residual membrane forces are large and no external loads are present, there is a tendency for certain nodes to oscillate in a snap-through mode. This effect is eliminated by use of a membrane artificial viscosity, which can be specified as a percentage of critical damping.

The tensile data of true stress versus engineering strain are approximated by a multilinear curve with isotropic strain hardening. Yielding in the biaxial state of stress is handled by the von Mises yield criterion (see Appendix B), and a flow rule is assumed in the plastic regime. The plastic components of stress are evaluated by an algorithm introduced by Hartzmann and Hutchinson.<sup>12</sup>

The code accepts pressure-time histories, initial velocities, and displacements as external loads. With the mass, moments of inertia, and external and internal forces known, the equations of motion are applied at the nodes. The equations of motion are integrated in time using the Newmark- $\beta$  method.<sup>13</sup> Since the formulation is based on an explicit integration, the length of the prescribed time step is limited by a stability criterion. The code operation has been found to be quite efficient, taking about 2 msec per time step per element on an IBM 370/195 computer.

## APPENDIX B

The Plane-strain Assumption1. The Elastic Range and Initial Yield Point

Since STRAW is a two-dimensional code, variations in the radial  $r$  and the circumferential  $\theta$  directions are computed, while variations in the axial  $z$  direction are assumed to be zero (see Figs. B.1 and B.2). For a hydrostatically pressurized hexcan, the pressure loading on the walls is uniform, and if the hexcan ends are constrained, displacements in the  $z$  direction can be assumed negligible. In this case, strain components are confined to the transverse  $(r, \theta)$  plane and the deformations are referred to as "plane strain."

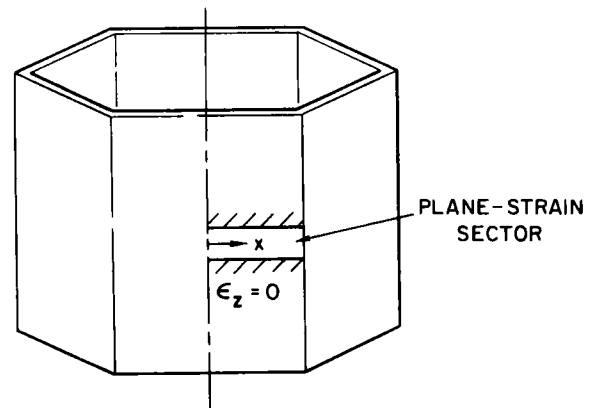
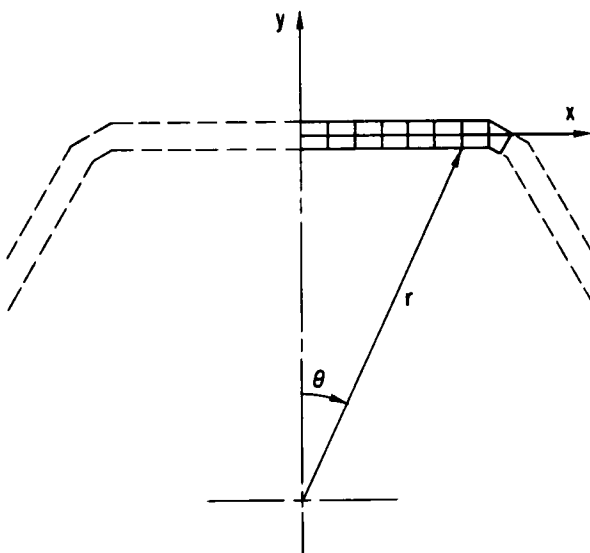
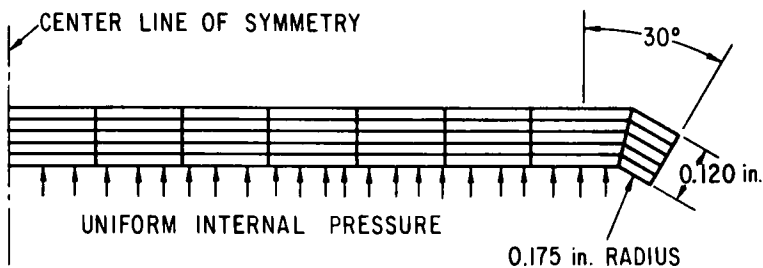


Fig. B.2. Representative Hexcan Sector for Plane-strain Conditions

Fig. B.1. Top View of Hexcan Showing Beam Elements That Deflect Radially Outward for an Internal Pressurization (1 in. = 2.54 cm). ANL Neg. No. 900-4596 Rev. 1.

Before the specific plane-strain problems are considered, it is instructive to refer to the general three-dimensional elastic relationships between the stresses and strains in the  $x$ ,  $y$ , and  $z$  directions:

$$\epsilon_x = \frac{\sigma_x}{E} - \frac{\nu}{E}(\sigma_y + \sigma_z), \quad (1x)$$

$$\epsilon_y = \frac{\sigma_y}{E} - \frac{\nu}{E}(\sigma_z + \sigma_x), \quad (1y)$$

and

$$\epsilon_z = \frac{\sigma_z}{E} - \frac{\nu}{E}(\sigma_x + \sigma_y). \quad (1z)$$

The Young's elastic modulus  $E$  can be determined in a tensile-test machine. Usually a test specimen in the form of a straight narrow rod is pulled, and the load and corresponding extension of the rod are measured. The plot of stress versus strain is a straight line of slope  $E$ . When the load is increased, a point is reached at which the linear relationship fails, marking the "linear elastic limit," or "proportional limit" or "yield point." Over the elastic range, the general equations applied to the tensile-test specimen reduce to the simple forms

$$\epsilon_x = \frac{\sigma_x}{E}, \quad (2x)$$

$$\epsilon_y = -\nu\epsilon_x, \quad (2y)$$

and

$$\epsilon_z = -\nu\epsilon_x. \quad (2z)$$

Equation 2x represents the straight-line "uniaxial stress-strain relationship." Equations 2y and 2z demonstrate the lateral contraction of the rod as a fraction  $\nu$  (Poisson's ratio) of the extension. In terms of the hexcan, Eq. 2y demonstrates the reduction of wall thickness when the beam elements (see Fig. B.1) are extended under internal pressurization. Equation 2z shows that the hexcan will also contract axially in length, if the ends are free, by the same proportion  $\nu$  of the principal strain in the  $x$  direction.

If the contraction  $\epsilon_z$  of the hexcan length is constrained ( $\epsilon_z = 0$ ), then a resisting stress  $\sigma_z$  must be set up in the  $z$  direction. The element then has two stress components  $\sigma_x$  and  $\sigma_z$ , and will be in a biaxial rather than uniaxial state of stress. Since  $\epsilon_z$  is zero, this is a plane-strain case, and the general equations for this case become

$$\epsilon_x = \frac{\sigma_x}{E} - \frac{\nu}{E}\sigma_z, \quad (3x)$$

$$\epsilon_y = -\frac{\nu}{E}\sigma_z + \sigma_x, \quad (3y)$$



and

$$0 = \frac{\sigma_z}{E} - \frac{\nu}{E} \sigma_x. \quad (3z)$$

From Eq. 3z we see that

$$\sigma_z = \nu \sigma_x. \quad (4)$$

This relationship between the stress components is similar to the relationship (Eq. 2z) between the strain components for the uniaxial stress case of the tensile-test specimen. Combining Eq. 4 with Eq. 3x gives the relationship between the extensional stress and strain of the beam fibers:

$$\epsilon_x = \frac{1 - \nu^2}{E} \sigma_x. \quad (5)$$

An "equivalent plane-strain Young's modulus" can be defined as

$$E_p = \frac{1}{1 - \nu^2} E. \quad (6)$$

Hence, constraining the ends makes the hexcan more resistant to deflections. The beam elements composing the plane-strain hexcan sector are stiffened by the factor  $1/(1 - \nu^2)$ .

Not only is the slope of the linear stress-strain relationship increased for the plane-strain case, but the elastic range is also increased. The equivalent plane-strain yield stress is greater than the uniaxial yield stress measured for the tensile-test specimen. The increase in the yield stress is determined from the von Mises yield criterion. For the von Mises criterion, the locus of yield points is expressed as a "yield surface" in a space having the stresses as coordinates. The yield surface is a circular cylinder in this stress space and consists of all points equidistant from the hydrostatic line ( $\sigma'_x = \sigma'_y = \sigma'_z$ ).

The assumption is made that, since a material in a state of hydrostatic equilibrium has no tendency to yield, then all points that are in a state of stress equally removed from the hydrostatic state have an equal tendency to yield. If we let subscripts X, Y, and Z indicate yield values, the equation for the principal stresses (i.e., normal to the principal planes of zero shear) is

$$(\sigma_X - \sigma_Y)^2 + (\sigma_Y - \sigma_Z)^2 + (\sigma_Z - \sigma_X)^2 = R^2. \quad (7)$$

The constant cylinder radius  $R$  is found from the tensile-test specimen, which is in a uniaxial state of stress ( $\sigma_y = \sigma_z = 0$ ). Substituting these values

into Eq. 7, we see that this radius is directly proportional to the yield stress  $Y_0$  measured in the test:

$$R = \sqrt{2}Y_0. \quad (8)$$

Under plane-strain conditions, the beam elements are in a biaxial state of stress ( $\sigma_y = 0$ ), so that the locus of yield points is an ellipse:

$$\sigma_X^2 - \sigma_X\sigma_Y + \sigma_Z^2 = Y_0^2. \quad (9)$$

Substituting the value for the z component given by Eq. 4 into Eq. 9, the equivalent plane-strain yield stress is

$$\sigma_X = \frac{1}{\sqrt{1 - \nu + \nu^2}} Y_0. \quad (10)$$

The relationship on the von Mises yield ellipse is illustrated in Fig. B.3.

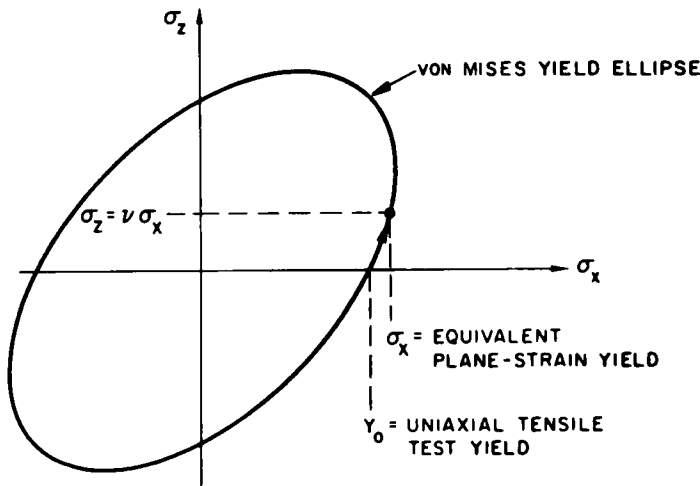


Fig. B.3

Increase in Plane-strain Yield Stress  
over Uniaxial Tensile-test Yield Stress

## 2. Plastic Flow and Subsequent Yields

Because of stress concentrations in the hexcan corner region, the elastic limit can be easily exceeded under moderate pressure loads. Plastic deformations have been found to occur for internal-pressurization values of the order of 150 psi (1.0 MPa). When plastic flow occurs, we are faced with the problem of applying the available uniaxial tensile-test data to the biaxial stress conditions imposed by the plane-strain constraint.

The tensile-test data were transformed to a form suitable for the plane-strain case by a simple procedure. The method consisted of increasing the slope of the plastic strain-hardening curve derived from the tensile-test data by the factor  $4/3$  at each point

$$\bar{E}_p = \frac{4}{3}E_p. \quad (11)$$



then the relationship between this actual slope and the two slopes defining the elastic and plastic components of the total strain is

$$\frac{1}{E_{\tan}} = \frac{1}{E} + \frac{1}{E_p}. \quad (13)$$

Since the Young's modulus  $E$  is large compared to the plastic slope  $E_p$ , the approximation is made that the total strain is nearly equal to the plastic strain:

$$\delta \epsilon_x \approx \delta \epsilon_x^p. \quad (14)$$

The yield surface corresponding to Eq. 7 may be expressed as a function of the principal stresses:

$$f(\sigma_x, \sigma_y, \sigma_z) = Y^2. \quad (15)$$

For deformation states that return to the inside of the current yield surface, the material will behave elastically, i.e., for states  $(\sigma_x, \sigma_y, \sigma_z)$  that satisfy the local condition

$$f(\sigma_x, \sigma_y, \sigma_z) < Y^2. \quad (16a)$$

If the loading is increased so that the state points progress outside the yield surface, the material will behave plastically, i.e., for states that satisfy the local condition

$$f(\sigma_x, \sigma_y, \sigma_z) > Y^2. \quad (16b)$$

It has been shown by Drucker<sup>14</sup> that if the incremental plastic strain  $\delta \epsilon^p$  is assumed to be linearly proportional to the incremental stress  $\delta \sigma$ , then the plastic-strain vector is perpendicular to the yield surface:

$$\vec{\delta \epsilon^p} = \lambda \vec{\nabla} f, \quad (17)$$

where  $\lambda$  is a scalar and  $\vec{\nabla} f$  is the gradient of the yield surface.

Equation 17 can be applied to the uniaxial stress case of the tensile test, for which the yield surface (Eq. 14) reduces to

$$f(\sigma_x) = \sigma_x^2 = Y^2. \quad (18)$$

For the uniaxial test, Eq. 17 becomes

$$\delta \epsilon_x^p = \lambda \frac{\partial f}{\partial \sigma_x} = \lambda 2\sigma_x = \lambda 2Y. \quad (19)$$

The plastic-slope definition gives

$$\delta \epsilon_x^p = \frac{1}{E_p} \delta \sigma_x, \quad (20)$$

and since the uniaxial stress increment becomes the new yield stress,

$$\delta \sigma_x = \delta Y. \quad (21)$$

The unknown scalar  $\lambda$  can be determined by combining the above three equations to give

$$\lambda = \frac{1}{2E_p} \frac{\delta Y}{Y}. \quad (22)$$

Thus the local value of  $\lambda$  can be determined from the uniaxial test data.

The next step is to proceed to the plane-strain biaxial-stress case using the information about  $\lambda$  and  $Y$  obtained from the uniaxial tensile test. For the biaxial-stress state, the yield surface is of the form of Eq. 9:

$$f(\sigma_x, \sigma_z) = \sigma_x^2 - 2\sigma_x\sigma_z + \sigma_z^2 = Y^2.$$

The  $x$  component of the gradient to the constant- $y$  yield surface is

$$\frac{\partial f}{\partial \sigma_x} = 2\sigma_x - \sigma_z. \quad (23)$$

The  $z$ -component stress is related to the  $x$  component through the gradient in the  $z$  direction:

$$\frac{\partial f}{\partial \sigma_z} = 2\sigma_z - \sigma_x.$$

Now, the incremental strain in the  $z$  direction is

$$\delta \epsilon_z = \lambda \frac{\partial f}{\partial \sigma_z},$$

and for plane strain  $\delta \epsilon_z = 0$ . Combining the above two equations gives

$$\sigma_z = \frac{1}{2} \sigma_x. \quad (24)$$

It is interesting to compare this relationship with Eq. 4. For fully plastic flow, the incompressibility condition gives  $\nu = 0.5$ , so that Eq. 4 for the elastic material is consistent with Eq. 24 for the plastic material.

The incremental strain in the  $x$  direction is

$$\delta \epsilon_x^p = \lambda \frac{\partial f}{\partial \sigma_x}. \quad (25)$$

Combining this equation with Eqs. 23 and 24 gives

$$\delta \epsilon_x^p = \frac{3}{2} \lambda \sigma_x. \quad (26)$$

If the value of  $\lambda$  (from Eq. 22) determined from the uniaxial test is used, the incremental plastic strain becomes

$$\delta \epsilon_x^p = \frac{3}{4E_p} \frac{\delta Y}{Y} \sigma_x. \quad (27)$$

The relationship between the uniaxial tensile-test yield stress  $Y$  and the equivalent plane-strain yield stress  $\sigma_x$  is of the same form (Eq. 10) as for the initial yield surface. Thus,

$$\sigma_x = \frac{1}{\sqrt{1 - \nu + \nu^2}} Y. \quad (28)$$

Since an increment in the stress produces a new yield surface,

$$\delta \sigma_x = \frac{1}{\sqrt{1 - \nu + \nu^2}} \delta Y. \quad (29)$$

Combining the above two equations gives the similar ratios

$$\frac{\delta \sigma_x}{\sigma_x} = \frac{\delta Y}{Y}. \quad (30)$$

Hence, from Eq. 27, the incremental strain for the plane-strain case becomes

$$\delta \epsilon_x^p = \frac{3}{4E_p} \delta \sigma_x. \quad (31)$$

An "equivalent plane-strain plastic slope" can be defined by

$$\delta \epsilon_x^p = \frac{1}{\bar{E}_p} \delta \sigma_x. \quad (32)$$

Comparing the above two equations demonstrates the transformation of Eq. 11.

Note that in the preceding discussion, the  $(x, y, z)$  directions defined in Figs. B.1 and B.2 are assumed to correspond to the principal-stress

directions for which the yield surface is defined. This assumption is consistent with the model described for the STRAW code in which each longitudinal fiber of the finite flexural-beam element acts as an independent membrane with no internal shear stresses. It follows that the plane normal to the  $x$  direction is a principal plane. For the actual hexcan, we should note first that the planes of symmetry at the midflat and corner are principal planes because the shear stresses on these boundary planes are zero. Also, the wall surfaces have zero shears. Hence, the yield criterion derived above is a good approximation for the corner and midflat elements, and for the outside surfaces of all the elements. Since the outer fibers exert the greatest bending influence upon the deflection, the error in the approximation caused by actual shear stresses on the inner fibers should be minimal. Also, in the plastic-flow region, the shear stresses can be expected to be small compared to the normal stresses, even for the inner fibers.

## APPENDIX C

Analytical Representation of Stress-Strain Relationship

To compute the deformation of the hexagonal-subassembly wrappers when subjected to pressure loads, the stress-strain properties of the material must be determined. Because of the sensitivity of the response of the Type 316 stainless steel hexcan to its material properties, verification of the STRAW and SADCAT codes requires that the stress-strain relationship be known accurately over the complete range of strains, extending from the elastic over the entire range of strain-hardening plastic flow out to final material failure. The entire stress-strain range must be known because of the wide variation of strains appearing in the deformed hexcan, particularly for the stress-concentration regions in the corners.

The mechanical material properties were measured by the ANL Materials Science Division. Tensile tests were performed for specimens cut from the test-hexcan ducts, and the resulting stress-strain curves for annealed and 50%-coldworked hexcans are shown in Figs. 30 and 36. The point of maximum tensile load, called the "ultimate strength," for the 50%-coldworked specimen occurred at a relatively small strain (about 2%), whereas the major extension of the tensile specimen out to fracture occurred beyond the ultimate point (see Fig. 36). For the annealed tensile specimen (see Fig. 30), the ultimate point was not reached until the gage length was extended about 50%. The range of extension beyond this ultimate point out to failure was a much smaller proportion of the graph of total load versus elongation.

For extension below the ultimate strength point, the tensile specimen is in a state of uniform uniaxial stress and strain. At the ultimate strength, the specimen reaches a point of plastic instability, and a local contraction, or necking, will occur at some cross section of the specimen gage length. Further strains will fail to be uniform, and the local strain cannot be measured by the total extension of the gage section of the specimen; i.e., the portions of the graphs in Figs. 30 and 36 beyond the maximum load point cannot be applied to computations involving the local stress-strain relationship of the material. The mean true stress at the necked-down section is the tensile load divided by the instantaneous area, and the mean strain at this section can be estimated from the ratio of the contracted area to the original area.

Because of the uncertainties involved in measuring accurate local strain values with increasing stresses, it is convenient to develop analytical expressions for the strain-hardening plastic-flow region that require only a few measurements. A method for determining an analytic expression that will aid in describing an appropriate stress-strain relationship for the STRAW code is described below.



The physical mechanism of the plastic-flow instability that results in a local necking down of the tensile-test specimen and destroys the uniformity of the strain distribution can be simply explained. If we consider a straight cylindrical filament subjected to a pure uniaxial tensile loading, the cross-sectional area will diminish when the filament length is increased. In the plastic-flow region, the material is essentially incompressible, so that for constant volume, the new area  $A$  and length  $\ell$  is related to the initial unloaded  $A_0$  and  $\ell_0$  by

$$A = A_0 \ell_0 / \ell. \quad (33)$$

For a tensile loading force  $P$ , the uniform "true" stress is

$$\sigma_t = P/A. \quad (34)$$

When the filament is strained, the increase in stress due to the reduction in area must be balanced by an increase in the stress resistance of the material. For a perfectly plastic material, the stress will not increase with the strain, and the material will continue to deform and not reach equilibrium. The increase in stress above that for perfect plasticity, called "strain hardening," permits the tensile specimen to sustain stresses above the yield point. However, a point is reached when the increase in material resistance is not sufficient to balance the effect of area reduction; this is the "ultimate strength" point.

The conventional engineering stress  $\sigma$  is the tensile test load  $P$  divided by the initial area  $A_0$  of the gage length of the tensile test specimen:

$$\sigma = P/A_0.$$

The engineering strain  $\epsilon$  is the extension of the gage length from the initial length  $\ell_0$  to the length  $\ell$  divided by the initial length:

$$\epsilon = (\ell - \ell_0)/\ell_0.$$

The strip chart from the tensile-test machine gives the plot of load  $P$  versus the extension  $\ell - \ell_0$ . Dividing these values, respectively, by the initial area  $A_0$  and initial length  $\ell_0$  will give a graph up to the ultimate point of engineering stress versus engineering strain. At the ultimate point, the load is a maximum and the slope of the graph is zero:

$$\frac{dP}{d\epsilon} = 0 = \sigma_t \frac{dA}{d\epsilon} + \frac{d\sigma_t}{d\epsilon}. \quad (35)$$

From Eq. 33, the engineering strain is related to the areas by

$$A_0 = A(1 + \epsilon), \quad (36)$$

and, since  $A_0$  is constant,

$$\frac{dA}{d\epsilon} = -\frac{A}{1 + \epsilon}. \quad (37)$$

Substituting Eq. 37 into Eq. 35 gives the condition for the ultimate point:

$$(1 + \epsilon) \frac{d\sigma_t}{d\epsilon} = \sigma_t. \quad (38)$$

If the "true" strain is defined to be

$$\begin{aligned} \epsilon_t &= \int_{\ell_0}^{\ell} \frac{d\ell}{\ell} = \ell \ln \frac{\ell}{\ell_0} \\ &= \ell \ln(1 + \epsilon), \end{aligned} \quad (39)$$

then Eq. 38 gives the condition for the ultimate point to occur when the slope of the true stress-strain curve is given by

$$\left( \frac{d\sigma_t}{d\epsilon_t} \right)_u = (\sigma_t)_u. \quad (40)$$

The ultimate strength point, specified by Eq. 40, indicates the onset of plastic instability and the initiation of necking in the tensile specimen. Because of the nonuniform strains that will result for further deformation, the load-extension data from the tensile tests will not directly establish the stress-strain states of the specimen. An assumption can be made that the true stress-true strain relationship is approximated by a power law of the form<sup>15</sup>

$$\sigma_t = B(\epsilon_t)^m, \quad (41)$$

where  $B$  and  $m$  are constants, and  $m$  is known as the strain-hardening exponent.

This equation is a straight line on a log-log plot, as shown in Fig. C.1:

$$\log \sigma_t = \log B + m \log \epsilon_t. \quad (42)$$

Two points (for example, the yield and ultimate) will determine the unknown  $B$  and slope  $m$ :

$$\left. \begin{aligned} \text{yield point:} \quad & (\sigma_t)_y = B(\epsilon_t)_y^m; \\ \text{ultimate point:} \quad & (\sigma_t)_u = B(\epsilon_t)_u^m. \end{aligned} \right\} \quad (43)$$

Eliminating B gives

$$\frac{(\sigma_t)_u}{(\sigma_t)_y} = \left[ \frac{(\epsilon_t)_u}{(\epsilon_t)_y} \right]^m \quad (44)$$

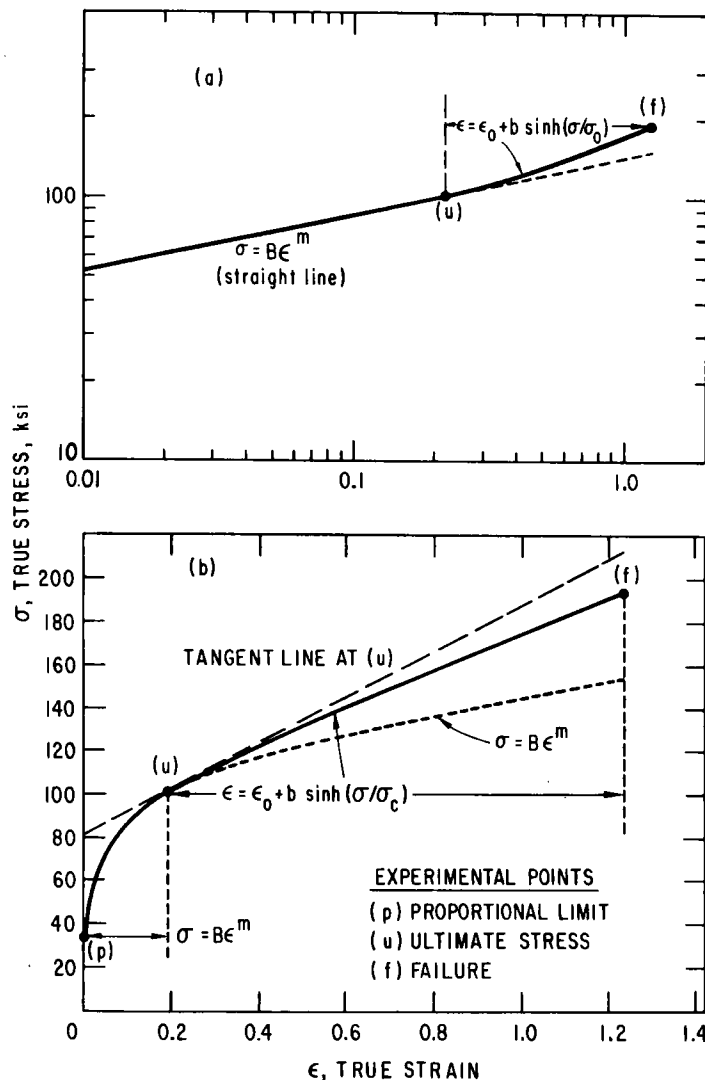


Fig. C.1. Empirical Fitting of Stress-Strain Relationship for Annealed Type 316 Stainless Steel (1 ksi = 6.895 MPa). ANL Neg. No. 900-5328 Rev. 1.

The coordinates of the yield point can be determined directly from the strip-chart data output from the tensile-test machine. The yield stress  $\sigma_y$  can be estimated fairly well as the point at which the graph begins to deviate from the straight line. The corresponding strain is given by

$$\epsilon_y = \sigma_y / E.$$

The stress and strain are the engineering values. The true stress value is obtained by combining Eqs. 33, 34, and 36 to give

$$\sigma_t = \sigma(1 + \epsilon). \quad (45)$$

It follows that the true yield stress is

$$(\sigma_t)_y = \sigma_y(1 + \epsilon_y).$$

The true yield strain is obtained from Eq. 39:

$$(\epsilon_t)_y = \ln(1 + \epsilon_y).$$

This yield point, defined at the proportional limit, has been de-

termined without reference to a measured strain value; only Young's modulus  $E$ , a measured load  $P$ , and the initial area  $A_0$  have been used.

The value of the ultimate stress is determined directly from the measured maximum load recorded on the strip chart. It is desirable to determine the ultimate strain without direct reference to displacement measurements. This can be accomplished by measuring the slope  $m$  of the log-log plot of true stress versus true strain as given by Eq. 42:

$$\begin{aligned}
 m &= \frac{d(\log \sigma_t)}{d(\log \epsilon_t)} \\
 &= \frac{\epsilon_t}{\sigma_t} \frac{d\epsilon_t}{d\sigma_t}.
 \end{aligned}
 \tag{46}$$

From Eq. 40, for the ultimate point, and Eq. 46 it follows that

$$m = (\epsilon_t)_u. \tag{46a}$$

From the definition (Eq. 39) for true strain,

$$1 + \epsilon = \exp(\epsilon_t).$$

Substituting this expression into Eq. 45 and using the value of the slope  $m$  given by Eq. 46a, the true stress at the ultimate point becomes

$$(\sigma_t)_u = \sigma_u \exp(m). \tag{47}$$

Substitution of this true-stress value and the true-strain value Eq. 46a into Eq. 44 gives

$$\frac{\sigma_u \exp(m)}{(\epsilon_t)_y} = \left[ \frac{m}{(\epsilon_t)_y} \right]^m \tag{48}$$

The value of  $m$  can be formed from this equation by a trial-and-error method of solution.

As an illustrative example, Eq. 48 will be solved for the 50%-coldworked tensile specimen listed as 1-50-B in Table VII. The 0.2% offset yield stress for this sample is 134.3 ksi (926.0 MPa), and the ultimate strength  $\sigma_u$  is 139.5 ksi (961.8 MPa). The engineering-yield-strain value is then

$$\begin{aligned}
 \epsilon_y &= 0.002 + \frac{134,300}{E} \\
 &= 0.006796.
 \end{aligned}$$

The corresponding value for the true yield strain is

$$\begin{aligned}
 (\epsilon_t)_y &= \ln 1.006796 \\
 &= 0.006773,
 \end{aligned}$$

and the true yield stress is

$$\begin{aligned}(\sigma_t)_y &= 134.3(1 + \epsilon_y) \\ &= 135.213 \text{ ksi (932.261 MPa)}.\end{aligned}$$

Substitution of the above values in Eq. 48 and solving for  $m$  by trial-and-error give

$$m = 0.040.$$

The value of this slope is also the value of the true strain at the ultimate point. The corresponding engineering value of the ultimate strain is then

$$\begin{aligned}\epsilon_u &= \exp(0.040) - 1 \\ &= 0.041.\end{aligned}$$

This value can be compared with the "maximum uniform strain" value of 0.034 that was estimated from the extensometer strain reading at the maximum load point. Estimates of the ultimate strain values from the strip-chart plot of the load versus extension are only approximate because the curve is very flat in the region of the peak load, and it is not possible to tell exactly at what strain the peak load occurs. Consequently, considerable scatter appears in the list of maximum uniform strain values in Table VII. Through the use of Eq. 48, the scatter in the computed values of  $m$  is greatly reduced.

Once the value of  $m$  is determined, it is simple to determine the constant  $B$ , and the graph of the true stress versus true strain is established by Eq. 41. The constant  $B$  is formed by substituting the coordinates of the yield point into Eq. 43 (or, alternatively, the coordinates of the ultimate point).

The power-law relationship (Eq. 41) can be checked at the final extended stress and strain values of the tensile specimen. If this final point does not fall on the power-law relationship, a hyperbolic-sine law can be used to fit the plastic-flow relationship from the ultimate point ( $u$ ) to the final failure point ( $f$ ) as shown in Fig. C.1.

The final necked-down cross section of the tensile specimen is severely strained, so that the strain distribution over the cross section is not uniform, and the resulting stress state is triaxial. An empirical correction method proposed by Bridgeman, described by Lubahn and Felgar,<sup>15</sup> will permit an equivalent uniaxial strain value to be determined based upon the measured final cross-sectional area.

## ACKNOWLEDGMENTS

We wish to thank Dr. D. J. Cagliostro, the project leader of the effort at the Stanford Research Institute, Mr. C. M. Romander, and their associates, who designed, built, and performed the experiments described here in cooperation with Argonne National Laboratory as part of the subassembly-to subassembly failure-propagation experimental program. Careful material-property characterization of subassembly ducts used in the tests, including tensile-test data and coldwork-gradient determinations, was performed by Messrs. C. A. Youngdahl, J. E. Slattery, and B. E. Lepacek of the ANL Materials Science Division. We also wish to acknowledge the contributions of other members of that division, including Drs. J. T. A. Roberts (now with the Electric Power Research Institute), J. J. Weins, and F. L. Yaggee, in the early stages of the program, plus the continuing interest and helpful discussions and suggestions of Dr. D. R. Diercks. Further, we appreciate the helpful discussions with Drs. J. M. Kennedy and A. H. Marchertas of the Engineering Mechanics Section of the Reactor Analysis and Safety Division and Dr. T. B. Belytschko of the University of Illinois, Chicago Circle, concerning the STRAW and SADCAT finite-element computer codes. And a special note of thanks goes to Dr. S. H. Fistedis, Manager of the Engineering Mechanics Section, for his continuing interest and encouragement during this phase of our study.

## REFERENCES

1. J. M. Kennedy, *Nonlinear Dynamic Response of Reactor-core Subassemblies*, ANL-8065 (Jan 1974).
2. A. H. Marchertas and T. B. Belytschko, *Nonlinear Finite-element Formulation for Transient Analysis of Three-dimensional Thin Structures*, ANL-8104 (June 1974).
3. J. M. Kennedy and T. B. Belytschko, *Energy Source and Fluid Representation in a Structural Response Code--STRAW*, ANL-8140 (May 1975).
4. A. H. Marchertas and R. T. Julke, *A Computer-code Formulation for Three-dimensional Hexcan Response Coupled with Internal Hydrodynamics*, ANL-76-17 (Mar 1976).
5. D. F. Schoeberle, J. M. Kennedy, and T. B. Belytschko, *Implicit Temporal Integration for Long-duration Accidents in a Structural Response Code--STRAW*, ANL-8136 (Oct 1974).
6. J. T. A. Roberts et al., *Fuel-Assembly Materials Simulation Program: Status Report*, ANL-8125 (Oct 1974).
7. J. E. Ash, *Analysis of Hexcan Deformations and Some Comparisons with Out-of-pile EBR-II Subassembly Duct Experiments*, ANL-8154 (Dec 1974).
8. D. J. Cagliostro et al., *Experiment on the Response of Hexagonal Subassembly Ducts to Radial Loads, Second Interim Report*, Stanford Research Institute (Aug 1975).
9. A. Mendelson, *Plasticity: Theory and Application*, The MacMillan Co., New York (1968).
10. J. H. Argyris, S. Kelsey, and H. Kamel, "Matrix Methods of Structural Analysis: A Precipit of Recent Developments," *Matrix Methods of Structural Analysis*, ed. by B. F. deVenbeke, AGARDograph 72, Pergamon Press (1964).
11. G. P. Bazeley, Y. K. Cheung, B. M. Irons, and O. C. Zienkiewicz, "Triangular Elements in Bending-Conforming and Nonconforming Solutions," *Proc. Conf. Matrix Methods in Structural Analysis*, Wright-Patterson Air Force Base, Ohio (1965).
12. M. Hartzman and J. R. Hutchinson, *Nonlinear Dynamics of Solids by the Finite Element Method*, Comput. Struct. 2, 47 (1972).
13. N. Newmark, *A Method of Computation for Structural Dynamics*, J. Eng. Mech. (ASCE) 85, 67-94 (1959).
14. D. C. Drucker, *Stress-Strain Relations in the Plastic Range: A Survey of Theory and Experiment*, Brown University (Dec 1950).
15. J. D. Lubahn and R. P. Felgar, *Plasticity and Creep of Metals*, J. Wiley and Sons, Inc., New York (1961).

Distribution for ANL-77-1Internal:

J. A. Kyger  
 A. Amorosi  
 L. Burris  
 S. A. Davis  
 B. R. T. Frost  
 D. W. Cissel  
 D. C. Rardin  
 R. G. Staker  
 R. J. Teunis  
 C. E. Till  
 R. S. Zeno  
 H. O. Monson  
 C. A. Youngdahl  
 J. E. Slattery  
 B. E. Lepacek  
 F. L. Yaggee  
 D. R. Diercks  
 R. Avery  
 J. F. Marchaterre  
 H. K. Fauske

A. J. Goldman  
 E. L. Martinec  
 I. Bornstein  
 A. Glassner  
 D. Rose  
 P. A. Lottes  
 R. H. Sevy  
 B. A. Korelc (5)  
 B. D. LaMar  
 D. H. Lennox  
 C. R. Snyder  
 L. W. Deitrich  
 L. Baker, Jr.  
 C. E. Dickerman  
 R. A. Noland  
 D. R. Ferguson  
 S. H. Fistedis (10)  
 H. Geiger (5)  
 M. T. A. Moneim

J. E. Ash (10)  
 J. C. Bratis  
 Y. W. Chang  
 H. Y. Chu  
 C. Fiala  
 J. Gvildys  
 J. M. Kennedy  
 R. F. Kulak  
 G. A. Nagumo  
 H. J. Petroski  
 C. Y. Wang  
 R. T. Julke  
 A. H. Marchertas  
 J. L. Glazik  
 R. E. Henry  
 T. J. Marciniak (10)  
 A. B. Krisciunas  
 ANL Contract File  
 ANL Libraries (5)  
 TIS Files (3)

External:

ERDA-TIC, for distribution per UC-79p (246)  
 Manager, Chicago Operations Office  
 Chief, Chicago Patent Group  
 Director, ERDA-RDD (2)  
 Director, Reactor Programs Div., ERDA-CH  
 Director, CH-INEL  
 President, Argonne Universities Association  
 Reactor Analysis and Safety Division Review Committee:  
   D. D. Glower, Ohio State Univ.  
   W. Kerr, Univ. Michigan  
   M. Levenson, Electric Power Research Institute  
   S. Levy, General Electric Co., San Jose  
   R. B. Nicholson, Exxon Nuclear Company, Inc.  
   D. Okrent, Univ. of California, Los Angeles



ARGONNE NATIONAL LAB WEST



3 4444 00010881 1